Growth and magnetotransport studies of epitaxial graphene

Graham Leslie Creeth

School of Physics and Astronomy

University of Leeds

Submitted in accordance with the requirements for the degree of

Doctor of Philosophy

September 2010

Intellectual Property Statement

The candidate confirms that the work submitted is his own and that appropriate credit has been given where reference has been made to the work of others.

The right of Graham Creeth to be identified as Author of this work has been asserted by him in accordance with the Copyright, Designs and Patents Act 1988.

Acknowledgements

I would like to thank Dr Chris Marrows for his guidance during the course of my PhD. His decision to investigate graphene in the first place has lead to a fascinating few years for me, while his support with acquiring and accessing equipment and helpful suggestions during writing have been instrumental. My fabrication of devices owes much to Dr Gavin Burnell, to whom I am very grateful for his open door and willingness to explain things again. Thanks to Prof Bryan Hickey for his contributions to and interest in the project.

STM scans were carried out at the University of York by Dr Steve Tear and Mr Andrew Vick. The vacuum systems are maintained through the skill and dedication of Mr John Turton, and the availability of the cryostat is dependent on the willingness of Mr Phil Cale to supply cryogens at short notice. The anneal of sample 2421 and the AFM scan of sample 2423 were performed by Mr Andrew Strudwick.

It has been a pleasure to spend time with colleagues and friends, both in the lab (Mike, Mannan and Nick) and the office (Kari, Ania and Aidan); time spent away from the research deck has also been great fun, whether climbing (Ania again and Marcin), playing football (Magneticos) or otherwise (everyone else!).

I could not have completed the PhD without the love and support of my parents, to whom I am extremely grateful. Listening to me talk for years about returning to do a PhD must have paled into insignificance compared to listening to me talk for years about actually doing one!

Last but not least, Lara has coped with my close and time-consuming relationship with a cryostat with remarkable good grace, and has been on-hand for moral support which is very much appreciated.

Abstract

In this thesis single-crystal 4H silicon carbide is decomposed by annealing in ultra-high vacuum conditions, forming a surface layer consisting of a few atomic layers of graphitic carbon (graphene) arranged in known crystallographic register with the substrate material. The layers of graphene on the $(000\bar{1})$ face form the subject of the thesis, and their surface morphology, crystallography and electronic transport properties are investigated in order to gain insight into the growth process with a view to improving the quality of the graphene (assessed in terms of lateral grain size, and coherence of electronic transport).

Graphene quality is improved following changes to the annealing procedure based on understanding of growth mechanisms, and the resulting material is characterised using a range of surface-sensitive techniques as well as extensive analysis of electronic transport phenomena. Comparisons made between the graphene produced by the initial and improved processes indicate an order of magnitude increase in structural coherence as a result of the changes made, with associated improvements in electronic characteristics.

Magnetotransport measurements are presented which demonstrate the two-dimensional nature of the material. These can also be used to extract values for rates associated with the various scattering mechanisms present, which in turn give insight into the electronic coherence, linking this with the physical properties. Consideration of electron-electron interaction effects is required in order to fully explain the magnetotransport behaviour seen.

Detailed consideration of surface properties seen at intermediate stages in the decomposition process (including a previously unreported surface reconstruction) is used to suggest a change to established growth procedures which if successful has the potential to further improve the quality of material.

Contents

List of Figures

Abbreviations

AC	Alternating current
AFM	Atomic force microscopy
DC	Direct current
E_F	Fermi energy
FWHM	Full width half maximum
k_B	Boltzmann's constant
k_BT	Thermal energy
LEED	Low-energy electron diffraction
MC	Magnetoconductance
mfp	Mean free path
MR	Magnetoresistance
NV	Needle valve
RMS	Root mean square (roughness)
RvT	Resistance vs temperature
SdHO	Shubnikov de-Haas Oscillations
STM	Scanning-tunnelling microscopy
WL	Weak Localisation
XPS	X-ray Photoelectron Spectroscopy
$\mathrm{v_F}$	Fermi velocity
VRH	Variable range hopping
...	...

Chapter 1

Introduction

Graphene - a single atomic layer of carbon - has formed the basis for theoretical studies of graphitic carbon in all its forms since 1947 [1]. During the intervening years, even the possibility of the existence of 2D materials was the subject of continued debate due to crystal order considerations [2]. Despite this, theoretical studies continued; the results giving excellent agreement between the behaviour of bulk carbon and 2D-based theory, and a set of predictions as to how graphene would behave, if it could be fabricated [3].

Recent developments have seen graphene produced and characterised for the first time. The two main methods of production used to date do not rely on advanced fabrication techniques, but mechanical cleavage in one case [4] and an evaporation technique with over 30 years of history [5] in the other [6]. Availability of physically realised samples of graphene has enabled agreement to be reached between experimental results and predicted behaviour [7], and also led to some unexpected characteristics such as an unconventional quantum Hall effect [8], and unusual weak localisation behaviour [9], in addition to providing further consideration for the existence of genuine 2D materials (ripples in graphene are the reason that arguments against true two-dimensionality are not violated).

The current level of interest in the theoretical and fundamental physics community is due to the continuing discoveries of properties related to the unique features of graphene's band structure [10]. In addition, a consequence of the massless behaviour of electrons in graphene is that it should allow access to relativistic phenomena such as the Klein paradox [11] which are usually thought of as associated with neutrinos (with associated length-scales) in a more convenient experimental framework [12, 13, 14]. A recent review summarises the broad spectrum of physics associated with this new material [15].

Systems in which electrons are tightly confined in one dimension, being free to move in the plane described by the other two dimensions (referred to as 2-Dimensional Electron Gas or 2DEG systems) have been studied for a number of years. These 2DEG systems exhibit several novel electronic properties, including the Quantum Hall Effect (QHE) and the fractional Quantum Hall Effect (fQHE), for which Nobel Prizes for physics have been awarded in 1985[1] and 1998[2]. Despite the fact that samples of this type can be used to probe novel quantum behaviour, research into such 2DEGs shows that the observed properties of their electron systems can be understood while treating the electrons as particles with an effective mass, as in standard condensed matter systems [16].

One reason behind the recent interest in graphene is the discovery that electrons in graphene can be modelled most accurately using relativistic equations, and can be said to behave as massless particles. The conclusion can be arrived at via band-structure calculations for a graphene sheet. For energies around the Fermi level (within ∼1 eV) the relationship between E (vertical axis) and $\underline{k}$ (horizontal plane) is linear, due to two intersecting cosine-like energy-bands (one from each sublattice). This band structure has now been measured using angle-resolved photoemission spectroscopy (ARPES) and shows good agreement with theory [17].

Graphene is not only of interest to those studying fundamental physics, but also those involved in materials science / device manufacture. Properties such as high mobility at room temperature, long mean free path (of the order of 1 μm) and long spin-relaxation times make graphene a candidate for inclusion in (if not

---

[1] K. von Klitzing

[2] R. B. Laughlin, H. L. Stormer, D. C. Tsui

a framework for) future electronic devices [18, 19], and seem certain to maintain the current focus on the material.

Two main techniques exist for the production of graphene - micromechanical cleavage (known as the Scotch tape method) [4] and heat treatment of silicon carbide to produce a surface layer of carbon [6]. Mechanical cleavage has been shown to be a reliable technique for producing highly perfect monolayers, but yields samples of limited size. The main advantage of epitaxial growth via heat treatment is that sheets of graphene can be produced which are large enough to pattern into full device structures via lithographic techniques (either conventional [6] or novel [20]). While other technologies are being developed which can produce large monolayers using chemical vapour deposition (CVD) [21], these require subsequent transfer onto other substrates, and as with the cleavage method this has the potential to introduce defects. Using single-crystal 4H SiC (a polytype with hexagonal symmetry), growth initiates from within the crystal, and an initially clean surface is all that is required to produce graphene which is fully electronically decoupled from the substrate.

Despite the long history of SiC as a material for high-power components [22, 23], the initial focus (on the detrimental influence of carbon to the properties of these components) informed the choice of techniques used (low energy electron diffraction (LEED), Auger spectroscopy) and the temperatures studied. As the aim was not to optimise the quality (structural or electronic) of the surface graphitic material these choices were not necessarily best suited to these ends, and hence the current interest in epitaxial graphene is, while reliant on some existing knowledge, almost a nascent field in its own right. SiC technology is advanced, and there are several research groups using their knowledge of SiC to produce graphene. The state-of-the-art includes many, sometimes conflicting, paradigms, involving expertise in semiconductor sample preparation and interpretations of growth conditions and mechanisms.

1.1 The effect of growth conditions on epitaxial graphene

The properties of graphitic material grown by thermal decomposition of silicon carbide are a consequence of both the substrate surface prior to graphitisation, and the details of the annealing conditions used. Substrate surfaces can be improved by advanced polishing or etching in hydrogen to remove surface scratches resulting from standard polishing techniques. Wafers with very small offcut angle from a vicinal surface can be chosen in order to minimise atomic steps, or small amounts of additional SiC can be grown in order to form an atomically flat surface.

SiC is polar, with the $\{0001\}$ faces Si- and C-terminated respectively. The material which results from graphitisation differs for the two faces, but in each case the carbon-rich surface which ultimately forms graphene results from preferential evaporation of silicon when the substrate is heated above $\sim 1250°$C.

With no external source of carbon required, the available variables through which to influence the growth dynamics are temperature, pressure and duration of anneal. The effects of these parameters complicates process, as they do not act in isolation on the various processes which are taking place. Lower temperatures may be expected to provide more control over the growth rate, but can result in ungraphitised areas continuing to act as sources of carbon, leading to more layers than if the process had resulted in a covering layer which can then slow subsequent evaporation.

The main motivation for graphene studies is electronic transport properties, however iterating through cleanroom fabrication, etc is a time-consuming, *ex-situ* process which has the potential to damage samples. In addition, there is considerably more literature published on the surface characteristics than the transport properties, especially on non-ideal material. Obtaining equivalent surface science data, and adding transport properties ensures that transport properties are understood in context, and addresses an important disconnect which exists in the subject area.

1.2 The aim and contents of this thesis

The PhD was undertaken with a view to producing large areas of defect-free graphene on SiC. Analysis of data collected on non-ideal material lead to improvements to the procedures used, and hence to higher quality material.

The thesis shows a development of the process used for producing layers of graphene, with lateral sizes increasing by an order of magnitude as a result of considerations of growth dynamics. The resultant lateral size is still smaller than the current state of the art, however the improvements lead to a conclusion that further refinement is possible. The detailed analysis of magnetotransport and complementary surface measurements for imperfect and incomplete layers is a combination which is under-reported in this research area, despite the potential for insight into growth dynamics which can inform the state of the art. In fact it is true to say that there is a general preponderance of surface studies over transport studies of epitaxial graphene. It is likely that features seen clearly in the transport properties of imperfect films are also present to a lesser degree in higher-quality material, and this widens the relevance of these results.

The growth procedures used for epitaxial graphene have undergone a rapid evolution in recent years. Despite the clear and measurable progress, this has arguably outpaced comprehensive understanding of the exact reasons for the improved quality of the material; it is unlikely that growth has been fully optimised, as any new insights could inform alterations to the procedures used.

The outline of this thesis is as follows. Chapter 2 introduces the physics used, both with resect to the motivation for studying ideal graphene, and also the physics underpinning the experiments and interpretations of data relating to epitaxial graphene at various stages of formation. Chapter 3 describes the methods for fabrication and characterisation, and the details of some data analysis procedures. Chapter 4 contains results from various surface science techniques used to characterise the material.

The electronic properties of the material are presented in the remaining chapters. Chapter 5 concerns the posited growth mechanism, how this is seen in terms of electronic properties and how different transport measurements can provide information as to several distinct behaviours of electrons in the system. Chapter 6 presents results from material grown following changes to the fabrication procedure informed by the results from chapters 4 and 5, showing improved characteristics of the graphene layers, and some new properties. The presence of some features seen in the less ordered material persist, and are discussed in more detail. Chapter 7 presents details on electron-electron interactions in the material produced, both when this is an overt contribution, and also when the contribution is present but less obvious.

Chapter 8 will conclude the thesis with an overview of the contents and conclusions, plus the outlook for research in this field, and plans for future experimental work.

Chapter 2

Theory and background

2.1 Introduction

As outlined in the introductory chapter, this thesis contains details of transport properties of epitaxial graphene on SiC at various stages during the formation of films, and for films which exhibit characteristics, indicative of varying structural and electronic order. The contents of this chapter reflect this, as the physics behind both the unique properties of ideal graphene and the behaviour seen in incomplete or non-ideal films is covered.

2.2 Graphene electronic structure and transport

2.2.1 Two-dimensional materials

The (at the time hypothetical) question of whether a 2D crystal can exist, due to thermodynamic arguments was first addressed in 1934 by Peierls [24], and subsequently by Mermin [2]; with the the advent of graphene in 2004 the opposing ideas could be tested, although to date even in graphene systems the the arguments for a ‘true’ two-dimensionality can be said to be unresolved, as in practice substrate support, or slight buckling at real temperatures can be viewed as three-dimensional qualities.

Prior to the advent of crystallographically two-dimensional (monolayer) materials, structures which resulted in confined electrons existing in a well-defined plane (often at a buried interface in a stack of epitaxially engineered material such as GaAs/AlGaAs) known as two-dimensional electron gas or 2DEG systems were studied. These introduced a plethora of physics in terms of measurement techniques and interpretations [25], many of which are used to evaluate graphene and compare it to existing results for 2DEGs.

2.2.2 Graphene band structure

The band structure of a single layer of graphene, consisting of a hexagonal 'chicken-wire' arrangement of carbon atoms, was first calculated in 1947 by Wallace [1] and has subsequently been used as the foundation for theoretical studies of other forms of graphitic carbon. In this lattice, one conduction electron is contributed per atom, with three bonding covalently with adjacent atoms to form the honeycomb structure, with two atoms per unit cell. The basis of the band structure is that there are two sublattices due to adjacent atoms being crystallographically inequivalent. This leads to the formation of two bands, each with a cosine-like dependence of electron energy on the wave vector k.

When the structure is plotted (figure 2.1 shows the band structure of an isolated graphene sheet, calculated using tight-binding approximations as in [26]) the 'eggbox' structure is seen, with the two bands crossing at the edges of the first Brillouin zone, meaning that graphene is a zero-gap semiconductor.

The more subtle aspects of this bandstructure are twofold. In the vicinity of the Fermi level the band structure is conical (seen in diagrammatic for in figure 2.2), meaning that the energy dispersion is linear (Energy E varies linearly with momentum k described by

$$E = \hbar \cdot V_{\mathrm{F}} \cdot k \tag{2.1}$$

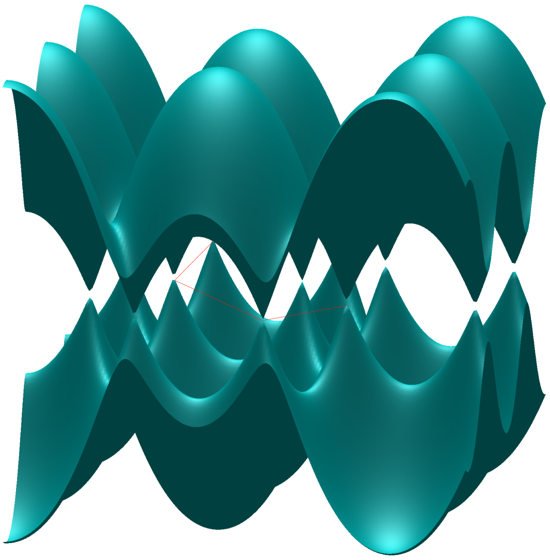

Figure 2.1: Graphene band structure, calculated from a tight-binding approximation, as in [1] .

where $\hbar = h/2\pi$, h is Planck's constant and V_{F} is the Fermi velocity. This is in contrast to the near-ubiquitous quadratic dispersion for condensed matter systems which arises from the Schrödinger equation. As the effective mass is given by the second derivative of the dispersion relation, electrons in graphene can be said to be massless, and equivalent to other massless fermions, such as neutrinos, which are more properly described by the Dirac-Weyl equation [7]. A second formal equivalence between descriptions of electrons in graphene and the Dirac equation is that it is possible to include the two sublattices using a 2-element column vector known as a spinor (as used conventionally to denote particles and antiparticles). Electrons are then said to have a pseudospin denoting the sublattice on which they exist, based on which element of the spinor applies to them.

A consequence of the use of spinor notation to denote the valley degeneracy of the system is that a particle travelling around a closed trajectory experiences a phase change of π, referred to as a Berry's phase. It is this which provides a link between the theoretical construct describing electrons in a lattice of carbon atoms as 'relativistic' and experimental observation, as this Berry's phase gives rise to

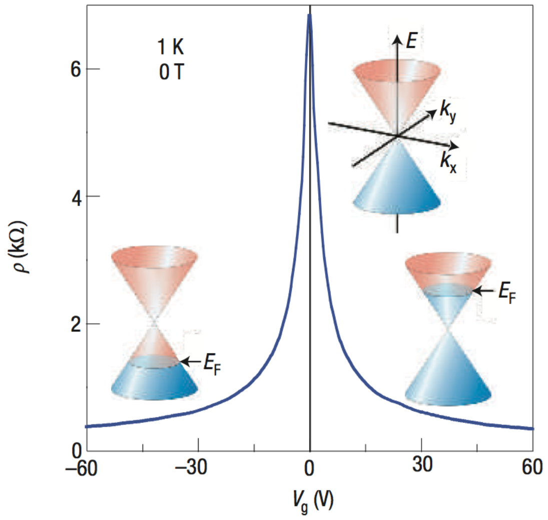

Figure 2.2: Diagram of conical band structure near the Dirac point, and the associated gate-dependent resistivity, from [12].

a distinct (and unique) departure from the conventional integer quantum Hall effect [27] (see section 2.2.3). This is the most striking consequence of graphene's unique structure, but not the only one. The phase gained during an electron following a closed path leads to an important modification to weak localisation theory (see section 2.3.2).

A correction to the simplified picture of conical band-structure features is known as trigonal warping, and can be understood if the band structure diagram is pictured being sliced. Close to the E_F (*i.e.* the Dirac point), the band structure is conical, and the cross sections through any energy (horizontal) section will be circular, however as adjacent cones overlap at higher energies, the surface gains a three-fold symmetry.

As subsequent layers of graphene are added to the system, the stacking order determines the properties, as a regular AB stacking lifts the sublattice degeneracy through interlayer coupling. A motivation for studying epitaxial graphene on 4H SiC $(000\bar{1})$ is that the less ordered stacking means that the properties of an isolated monolayer of graphene persist for systems with multiple layers, due to the degeneracy between sublattices being preserved.

Undoped, isolated graphene would have a vanishingly small number of charge carriers at zero temperature. While this condition can be achieved experimentally, epitaxial graphene, as a result of interactions with the substrate, usually has an effective doping resulting in a carrier density of $\sim 1 \times 10^{12}$ cm^{-2}, corresponding to a Fermi wavelength of $\sim 10^{8}$ m^{-1} [28].

2.2.3 Magnetoconductance of high-quality graphene

The application of a magnetic field (most commonly perpendicular to the plane of the sample) is widely used to characterise electron propertied in sheet material or 2DEG systems. The application of such a field to graphene yields some behaviour which is shared with other systems, and some which is unique. Graphene which is virtually defect-free will still have some impurities (in the case of mechanically cleaved samples these could be from the substrate prior to deposition of a flake, and in all cases can be due to surface adsorbants); these can contribute to processed discussed in section 2.3. Samples sufficiently free from defects exhibit a unique quantum Hall effect, which is the most definite electronic fingerprint of graphene. In the conventional integer quantum Hall effect, plateaux in Hall conductance σ_{xy} occur when the quantisation of electron energy levels into Landau levels means that there are no available states close to the Fermi level. These plateaux occur in a regular sequence if the Fermi level is changed by means of a gate voltage, with values of Hall conductivity given by $\sigma_{xy} = (4e^2/h)N$, where N is an integer, whereas in monolayer graphene the sequence is $\sigma_{xy} = (4e^2/h)(N+1/2)$ [7]. This is shown in figure 2.3 from reference [7] in which the magnetic field is held at a constant value, and the carrier concentration is modified using a gate voltage while the Hall (σ_{xy}) and longitudinal (σ_{xx}) conductivities are measured. For bilayer graphene the conventional QHE is recovered (inset of figure 2.3).

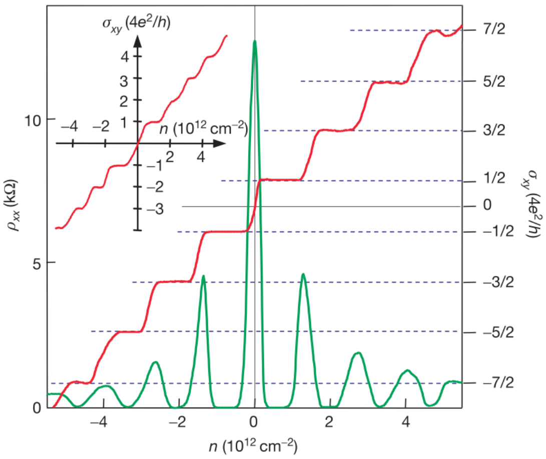

Figure 2.3: Quantum Hall effect for monolayer graphene, and (inset) bilayer graphene. From [7].

2.3 Conduction in disordered systems

The effective doping seen in epitaxial graphene systems means that it is a conductor at finite temperatures, and the conduction through disordered graphene systems is described by well-established theory. Conduction in any condensed matter system happens as a result of the presence of available states into which electrons can scatter following the application of an external electric field. Deviations from metallic conductivity can arise due to band structures which affect this availability, or from consequences of physical disorder. In a disordered system, local defects mean that carriers experience an extremely non-homogeneous potential landscape. Two consequences of this are seen in samples presented in this thesis and these are described in the following sections.

2.3.1 Variable range hopping

The variable range hopping regime describes conduction for electrons localised due to charge impurities. Thermally-activated transport can still occur in this situation, and is known as hopping conduction. The argument for variable range hopping (*i.e.* hopping to a non-adjacent site) is given in reference [29]. The average spacing (in energy) between states, ΔW near the Fermi energy $N(E_F)$ is given (in 3 dimensions) by

$$\Delta W = (3/4\pi)R^3 N(E_{\mathrm{F}}) \tag{2.2}$$

where $N(E_F)$ is the density of states, and so the probability of a hop to the lowest available energy ΔE is range-dependent, being equal to the reciprocal of the above expression. The probability of hopping a distance R has a separate range dependence of $\exp(-2\alpha R)$ where α quantifies the wavefunction decay, and these expressions combine with the distribution of available energies at a temperature T to give a hopping probability (and hence a conductivity) which can be written in terms of a constant A and characteristic temperature B, as (for the 3-dimensional case)

$$P_{hop} = A \exp(-B/T^{-\frac{1}{4}}) \tag{2.3a}$$

$$B = 2\left(\frac{3}{2\pi}\right)^{\frac{1}{4}} \left\{\frac{\alpha^3}{k_{\mathrm{B}} N(E_{\mathrm{F}})}\right\}^{\frac{1}{4}}. \tag{2.3b}$$

This three-dimensional argument is generalised for lower-dimension systems by replacing the exponent with $1/(n+1)$ where n is the dimensionality of the system. Efros and Shklovskii also modified the expression for the presence of the coulomb interaction, finding the exponent to be 1/2 for both two and three-dimensional systems.

2.3.2 Localisation

For less disordered samples, the timescale associated with collisions which cause phase-breaking (a change of energy state) increase. This is the basis for an argument based on two oppositely-directed closed trajectories formed by a carrier experiencing multiple scattering events [30]. If the carrier retains phase through such a trajectory, the resultant probability found from squaring the resulting wavefunctions will be maximal at the origin (also the return point) of the trajectory: the electron is preferentially backscattered. This 'weak localisation' (WL)is destroyed by the application of a magnetic field, which introduces a phase difference for the oppositely-oriented paths, decreasing the preferential backscattering and hence the resistance. The effect is more pronounced at lower temperatures, as the phase-coherence length becomes longer; a review of the full area of physics is given in reference [31]. The sharpness of the (MR) peak due to WL can be used generally as a gauge of sample quality, with more ordered samples having sharper peaks.

The same argument must, when used for graphene, consider the effect of the Berry's phase arising from the sublattices. As a closed trajectory now (in the absence of a magnetic field) causes a phase-change of π the same argument for scattered electrons leads to the opposite conclusion as the two wavefunctions will be out of phase, leading to a minimum probability at the origin; this suppressed backscattering is referred to as weak antilocalisation (WAL). In the presence of a magnetic field, the influence is two-fold in terms of observed behaviour; there is a positive component at high-field, and suppression of WL at lower fields [32]. The coherence of 'pseudospin' has an associated scattering rate, and the relative magnitude of this and the other scattering rates in the system determines which mechanism is dominant (this balance changes with temperature as the various scattering rates have different dependences on temperature).

There are therefore several potential components present in measured magnetoresistance data:

- Positive component from classical Lorentz force present at all temperatures
- Negative magnetoresistance due to enhanced backscattering
- Suppression of WL by WAL at all fields, magnitude of suppression similarly dependent on sample-specific properties. Samples with a larger relative contribution from WAL will have a positive MR component from WAL above a certain field.

2.4 Large area graphene production

In order to grow a thin film of carbon it is self-evident that you require a source of carbon atoms, and a means to promote bonding between them to produce sheet material. This leaves scope for a huge range of approaches, some of which are briefly summarised here.

Graphene platelets can be formed by chemical means, generally oxidation of highly ordered pyrolytic graphite in order to form oxygen-intercalated structures (graphene oxide, or GO) which can be reduced to form suspensions of graphene.This process is capable of extremely high yields in terms of surface area, but results in domains which are small (μm length scales) and disordered with respect to each other. Dispersion of the solution while maintaining true two-dimensionality is difficult, and an annealing procedure or similar would be required to form larger areas. The electronic properties of some samples prepared by this method are presented in [33].

It is possible to grown graphene on ruthenium [34] via an annealing technique. The source of carbon is impurities in the ruthenium itself, and on emerging from the substrate it is observed to form large regular graphitic regions. The fact that the substrate is a metal means that probing the electronic properties of this layer is problematic, as would be using the overlayer in a regular integrated circuit. If the grown material could be transferred the technique would avoid both of these issues, but transfer is non-trivial.

Despite issues with transference of graphene material, a recent paper reports a process involving chemical vapour deposition (CVD) combined with roll to roll transfer techniques [21]. The length scales involved (30 inch wide sheets) mean that if this is a viable method it is by far the leader in terms of ‘acreage’.

Finally (although not strictly large area) graphene can be produced by ‘unzipping’ carbon nanotubes [35]. Given the relatively long history of nanotube placement, orientation and alignment, and associated difficulties it would be ironic if the solution to the utilisation of a supposedly more convenient allotropic form relied on placement of nanotubes followed by this unzipping process.

2.5 Thermal decomposition of SiC

2.5.1 Structure of SiC

Silicon carbide exists in a huge number of polytypes. The studies presented here are based on the 4H polytype, where H denotes hexagonal symmetry and the 4 refers to the number of bilayers in a repeat sequence (ABCB). The {0001} polar faces in this case are terminated by silicon and carbon atoms, respectively.

2.5.2 Thermal decomposition process

Thermal decomposition of SiC leading to the formation of a graphitic overlayer has been known of and studied for decades [36], although the interest was initially in understanding the carbon growth with a view to eradication or mitigation of deleterious effects on the properties of SiC components. On heating to temperatures above 1000 °C, the structure of SiC becomes unstable, with bonds breaking and free atoms able to leave the surface. Silicon evaporates preferentially to carbon, leaving a SiC surface which is depleted of silicon.

Growth of graphene proceeds as a result of three adjacent layers of SiC being left (as a result of Si desorption) with a lattice vacated by Si. Depending on the nature of the nucleation site, this can mean that the graphitised layer grows such that it is raised above the substrate surface which has yet to be graphitised, or such that it is lower than ungraphitised areas. If the nucleation site is a screw dislocation, the graphitised area spreads outwards from the dislocation site, forming a depression whose walls rise to the substrate level [37]. If, however, the silicon egress is from a step edge, then the process can proceed along the upper level of the step, leaving the lower-level of substrate bare (or being graphitised from another step) [38]. In terms of characterisation, this introduces an important distinction between the topographic height and the thickness or depth of graphene; it is not trivial to correctly assign number of layers using scanning probe techniques. In fact, irrespective of the growth regime, three layers of SiC decomposing to form a single layer of carbon argues for a depression in the substrate as a result of graphene formation.

Formation of an overlayer via decomposition of a silicon carbide substrate has many potential advantages over other methods. Apart from considerations such as compatibility with existing wafer-scale fabrication techniques, the growth process itself has (once optimised) fewer variables to control, as incident flux, flow rates or exact chemical concentrations are not essential, and the process should be controllable through correct temperature, duration and pressure conditions for an anneal. The complexity of this approach lies in the fact that several mechanisms with a significant amount of interplay are at work, and optimising a parameter for one may negatively impact another. The two primary features are the net rate of silicon egress, and the lateral propagation of the resulting domains of graphene. The desorption rate can be controlled via an incident flux of silicon from an external source [39], but this is not necessary (although it can help to remove native oxides); similarly it is possible but not required to provide a carbon flux [40]. Without these external control mechanisms, the source of carbon is the substrate itself, through the mechanisms described above. As the desorption from different structures on the substrate is associated with different energy scales, and as the surface mobility of, and bond formation between carbon atoms are temperature dependent, the ideal annealing conditions, while potentially being described only by three parameters, are not trivial to identify.

Research initially focussed on the (0001) face, as the surface structure appeared more ordered. This continued with the advent of graphene as a desirable material on SiC, as opposed to an unwanted byproduct of high temperature operation of SiC components. More recent work has moved rapidly from UHV annealing [41] to the use of confined geometries [42] and atmospheric pressures [43] to control growth, and the state-of-the-art with these methods has reached a point where wafer-scale single-domain growth is possible. This high-quality epitaxial graphene exhibits the same distinctive half-integer quantum Hall effect as that produced by the cleavage method, as seen in figure 2.4 (from [28]). In this measurement the carrier concentration is held at a constant value and the magnetic field is swept in order to move Landau levels through the Fermi surface, while measuring the conductivity in both geometries (σ_{xy} and σ_{xx}).

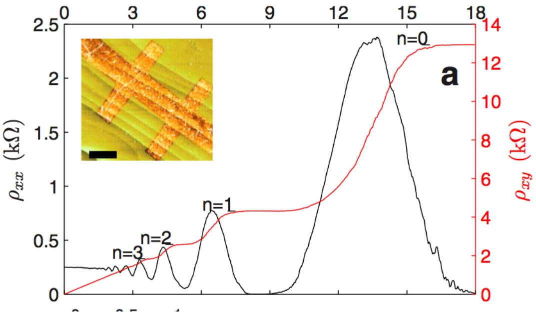

Figure 2.4: Quantum Hall effect for measurement on monolayer epitaxial graphene, from [28]. The device is shown in the inset

The change of emphasis from crystallographic curiosity to growth of electronic component has meant that intervening surface reconstructions are no longer widely investigated as an end in themselves, and while known stages in graphitisation were initially used in the development of growth procedures, the use of enclosures and atmospheric pressures make *in-situ* surface measurements less of a *de facto* activity. Combined with the relatively scarce literature on the $(000\overline{1})$ face (due historically to an apparently less ordered crystallography) this leads to a situation where despite the recent interest and progress with regards to this crystal termination, the details of the growth dynamics, although demonstrably exploited, are not fully understood.

2.5.3 Properties

Graphene formed by thermal decomposition of SiC has properties which differ from those of cleaved graphite. The properties also depend on the polytype of SiC used as a substrate; details here are for the semi-insulating 4H polytype used in this study. Transport properties are presented for the $(000\overline{1})$ face, as described above. The stacking which results is in contrast to the AB (Bernal) layer ordering which exists for naturally occurring graphite; even if several or many carbon layers are produced, their properties do not approach equivalence with a similar number of layers cleaved from a graphite crystal [42]. LEED and X-ray measurements show that layers are rotated with respect to each other and that the resulting structure consists of graphene layers which are electronically decoupled from their immediate neighbours [44].

By contrast, the (0001) layer shows LEED commensurate with exact epitaxial order, although counterintuitively this results in poorer electronic properties. Graphene on this face grows an initial structure referred to as $6\sqrt{3}\times 6\sqrt{3}R30$, also known a buffer layer or 'zeroth' layer. The stoichiometric composition of this layer is 100 % carbon, and the bond lengths show agreement with a graphene 'chickenwire' structure, but crucially the π-electrons form covalent bonds with the SiC layer beneath. This orders the layer with respect to the substrate, and at the same time removes the electrons responsible for conduction. This hypothesis can be proven very convincingly by intercalating hydrogen between the substrate and the zeroth layer. For samples with only the zeroth layer grown this results in monolayer properties (in LEED and angle-resolved photoemission spectroscopy (ARPES)); for a sample which initially has the zeroth layer plus one monolayer, bilayer properties are seen [45].

Chapter 3

Methods

3.1 Introduction

This chapter introduces the techniques used to fabricate and characterise epitaxial graphene on SiC. Analysis procedures are also described in detail, for both Raman spectra and for transport data (specifically measurement of resistance in an applied magnetic field) since these methods are used extensively in the following chapters as standard characterisation tools.

3.2 Fabrication Methods

The number of layers and lateral size of epitaxial graphene domains are critically dependent on the annealing conditions. Initial attempts to produce graphene on SiC used conditions known to produce a graphitic layer in UHV. Subsequent work has used lower vacuum and also atmospheric pressures of inert gas, resulting in larger graphene domains, up to the wafer scale. All results presented in this thesis use UHV conditions, with temperature and duration of anneal being varied in order to increase lateral dimensions of graphene.

3.2.1 Sample preparation and mounting

All results presented in this thesis are based on graphene grown on a substrate of 4H polytype silicon carbide (SiC), with an offcut of 0.13°. This choice of polytype is based on the potential for monolayer graphene-like transport properties (on the $(000\bar{1})$ face) which persist even in multiple layers [44]. In order to ensure that measured electronic behaviour can be separated from any substrate contribution, the substrates are semi-insulating, with a quoted resistivity of $> 10^5$ Ω-cm.

Substrates were purchased from Cree, inc. [46] with the polar faces both polished. The wafer was diced into sections measuring 5mm x 10mm, during which process it was protected with polymer resist. Prior to annealing, a piece of substrate is cleaned by sonicating in acetone followed by isopropanol to remove this resist, and is then mounted into a recess in a circular plate made of molybdenum. Tungsten wire is used to secure the substrate in place, in order that the sample remains in the recess for annealing, and that the entire plate can be inverted while still under UHV conditions.

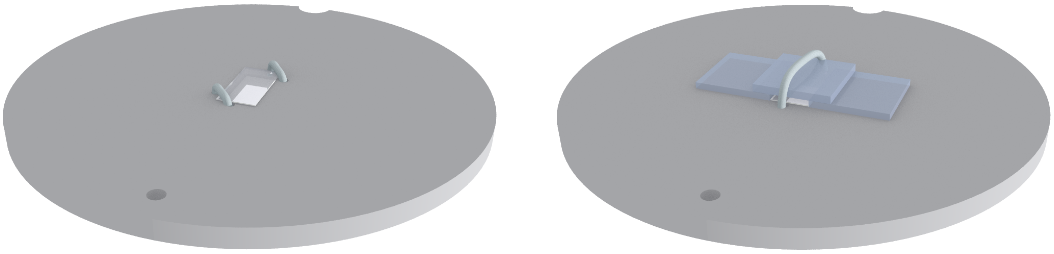
(a) (b)

Figure 3.1: Sample mounted for annealing. Uncapped samples (a) can be secured with tungsten wire and can therefore be inverted for LEED on both faces *in situ*, whereas samples with an Al_2O_3 cap (b) cannot.

In the case of the samples annealed at higher temperatures, the substrate is protected from possible debris from the heater assembly. This is achieved using three pieces of sapphire, each 1mm thick and measuring 10 mm x 10 mm. Two pieces are placed on the molybdenum plate, either side of the recess in which the substrate sits. The third piece is then rested on the first two, producing an enclosure open on two sides, with a 1 mm separation between the up-facing face of SiC and the capping piece of sapphire. A piece of tungsten wire is then used to secure the structure. Samples annealed in this way cannot be directly secured to the plate with tungsten wire, so LEED is only possible with the plate in the same orientation as during the anneal. The reverse face can be investigated via LEED by removing the sample, inverting and reloading, followed by a flash anneal as described in the LEED section.

3.2.2 Vacuum conditions

The vacuum chambers which house the annealing and LEED systems used here form part of a molecular beam epitaxy (MBE) system manufactured by VG Semicon. In normal usage, the system is used to grow atomically thin layers of metals under clean ultra-high vacuum (UHV) conditions. For the purposes of this study, the pertinent components are the manipulator which houses the heating assembly (discussed in the following section), the vacuum chambers themselves, and the pumping systems which create and maintain the vacuum conditions.

Samples are loaded through a fast entry lock (FEL). This is a small chamber housing a carousel able to hold ten sample holder plates at a time. To load, the FEL is vented using dry N_2, the carousel removed and loaded with plates holding samples to be processed. The FEL is then pumped using a roughing pump (diaphragm pump) followed by a turbo-molecular pump. In order to maintain the best possible vacuum conditions, the FEL is pumped by the turbo pump overnight.

The FEL opens into the preparation chamber. The vacuum in this section is typically 10^{-8} mbar or better, and is maintained by an ion pump. This chamber houses the LEED system, and allows access to the main chamber and the scanning tunnelling microscope (STM).

The main chamber has a typical base pressure of 10^{-10} mbar. This is maintained by a diffusion pump. A titanium sublimation pump (TSP) is also installed in the main chamber and fires at intervals of 5 hours, in order to remove small gas molecules such as H_2 for which the diffusion pump is less effective. The heater assembly is used to anneal samples, and during this process the vacuum deteriorates due to the desorption of gas from the substrate, the molybdenum sample holder and the heater assembly itself. For longer-duration and higher temperature anneals, more distant areas of the vacuum chamber may also desorb gas. To mitigate these effects, the chamber walls are cooled when annealing is in progress, using a shroud filled with liquid N_2. The resulting vacuum whilst annealing is better than 10^{-8} mbar, and can be as low as 10^{-10} mbar (the base vacuum improves day on day during periods when the chamber is not opened to atmosphere for servicing, as gas desorbed from the system during anneals is pumped away either at the time or (if it has settled on the walls of the chamber) later, when the LN_2 shroud has warmed to room temperature.

3.2.3 Annealing process

Samples are annealed in the UHV conditions of the main chamber (see previous section). The MBE system has a manipulator fitted with a PgG (Graphite, coated with Pyrolytic Graphite) element. The element is resistively heated and the maximum temperature is limited by the power supply; the peak temperature registered on the thermocouple is 1535 °C, with the power unit supplying 46 V and 56 A. The thermocouple enables temperature to be monitored, and is connected to a Eurotherm temperature controller in order that constant temperatures can be maintained. The temperature of the surface of the sample itself can be monitored using a pyrometer, although for transparent samples this technique has some limitations. To address this, a set of anneals were completed with Ta/C sputtered onto the (0001) face of the substrate, so that the sample was opaque. The sample was then mounted with the sputtered material closest to the heater assembly, and thermocouple and pyrometer readings were compared. Sample surface temperatures measured with the pyrometer were lower than thermocouple temperatures by approximately 10 °C at 1200 °C, and the difference increased slightly at higher temperatures. As the thermal properties of the sample are altered by this technique, and as the readings are in close agreement, temperatures quoted here are thermocouple readings. Any attempt to achieve the same growth conditions in a different apparatus would require the equivalent system temperatures to be ascertained.

The SiC substrate is positioned beneath the manipulator element and is radiatively heated. The temperature is initially increased gradually in order to maintain a good vacuum. Water vapour and adsorbed gas are driven off (with an accompanying temporary rise in pressure) at between 100 °C and 300 °C. These temperatures are too low to have an effect on the SiC substrate and is therefore not critical to the final graphene layer produced; the time for which the sample is held at these temperatures is determined by the vacuum conditions in the chamber (plates which have been under atmospheric conditions in the lab for extended periods require longer to fully outgas). The outgassing constitutes one of several stages of anneal, which are valid for any of the specific procedures discussed in more detail below. These general stages are

- Desorption. Sample temperature 100 °C, 300 °C, 600 °C until chamber vacuum recovers, indicating that substrate / sample holder has outgassed
- Reconstruction. Sample temperature 900-1100 °C. This allows some further desorption of gas, and also surface reconstruction. After this stage a 1×1 reconstruction can be seen using LEED (see section 4.2)
- Graphitisation. Sample temperature above 1275 °C. During this stage graphitisation occurs as described in section 2.5

The manipulator heating assembly is lowered into place above the sample, with the heater element in close proximity during the anneal. The heating assembly is shown during an anneal in figure 3.2.

The details of the final stage of the anneal depend on the objective of the experiment. In order to assess the onset of graphitisation, samples were annealed at 1300 °C for varying lengths of time. Following analysis of this data, other anneals were carried out at higher temperatures, for varying durations (in general higher temperatures require less time to produce a film of graphene which extends

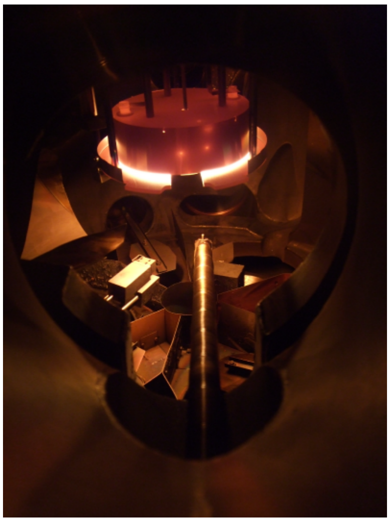

Figure 3.2: Manipulator at 1235 °C. The sample itself cannot be seen, as it is positioned beneath the heater assembly. The sources for metal MBE growth can be seen on the base of the chamber, and the wobble stick for sample transfer is in the foreground.

over the entire substrate surface). Following the final stage of the anneal the sample is not actively cooled as the temperature in any case falls rapidly below the temperatures at which graphitisation occurs, reaching 1200 °C in less than 60 seconds.

3.3 Surface characterisation

Several surface-sensitive techniques were used to refine the fabrication procedures described in the previous section.

3.3.1 Low-energy electron diffraction

Adjacent to the chamber in which the samples are annealed is a rear-view low-energy electron diffraction (LEED) system manufactured by VG Semicon. The system is mounted onto a flange on the top of the chamber with the component parts in the orientation shown in figure 3.3. Electrons can be accelerated from the filament using voltages of up to 1kV, although in practice most of the detailed diffraction patterns can be discerned more clearly with far less energetic electrons. Electrons incident onto the sample surface do not have sufficient energy to penetrate further than a few atomic layers into the material. They are scattered from the atomic potentials, and if the material consists of a regular array of potentials (typically as a result of being a single crystal) then the interference between reflected electrons gives rise to a diffraction pattern. The reflected electrons are focussed, and higher energy electrons from specular reflection are retarded by applying potentials to the various components of mesh and grid. Finally electrons are accelerated towards the phosphor screen in order that the diffraction pattern can be viewed. A CCD camera and image-capturing software enable the patterns to be stored for the purposes of comparison, and the sample can be moved laterally to obtain diffraction from areas over the entire surface. The spot size is approximately 500 μm, hence the diffraction image seen is an average over that area. To acquire data from the LEED system from samples which have spent time *ex-situ* it is necessary to remove adsorbed gas from the surface by annealing at 600 °C for one hour.

Low-energy electron diffraction (LEED) relies on electron scattering from the material, and this makes it a surface-sensitive technique, as the penetration depth in any given material is short (less than 10 nm) [47]. For the epitaxial samples studied here, this means that visible diffraction features from the substrate can be used to give an upper bound to the number of graphitic overlayers grown. More detailed conclusions can be drawn from graphitic diffraction features, and from interference patterns between the two contributions.

An example of the LEED signature of graphene grown epitaxially on SiC is shown in figure 3.4. This diffraction is from graphene grown on the Si-terminated (0001) face of the SiC substrate, and is chosen as an introduction to the various features (the focus of this section, as with the rest of the thesis, is the $(000\bar{1})$ face). Features can be seen from both the substrate and the overlayer. The crystal structure of the graphene is hexagonal, as is the termination of the SiC, leading to two distinct hexagonal diffraction patterns from their respective reciprocal lattices,

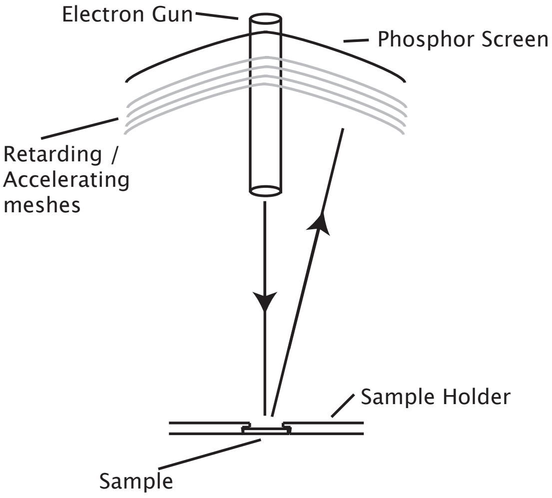

Figure 3.3: LEED System schematic.

as well as an interference between the two patterns. The appearance of both sets of diffraction spots, as mentioned above, puts an upper limit on the number of graphene layers present. The fact that the features due to substrate diffraction, graphene diffraction and interference are all spots indicates that there is good crystal order between the substrate and the graphene, meaning that in terms of crystal orientation the graphene is truly epitaxial. This specific arrangement of diffraction spots is referred to in the literature [5] as $6\sqrt{3} \times 6\sqrt{3}$R30, a denomination which refers to a surface reconstruction of the SiC substrate ($\sqrt{3}$R30) and the 6×6 pattern around the substrate diffraction spots. This pattern is visible once there is a single graphene layer on the surface, however the electronic properties of this first layer show that the π electrons which would normally be the charge carriers are covalently bonded to the substrate. This first layer is therefore referred to in the literature as the 'zeroth' layer, as it plays no part in conduction. Visual comparison of the diffraction pattern in figure 3.4 with published images in references [48, 49] enables the thickness estimate to be refined to between 1 and 4 layers of graphene (at least on this face of the substrate) for this sample, based on the extent to which the diffraction pattern from the substrate is visible.

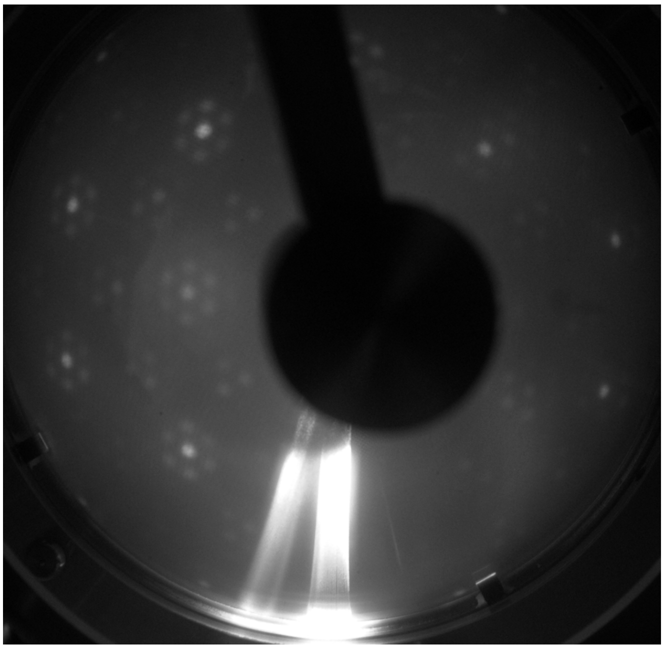

Figure 3.4: LEED pattern from (0001) face taken at 184 eV. The origin of the pattern is to the left of the circle of the electron gun.

3.3.2 Raman spectroscopy

Raman spectroscopy is one of the most widely used techniques associated with graphene produced by the micromechanical cleavage method (and has a long history in the study of graphitic material in more general terms [50]. The most commonly used substrate for this method is silicon with an oxide thickness of either 300 or 100 nm, as these aid the visual identification of monolayers [51]; an additional benefit of this is that silicon has no Raman spectral features in the region of interest for graphene. The Raman signal from cleaved graphene can be used to distinguish a monolayer from a bilayer very clearly; these are shown in figure 3.5, which introduces the spectral features. Each spectrum has a feature at 1580cm^{-1}, known as the G peak; the other spectral lines which are of interest are known as the D peak (at 1350 cm^{-1}), and the G$'$ or 2D peak (at 2700 cm^{-1}) [52]. The terminology G$'$ was used in early Raman studies on graphitic systems purely because it was the second largest peak in graphite, and does not denote any mechanism in common with the G peak; it is in fact the second order of the peak at 1350 cm^{-1}, and will be referred to as 2D from here on. For flake graphene or perfect layers of epitaxial graphene, the ratio of integrated intensity between the G and 2D peaks is the indicator of layer thickness for very few layers; due to an enhanced 2D peak for a single layer, the ratio I_{2D}/I_{G} is greater than 1 for a monolayer, approximately 1 for a bilayer and decreases below unity for subsequent layers. The D peak is associated with a breathing mode of sp^2 carbon atoms in rings, but due to selection rules it is only Raman active when there are unbound carbon atoms (at the edge of a domain of graphene) [53], whereas the G (associated with bond stretching between pairs of sp^2 carbon atoms) and 2D peaks are present in all scans. This can be seen in the figure, as the monolayer is the only spectrum which shows a D peak (the monolayer scanned was similar in size to the laser spot, and irregular in shape, so that a signal is being seen from an edge).

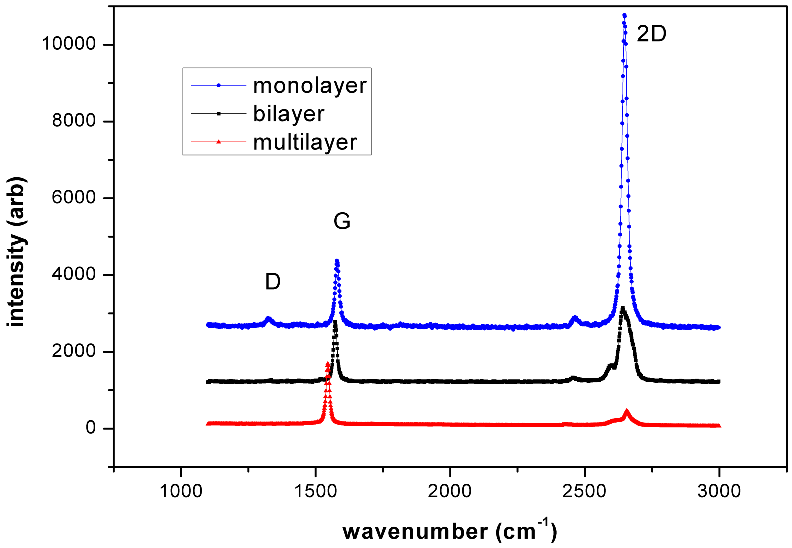

Figure 3.5: Raman data from monolayer, bilayer and multilayer graphene, prepared by the micromechanical cleavage method. Lines are offset for clarity.

Raman spectra were measured using a Renishaw 2000 Raman microscope equipped with a HeNe 633 nm laser with a spot size of ~1 μm (through a 50×

lens). The transparency of the substrate requires consideration of the surface beneath the substrate, and for this reason a piece of silicon wafer was used, as there are no spectral features from Si in the range of wavenumbers used to characterise the graphene layer.

3.3.3 Atomic force microscopy

The surface morphology of sample was investigated (at length scales of ∼100 nm to ∼10 μm) by atomic force microscopy (AFM) using a Digital Instruments Multimode SPM III. These measurements are necessarily *ex situ*, and samples are sonicated in acetone and isopropanol if the measurement is not performed immediately after removal of the sample from UHV.

3.3.4 X-ray photoelectron spectroscopy

X-ray photoelectron spectroscopy (XPS) was used in a limited capacity, to identify the species on the surface of substrates prior to annealing, after an anneal and then again after a subsequent oxygen plasma treatment (section 3.4.2). XPS identifies surface elements by exciting electrons into higher energy states using an incident X-ray beam and then collecting the photoelectrons emitted when these excited states are depopulated by the electrons. The equipment used was a VG Escalab 250 with a spot size of 500 μm. The X-rays penetrate deep into the sample, however, the electrons generated only have a limited escape depth [54, 55], which ensures the surface sensitivity of the technique. The electron penetration depth for travel through SiC $\lambda^{\mathrm{SiC}}_{\mathrm{Si(2s)}} = 25$ Å, $\lambda^{\mathrm{SiC}}_{\mathrm{C(1s)}} = 23$ Å, and in general through Carbon are 1-3 nm [56].

3.4 Device fabrication

3.4.1 Lithography

Optical (UV) lithography was used to define contact designs on the graphitised samples. The resist used, Shipley 1813 was spun at 3000 rpm for 30 seconds, followed by 2 minutes heating at 115 °C. Following exposure to UV, samples were left in chlorobenzene for 3 minutes in order to improve the sidewall profile of the pattern, which was then developed in MF319 for 80 seconds before being rinsed in de-ionised water. Metal (30 nm of titanium followed by 40 nm of gold) was thermally evaporated onto the surface and acetone was used for lift-off. These steps are close to those used for equivalent tasks across a range of materials, the only slight alterations required from a recipe which is in use for SiO_x substrates are a longer exposure (by a factor of 1.6) due to the optical transparency of the sample and a slightly thicker than standard Ti layer due to poorer adhesion to the substrate.

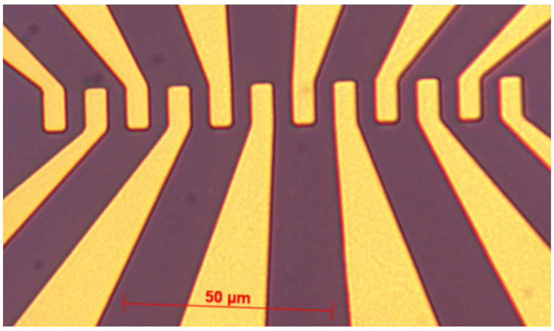

Figure 3.6: Ti(30 nm)/Au(40 nm) contacts for low-temperature measurements.

3.4.2 Oxygen plasma etching

Prototype devices with defined areas of graphene (as opposed to the sheet resistance samples measured predominantly in this thesis) were made using lithography to selectively protect areas of the sample, followed by a treatment in an oxygen plasma asher, at 50 W for 3 minutes. During development of the process, the successful etching of samples was confirmed via XPS, as the signal from the C1s peak is shifted, dependent on whether the carbon is graphitic or bonded into SiC. The C1s peaks prior to annealing shows a small graphitic peak due to surface residue; following graphitisation the ratio is reversed and the original ratio is recovered following the etching procedure.

3.5 Transport measurements

3.5.1 Low-temperature measurements

Transport measurements were made exclusively in an Oxford Instruments continuous-flow He cryostat. The sample is mounted on a stick along which run wires (twisted pairs) connected to the sample. During measurements, the sample is positioned some 80 cm from the top of the cryostat, in the centre of the solenoid, and close to the axis of the cylindrical housing. Around the sample is the VTI, and around that a jacket filled with LN_2. The system is cooled by allowing a flow of helium into the variable temperature insert using a needle valve. A temperature sensor allows accurate automated control of the temperature by means of maintaining a constant needle-valve setting and controlling a small heater.

3.5.2 Measurement apparatus

Samples were measured using a 4-probe technique, with a current being sourced between the two outer contacts to the sample and voltage measured between the two inner contacts. The equipment used was a Keithley 6221 AC and DC current source; a Keithley 2182A nanovoltmeter was used for DC measurements, and a SR830 Lock-In amplifier was used to detect the AC voltage. For dynamic conductance measurements the 6221 and 2182A were connected by a trigger cable and operated in ‘delta mode’. Control over the measurement equipment, temperature and magnetic field was achieved via in-house software based in a visual basic environment. This enabled automated measurements to be performed.

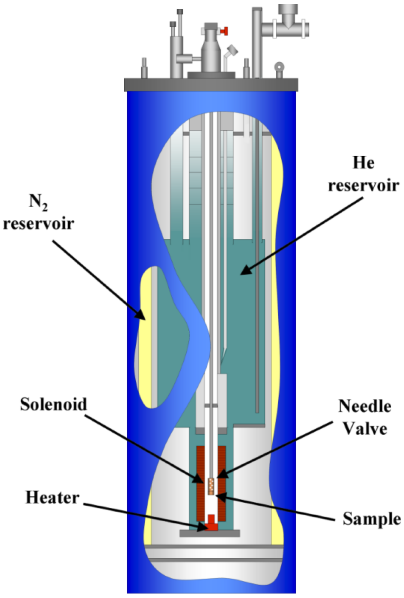

Figure 3.7: Cryostat schematic. [57]

All DC measurements used ‘current flipping’ where the current is reversed in order to nullify any spurious signal from thermal emf. Consideration was given to the magnitude of bias to use, with Joule heating a possible source of erroneous data. The low sense currents used (300 nA for the majority of measurements) are far lower than in some literature for epitaxial graphene, as although the material itself was not damaged by measuring at higher bias, the heat dissipation was kept low in order to prevent any possible effects due to sample heating [58]. For resistance of ~ 30 kΩ this corresponds to a power dissipation of 2.7 nW.

When comparison was made between samples, measured resistance was converted to a sheet resistance using a geometrical correction factor, and the samples dimensions (width W and length l) were used to convert the measured value into units of $\Omega/\square$.

3.5.3 Magnetoresistance measurements

The orientation of the applied field is vertical in the cryostat (along the axis of the cylinder), and samples were measured such that this direction was normal to the surface of the sample. the terminology ±8 T then refers to the direction of the field H, in units of μ_0H (Tesla).

At low temperatures the resistance of the Cernox temperature sensors changes not only with temperature but with magnetic field [59] hence if the machine tries to stabilise based on measured temperature, the true temperature is not constant. This is a known issue with any form of sensor and feedback mechanism, but the MR from cernox sensors is small enough that they are widely used in this capacity. The situation is more critical when the sample's properties have a strong dependence on temperature; samples discussed in chapter 5 can have a R(T) gradient of $-7\text{k}\Omega\text{K}^{-1}$ at 3 K. For this reason, measurements made at temperatures below 10 K necessitate setting the needle valve and heater settings manually, and then waiting for the temperature to stabilise. This can result in the measurement being made at a slightly arbitrary (albeit precisely measured) temperature.

The lowest temperatures attainable in the cryostat used are achieved by setting a flow of He, turning off the heater and opening the valve to the pump fully. Under these conditions the temperature can fall below 1.4 K, which is the lowest temperature for which the cernox is calibrated. At these temperatures, the MR of the cernox becomes a benefit, as it provides a means of measuring the true temperature at zero field. During magnetoresistance measurements, the software captures the temperature, and writes it to the data file produced. Data from measurements where the true temperature was slightly above 1.4 K can be used to plot measured T at a field (8 T and 4 T were used) against measured T at zero field; this plot can be seen in figure 3.8. The linear relationship means that true temperatures can be calibrated against this data, as long as the measured temperature at a field (in most cases 4 T and 8 T were used for this) is above 1.4 K. In this way it is possible to find the true temperatures for all measurement conditions used (the minimum temperature of which was 1.3 K).

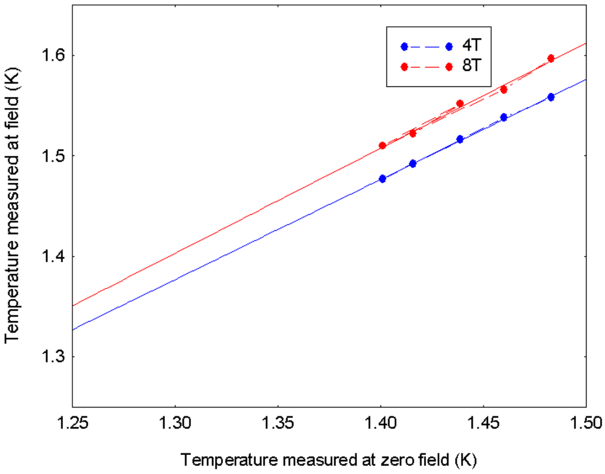

Figure 3.8: Calibration of zero-field temperatures lower than 1.4K using measured T at field.

3.6 Fitting procedures

3.6.1 Weak localisation fitting methods

The change to the conductivity, G of a disordered material in an applied magnetic field B is given in reference [60] as

$$G(B,T) - G(0,T) = \frac{e^2}{\pi h}\left[\frac{3}{2}\Psi\left(\frac{1}{2}+\frac{B_2}{B}\right) - \Psi\left(\frac{1}{2}+\frac{B_1}{B}\right) - \frac{1}{2}\Psi\left(\frac{1}{2}+\frac{B_3}{B}\right) - \ln\frac{\mathrm{B}_2^{3/2}}{\mathrm{B}_1\mathrm{B}_3^{1/2}}\right] \tag{3.1a}$$

where

$$B_1 = B_0 + B_{\mathrm{s.o.}} + B_{\mathrm{s}}, \tag{3.1b}$$

$$B_2 = B_{\mathrm{i}}(T) + \frac{4}{3}B_{\mathrm{s.o.}} + \frac{2}{3}B_{\mathrm{s}} \tag{3.1c}$$

and

$$B_3 = B_{\mathrm{i}}(T) + 2B_{\mathrm{s}}. \tag{3.1d}$$

Here Ψ is the digamma function, B is the applied magnectic field, B_0 is the characteristic elastic scattering field, $B_{\mathrm{i}}(T)$ is the characteristic inelastic scattering field, and $B_{\mathrm{s.o.}}$ and B_{s} are characteristic fields for spin orbit (s.o.), and magnetic impurity (s) scattering respectively (reference [61]). The prefix to the right-hand side of the equation is related to the conductance quantum, $2e^2/h$, where e is the charge of an electron and h is Planck's constant. As spin-orbit and magnetic impurity effects are small, $B_2 = B_3$, meaning that the first and third Ψ terms in equation 3.1a can be combined, and the final term simplified. The expression for magnetoconductance is then

$$MC = \frac{\Delta G}{G} = \eta(T)\left[\Psi\left(\frac{1}{2} + \frac{B_2}{B}\right) - \Psi\left(\frac{1}{2} + \frac{B_1}{B}\right) - \ln\frac{\mathrm{B}_2}{\mathrm{B}_1}\right] \tag{3.2a}$$

with $\eta(T)$ scaling the expression. The outputs from the fit are then $B_1 \equiv B_0$, and $B_2 = B_3 \equiv B_{\mathrm{i}}(T)$; conversion between characteristic field B_{n} and associated scattering lifetime τ_{n} is via the diffusion constant D and the expression (from reference [61])

$$\tau_n = \frac{\hbar}{4eDB_n}. \tag{3.2b}$$

In reference [62] the fit to WL only (without terms related specifically to graphene) is based on an expression in reference [32], but rewritten in order to fit directly to scattering times (τ is the transport time, τ_ϕ is the phase-coherent time) instead of characteristic fields. The expression used is

$$\Delta\rho(B) = -\frac{2e^2\rho^2}{\pi h}\left[F\left(\frac{2\tau_\phi}{\tau_B}\right) - F\left(\frac{2\tau}{\tau_B}\right)\right], \tag{3.3a}$$

where

$$F(z) = \ln(\mathrm{z}) + \Psi\left(\frac{1}{2} + \frac{1}{\mathrm{z}}\right) \tag{3.3b}$$

and conversion between field and scattering time is now

$$\tau_n = \frac{\hbar}{2eDB_n}. \tag{3.3c}$$

The expressions in square brackets in equations 3.2a and 3.3a can be seen to be equivalent. This then leads to the conclusion that for the overall expressions to be equivalent, the term η(T) in equation 3.2a would be equal to

$$\eta(T) = \frac{e^2}{\pi h} \cdot \frac{1}{G},$$

in which case there would be no need for it to be a fitting parameter. Values for η from fits are typically less than one, but trends have not been visible in temperature, although a trend with bias was observed. As measurements show a clear dependence of G on both temperature and bias, in order to investigate the parameter fully, the fit should be attempted with η(T) being separated out into component parts, so that the only truly 'free' component is visible, *i.e.*

$$\eta(T) = \chi(T) \cdot \frac{e^2}{\pi h} \cdot \frac{1}{G(0,T)} \tag{3.4}$$

where $G(0,T)$ is taken from the data at zero field. This would then be a test to see if there are trends in the free parameter χ, and (possibly) whether this is required in order to counter the contribution from interactions (such as the Altschuler-Aronov) which would tend to cause the fits to purely WL criteria to be poor.

As the quantum of conductance is defined as $2e^2/h$, equation 3.4 shows $\eta(T)$ to be dimensionless. Without the addition of the $\chi(T)$, the ratio would be equal to the inverse number of conduction channels (or the probability of a given channel). With the χ(T), this is modified so that this probability can be used to account for the temperature dependence of the scattering.

Also, from experiment, we know that this should really be written $\eta(T,V)$, *i.e.* it is bias dependent. By separating out the fit using $\chi(T)$, it would be possible to see how χ depends on the bias used.

Chapter 4

Fabrication and Surface Characterisation

4.1 Introduction

Surface measurements were used extensively during the development of the annealing procedure. Initially, these techniques were the sole means of characterising samples, and some (for samples which are not conductive) remain so. The annealing conditions for graphitisation evolved in two distinct phases. Initially (once a temperature had been found for which graphitisation occurred and the associated diffraction pattern seen in LEED) the duration of an anneal at this temperature which was required for the onset of graphitisation was explored. The assumption was that after the onset of graphitisation, subsequent layers would be grown on the initial one, and that this was not desirable. In investigating anneal durations close to the onset of graphitisation, samples were produced for which the onset had not occurred, or for which the surface was not fully graphitised. Comparisons are therefore possible between ungraphitised / incomplete samples, and samples with a complete graphene film over their entire surface. Following the successful growth of conducting samples using this method, the transport properties measured then informed the second phase, which was to raise the temperature used for the anneals in order to benefit from faster layer formation and larger resultant domains of graphene. In both cases, conclusions from surface characterisation work serve to anticipate or justify the transport properties, in terms of length scales for coherent transport. As only samples which are conductive are viable for transport measurements, and as surface data was routinely collected for all samples produced, there are data for more samples in this chapter than in the chapters on transport which follow.

Table 4.1: Samples characterised using surface techniques. Duration of single or multiple anneals (indicated by *e.g.* 10+5 for a 10 minute anneal, followed by LEED and a subsequent 5 minute anneal, all without breaking vacuum. The format for the labels (used in subsequent graphs and discussion) is temperature,duration.

Sample number	Temperature	Duration	Label
2325	1300 °C	15 + 20 min	1300,15+25
2424	1300 °C	60 min	1300,60
2438	1300 °C	60 min	
followed by	1400°C	30 min	1300,60,1400,30
2440	1400 °C	30 min	1400,30
2443	1400 °C	15 min	1400,15
2448	1400 °C	30 min	1400,30b
2449	1400 °C	30 min	1400,30c
2453	1400 °C	28 min	1400,28
2456	1400 °C	35 min	1400,35
2471	1400 °C	20 min	1400,20

4.2 Low energy electron diffraction

As introduced in section 3.3.1, diffraction patterns from graphitised SiC are widely used to characterise the thickness and order of the resulting films at various stages in the graphitisation process. Formation of graphene on the carbon-termination of the SiC substrate $(000\bar{1})$ face results in significantly different material, evidenced clearly in the differences between the LEED pattern shown previously for the (0001) face, and figure 4.1, which shows a diffraction pattern taken at 147 eV, viewed with the origin directly beneath the electron gun.

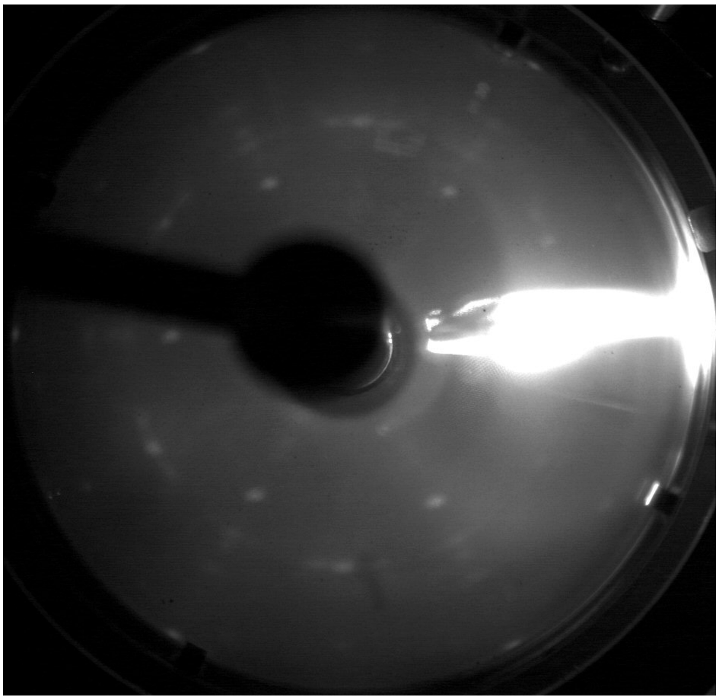

Figure 4.1: LEED image from (1400,30b) ($000\bar{1}$) taken at 147 eV. The origin of the pattern is directly beneath the electron gun.

The substrate contribution is again hexagonal (the LEED penetrates far enough into the substrate that the termination does not alter the diffraction pattern for these opposite faces), and a faint 2×2 reconstruction can be discerned, as in reference [63]. The contribution to the diffraction pattern from the overlayer for this face consists not of spots, but rings, centred on the same origin as the hexagonal pattern. This is indicative (for diffraction in general) of rotational disorder (the constant radius of the rings is dependent on the carbon bond-length), and also specifically of graphene grown on this face of SiC (references [44, 64]). Closer inspection shows that there is structure to the rings, which is explained as being due to several preferred orientations of carbon layers with respect to the substrate, and it should be emphasised that this is a structure which is distinct from turbostratic carbon (in which material there is no rotational order between the stacked layers). This stacking geometry on the $(000\bar{1})$ face can preserve the monolayer electronic properties despite several layers being present, as each layer is electronically decoupled from adjacent planes [44]. If the surface were a single-crystal monolayer, the argument for dashed lines would not be relevant, as there would be no rotated domains. The structure seen here could be the result of a monolayer consisting of rotated domains, or several layers (with or without in-plane rotation) rotated with respect to each other.

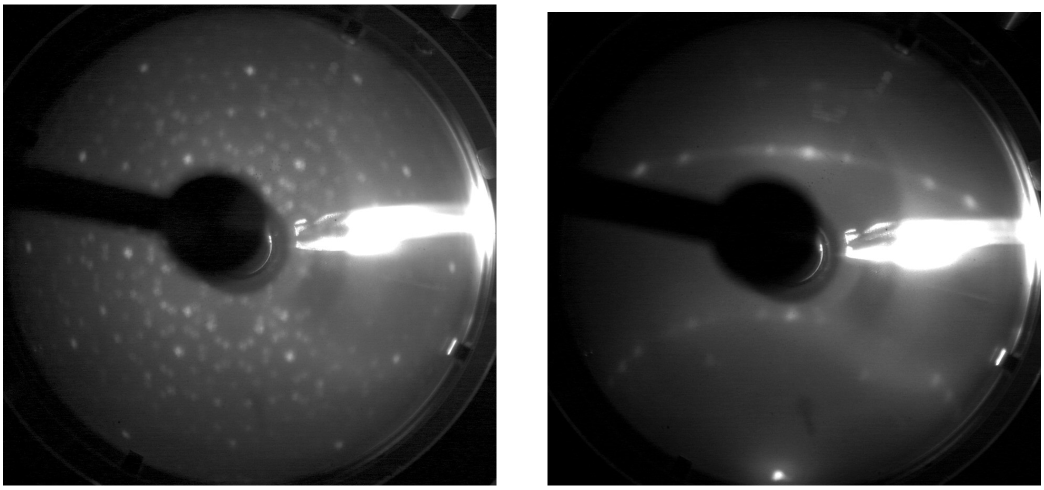

(a) (b)

Figure 4.2: LEED patterns from the $(000\bar{1})$ faces of (1400,28) (at 183 eV) (a) and (1400,35) (at 92 eV) (b).

For samples which are not fully graphitised, a change can be seen in the diffraction pattern as a result of intermediate stages in the process. In some cases (especially for samples annealed at 1400 °C, where any temperature gradient would be more marked) it is possible to see both types of diffraction pattern on the same sample. In regions where these reconstructions are seen it is not possible to obtain a diffraction pattern at energies below ~120 eV, which is understood as being due to charging of the surface (in agreement with a non-conducting intermediate stage in the graphitisation). This, and the geometry of the equipment, constrains the alignment choice to that with the electron beam normal to the sample, in order for the diffraction patterns to be as clear as possible. Figure

4.2a shows a representative image for the pre-graphitisation reconstruction. The diffraction pattern appears similar to the $(2\sqrt{3} \times 2\sqrt{3})R30^{\circ}$ reconstruction seen in reference [65] on the (0001) face of 6H SiC. The pattern is interpreted as being due to silicon adatoms on the surface; the source of this silicon is the substrate, and the pattern therefore indicates that the top few layers of SiC are silicon-depleted, referred to from here on as carbon-rich due to the focus of this work. This reconstruction has not previously been reported for the $(000\overline{1})$ face of 4H SiC, which is taken to be a consequence of the changing focus of research into graphitised SiC, as described in section 2.5. The observation of such a precursor stage indicates both that the process is well-controlled (at the temperatures used it is possible to halt the process at sub-monolayer coverage) and that the anneal durations used corresponded closely to the time taken for the surface to become fully graphitised. These conclusions are key to interpreting both other surface data and also the measurements of electronic transport properties.

The dashed rings can be seen more clearly if the sample is tilted relative to the electron beam, so that the origin is at the edge of the screen (for this reason this is the orientation for figure 4.2b). The duration of anneal was longer than for the sample for which LEED is shown in figure 4.2a, indicating that this is an intermediate stage in the graphitisation process.

Sample (1300,60,1400,30) underwent an annealing procedure which offers further insight into the growth process. This sample was the first to be annealed with a sapphire cap, and was initially annealed at 1300 °C for 60 minutes, as described in section 3.2. This 60 minute anneal did not result in graphitisation, presumably because the effective sample temperature was lower than for uncapped anneals. At this point, images from LEED of the sample show the same reconstruction seen in figure 4.2a. After a further anneal at 1400 °C for 60 minutes the dashed rings signature was seen, confirming that the reconstruction is, indeed, an intermediate stage in the graphitisation process. In samples where reconstruction and the dashed rings structure are seen depending on the region scanned, the ring structure still indicates rotational disorder, showing that for these samples each layer, including the first, can have domains rotated with respect to each other, as seen in [66]. For higher temperature anneals, the growth dynamics (even when using an atmospheric pressure of Ar to slow the Si egress) mean that monolayer coverage is difficult to achieve [42, 67]. In the case of samples presented here, with the high mobility of carbon over the surface at high temperatures, it is unlikely that there are multiple layers. The estimation of the layer count being between one and four cannot however be refined solely on the basis of this argument, and additional measurements (using other techniques) are required.

The diameter of the LEED beam which intersects with the sample is approximately 1 mm. This means that any diffraction pattern is the result of an average over many of even the largest graphene domains produced in this study. This means that large areas of the sample can be scanned (by moving the plate on which the sample sits laterally), but that it is insensitive to small defects, whereas these are critical to the transport properties.

More detailed analysis as in references [49, 68] (following a repair to electron-gun damage which is responsible for the streak on this and subsequent images) would yield additional information. The only face of SiC used for this technique in published literature is in reference [49], for the (0001) face, but equivalent consideration of intensity ratios for the SiC and graphene features from the $(000\bar{1})$ face should enable an equivalent procedure to be used.

4.3 Raman spectroscopy

Raman spectra for graphene on SiC consist of the same peaks introduced in section 3.3.2. The spectra obtained and the interpretation share similarities with those for flake graphene, but some details can help to characterise features which are more relevant in the case of epitaxial graphene.

The presence of the D peak due to dangling bonds (found at the edges of graphene layers) was introduced in section 3.3.2. The fact that this feature indicates edges, while the G peak indicated the presence or quantity of graphene is important for smaller domains of graphene, as the ratio of intensity for the G and D peaks can give an indication of the contributions from edges, and hence the average grain size within the area being scanned [69, 70].

This analysis is straightforward for spectra from samples on SiO_2, as in figure 3.5, however for graphene grown on SiC substrates, further consideration is necessary before such peak areas can be calculated. The substrate has several spectral features which are at very similar wavenumbers to the graphene G peak, as shown in figure 4.3. These complicate the spectra acquired, and require careful subtraction in order to obtain accurate ratios. In order to subtract the contribution from the substrate, it is necessary to take an equivalent spectrum from a bare piece of SiC. However, simply subtracting this spectrum is not sufficient. As the graphene is on top of the SiC, it attenuates the laser intensity (both incident and reflected) in addition to adding specific spectral features, and this effect must be included in any subtraction process. One benefit of this attenuation is that it can be used to estimate the thickness of the graphitic overlayer, providing support for thickness estimates from other techniques. This is important as (unless the individual domains of graphene are larger than the laser spot size (2μm)), the ratio of 2D to G peak heights cannot be used, as it is for flake graphene.

Finally, the spectral shape of the 2D feature allows monolayers to be distinguished from bilayers and samples with more than two layers. For a monolayer, the peak can be fit using a single Lorentzian function. For more than one layer, the peak must be decomposed into four individual Lorentzian shapes in order to be adequately described as in [71, 72] for the (0001) face. A combination of this approach and the position and width of the 2D peak is used in reference [73].

The attenuation, ratio of the areas of D and G peaks, and characteristics of the 2D peak are discussed in the following subsections.

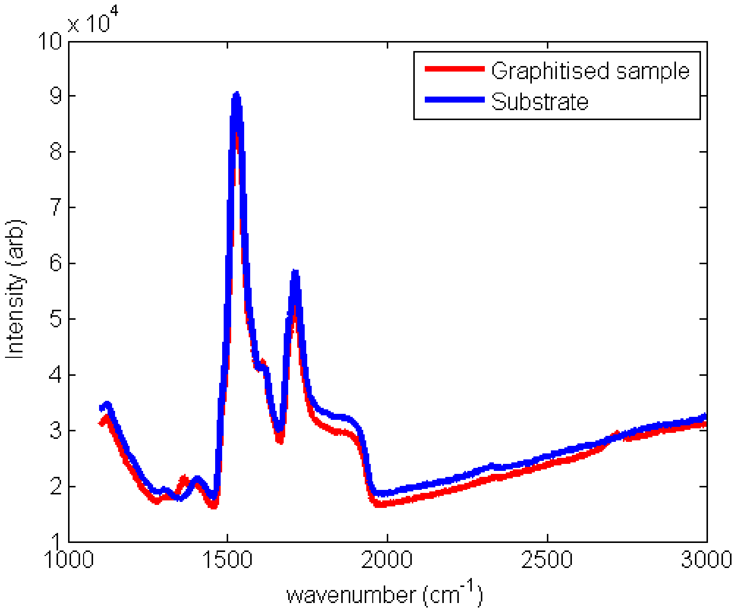

Figure 4.3: Raman spectra for SiC substrate and graphitised sample, showing the proximity of substrate peaks to the graphene G peak.

4.3.1 Raman attenuation and graphene layer thickness

This procedure relies on the Beer -Lambert law, expressed in terms of the intensity from the sample (I_{sample}) and from a reference substrate (I_{ref})as

$$\frac{I_{\mathrm{sample}}}{I_{\mathrm{ref}}} = \exp(-2\alpha t) \tag{4.1a}$$

$$\frac{I_{\mathrm{ref}} - I_{\mathrm{sample}}}{I_{\mathrm{ref}}} = -2\alpha t \tag{4.1b}$$

where α is an optical absorption coefficient, t is the number of graphene layers and the factor of two comes from considering incident and reflected light.

Measuring the attenuation of the Raman signal from the SiC substrate can therefore identify the thickness of the overlayer. In terms of experimental procedure this requires two spectra, one of the graphitised sample and one of an equivalent bare substrate. Ideally these would be from a single graphitised sample with an area of graphene removed (*e.g.* by O_2 plasma etching), however a spectrum taken from a piece of substrate from the same wafer can also be used. Using a spectral feature of SiC at 1519 cm^{-1} [74], a plot is made of the intensity of the substrate signal ($I_{\text{substrate}}$) on the abscissa vs ($I_{\text{substrate}} - I_{\text{sample}}$) on the ordinate, and the fitted gradient from this graph is used to find the layer thickness t (see figure 4.4). Determination of α was achieved via the same procedure, but using mechanically cleaved graphene and the 520 cm^{-1} silicon Raman peak (it is assumed that the attenuation is the same for epitaxial and cleaved graphene, and that α is independent of wavelength for the range in question). For these flake graphene samples, monolayers and bilayers can be identified clearly; and values of α found were 0.015 per layer [75], which compares with published values of 0.02 [76] (using a 488 nm excitation wavelength).

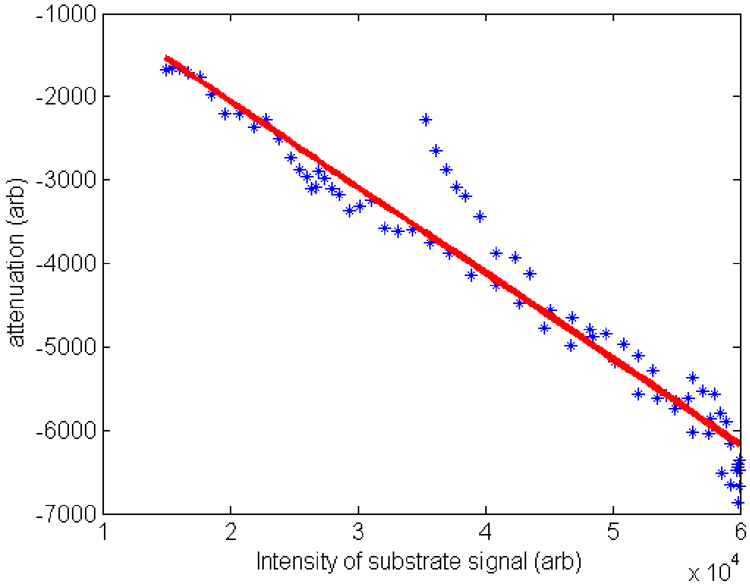

Figure 4.4: Attenuation of Raman signal as a function of substrate intensity.

4.3.2 Raman peak ratio and grain size

Following the SiC attenuation procedure, it is possible to perform a more accurate subtraction of the substrate signal, in order to isolate the Raman signal from the graphene. The spectrum from the substrate is modified using the gradient and intercept from the graph described in the previous section (this is equivalent to $I_{\text{substrate}}\exp(-2\alpha t)$) and this is used to calculate a corrected substrate (as shown in figure 4.5. This signal is then subtracted from the measured spectrum from the graphitised sample. The result of these operations is shown in figure 4.6, where the spectral features are now seen on a near-zero background.

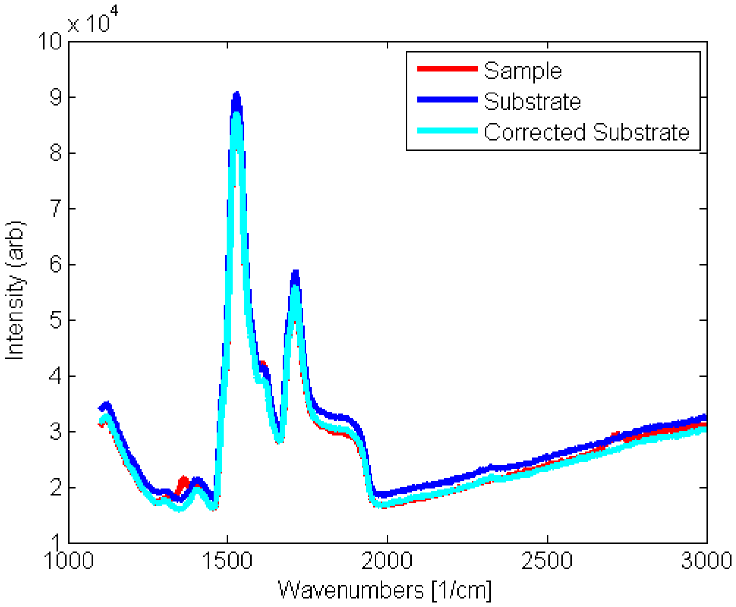

Figure 4.5: Raman spectra for sample (1400,30c) and for an un-annealed substrate. These spectra are then used to calculate a corrected substrate signal prior to subtraction from the spectrum from the graphitised sample.

The integrated intensities (areas) of the D and G peaks are found from this graph and used to calculate the size of the graphene grains using equation 4.2, from reference [70]:

$$L_{\alpha} = \left(2.4 \times 10^{-10}\right) \lambda_{\mathrm{l}}^{4} \left(\frac{I_{\mathrm{G}}}{I_{\mathrm{D}}}\right) \tag{4.2}$$

where L_{α} is the lateral grain size, λ_{l} is the incident laser wavelength (both in nanometer units) and I_{D} and I_{G} are the integrated intensities of the D and G peaks, respectively.

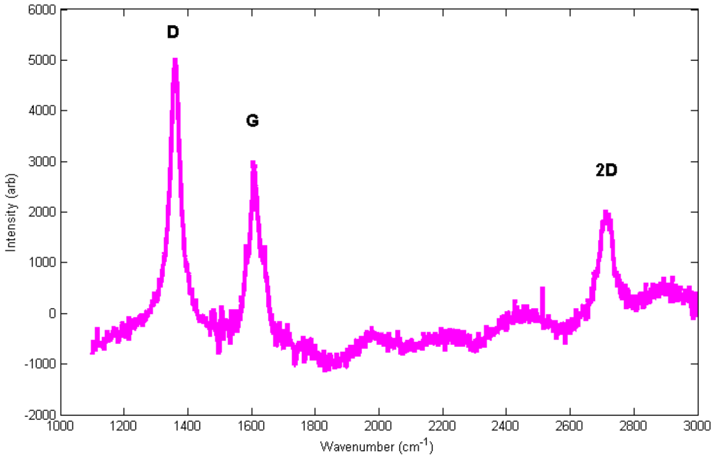

Figure 4.6: Raman spectra for sample (1400,30c) following removal of substrate signal.

The sizes of grain are obtained from this procedure are (16±2 nm) for samples annealed at 1300 °C. A very similar grain size is obtained for samples annealed at higher temperatures, contrary to what is seen in AFM micrographs; this discrepancy is discussed in section 4.3.4.

4.3.3 Fitting the 2D peak

As with the D and G peaks, in terms of significance for structural determination of graphene sheets the 2D peak's origin and interpretation is more straightforward for sheets which are isolated and of large lateral size relative to the laser spot; properties of these (mechanically cleaved) graphene flakes serve as a useful introduction. The two characteristics of the 2D peak which are of interest are the position (in cm^{-1}) and the structure of the peak (width, and accuracy of fit to one or multiple Lorentzian components). For flake graphene on SiO_2 the 2D peak is present at $2678 \pm 1.0\ \mathrm{cm}^{-1}$ (for an excitation wavelength of 532 nm) and can be fit by a single Lorentzian [71, 77]. As the number of layers increases, the peak position moves to higher wavenumbers, and multiple Lorentzian components must be used to fit the peak shape.

For epitaxial graphene, the situation is complicated by the fact that the graphene is likely to be under compressive strain [72], and also because (unless the size of graphene domains is larger than the laser spot) the average layer thickness can be non-integer, and also less than one. The strain causes a shift in the position of the 2D peak to higher wavenumbers, from which position there is an additional shift due to the number of layers present; for epitaxial graphene this layer-dependent shift is to *lower* wavenumbers with additional layers [72, 78]. Importantly, the trend is not valid for sub-monolayer coverage (possibly due to more effective strain relaxation by small domains); the peak occurs at lower wavenumbers for $n \leq 1$ than for $n = 1$ [72]. Finally, the multiple-Lorentzian requirement for epitaxial graphene 2D peaks is the same as for flake graphene with the slight variation that the FWHM for disordered films is larger than for flake graphene or more ordered epitaxial films [73].

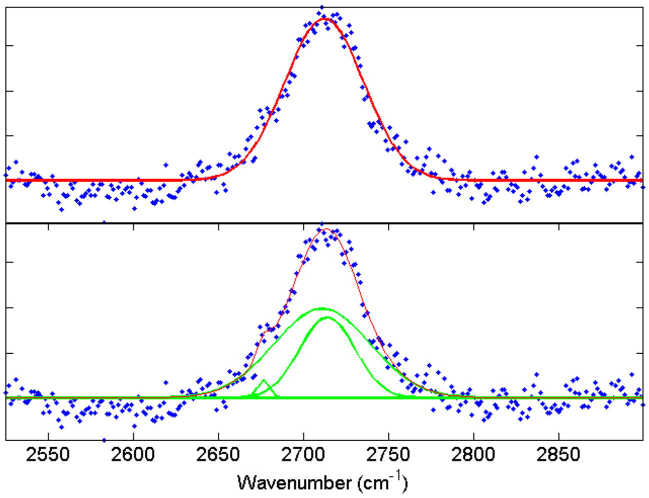

Figure 4.7: Raman 2D spectral peak for sample (1400,30c) following removal of substrate signal, fitted with a single and four individual components. A single component is sufficient, and will be used henceforth.

Representative data for a sample characterised in this way is shown in figure 4.7; the 2D peak has a position (2712 cm^{-1}) which is lower than that for complete epitaxial layers, indicating sub-monolayer coverage, and a FWHM (54 cm^{-1}) which agrees with a relatively disordered epitaxial layer. The fit to a single component peak (the 4-component fit has two peaks within 3 wavenumbers of each other and one which has a height which is near-zero), as well as the attenuation for this sample (which indicates a coverage of 0.8 layers) corroborate these conclusions.

4.3.4 Raman discussion and conclusions

The diameter of the laser spot which initiates the Raman scattering is approximately 2 μm. The consequences of this are that only a small area of the sample is characterised, even with multiple scans. For the largest domains of graphene produced in this study, the spot still covers many grains, and the spectra are therefore a representation of aggregate features. The dimensions of the spot are similar to those of electronic devices, and, if representative, should give an indication of the transport properties which can be expected.

For regularly shaped domains of graphene the equation for grain size is valid (domains for samples annealed at 1300 °C are well described by the formula); the validity decreases further from these conditions, as can be demonstrated by considering either a large domain or one with very irregular edges. Conversion between the 'edge length ' and grain size is presumably based on the assumption of a regular shape, which isn't true for the morphology seen, and which would lead to underestimates of the size; this would explain the discrepancy grain sizes from the Raman and AFM data.

A method for identifying graphene layer thickness using the attenuation of Raman signal from the substrate is presented. This is similar to the methods published recently [76] but does not rely on a confocal microscope. Results from this attenuation method give a thickness of 0.8 layers for the sample shown, in agreement with the position and structure of the 2D peak.

4.4 Atomic force microscopy

Data from LEED and Raman microscopy appear to present slightly conflicting information about the surface graphitic layer, with LEED (especially of the (0001) face) indicating extremely good order with respect to the substrate and Raman spectra showing evidence of disorder; AFM micrographs demonstrate how these conclusions are not mutually exclusive. The micrographs show a granular surface, with lateral sizes which are seen to depend on annealing conditions. This completes the picture of the nature of the surface material, in a qualitative sense. Each grain is ordered (crystalline) and epitaxial, *i.e.* as shown by the LEED, but grain boundaries and other possible defect sites lead to the incomplete bonds associated with the spectral features seen in Raman spectra. While AFM provides no information as to the relative alignment of the crystal lattice between these grains, they provide the edges which influence the Raman signal, and the LEED patterns seen provide evidence that they are all oriented the same (in the case of the (0001) face), and oriented in specific directions (on the $(000\overline{1})$ face) with respect to the substrate.

In addition to complementing and strengthening conclusions from other techniques, the first major contribution made by AFM is to show a clear difference between samples annealed at 1300 °C and 1400 °C, as seen on micrographs shown in figure 4.8. The lower temperature anneal has resulted in a graphitic covering, which varies in height by only a few nanometers over a 1 μm scan, but which consists of grains with a diameter of approximately 20 nm. The higher temperature anneal results in a similarly flat surface, but with far larger domains (generally 100s of nm, and with some approaching 1 μm), where any height changes coincide with well-defined, faceted edges between domains. This difference in lateral size can be expected to result in significantly altered electronic transport properties between the samples.

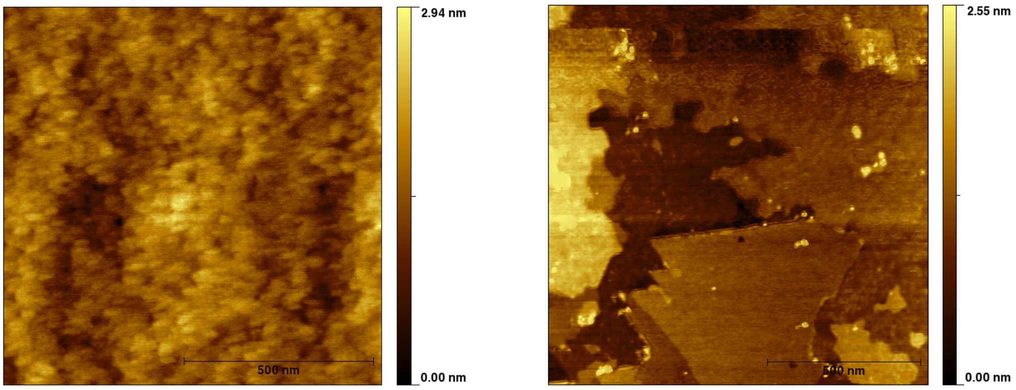

(a) (b)

Figure 4.8: AFM micrographs from (1300,60) (a) and (1400,15) (b). The size of the scan in each case is 1μm

There are some limitations to the conclusions which can be drawn from the AFM data. One concerns the lack of a datum. As the AFM does not distinguish between conducting and insulating areas of the substrate, it is not possible to tell if a given flat section of the micrograph is substrate or graphene. This piece of information is important for several reasons. Firstly, it assists the formation of a definite conclusion as to whether the film is continuous. If the film is incomplete, then the relative heights of the graphene and substrate layers can be interpreted in terms of the type of nucleation site for the graphitisation (see section 2.5). It is possible that the most significant layer, in terms of electronic transport, could be beneath the raised mesas which are seen. Without a conducting tip, the height change as a result of chemical contrast can be difficult to distinguish from a genuine topological feature. The micrographs, for the small areas which are scanned, show a level of detail which is important for the length scales of devices used for electronic transport, but this is balanced by questions over how representative any given scan is of the sample.

As described in section 4.2 sample (1300,60,1400,30) had an anneal of 1300 °C for 60 minutes with a sapphire cap, after which LEED showed the reconstruction prior to graphene. As anneals of 60 mins at 1300 °C for uncapped

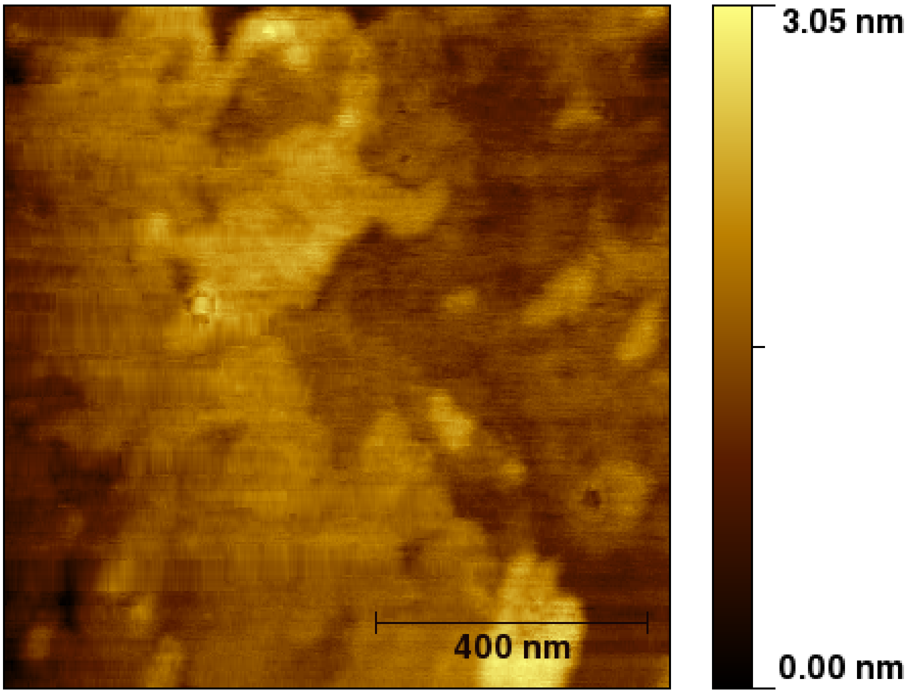

Figure 4.9: AFM from (1300,60,1400,30). Despite the initial conditions being the ones which are a precursor to the 20 nm grain size, the size of grain seen is the same as that for samples which have only been heated at the higher temperatures.

samples resulted in samples with graphitised surfaces (albeit 20 nm grains) this is presumably an indication that the surface temperature was slightly lower due to the cap. Given that uncapped samples at 1400 °C have since been seen to have domains of 300 nm and greater in extent, there is nothing to suggest that the surface of sample (1300,60,1400,60) at this stage would have been any different to the precursor to 20 nm grains. The upper layers are carbon-rich, and any defects should be those inherent to the substrate, hence similar across samples.

Following *ex-situ* cap replacement and a re-anneal at 1400 °C for 30 minutes, the domain sizes were 300 nm. The question is, what happened to the 20 nm-scale defects or precursor morphology? The accepted mechanism is that on the $(000\bar{1})$ face, new layers are formed from the lowest graphene layer; this would mean that the first layer formed is the top one. If the immediate precursor to 20 nm grains is later (after a 1400 °C anneal) seen to have grains of lateral dimension 300 nm, then the conclusion must be that the carbon is extremely mobile (at 1400 °C). This mobility means that the potential exists to decouple the processes of nucleation and propagation. Recently [43] it seems accepted that high mobility of step edges is the case, but this is not necessarily the same as carbon mobility, as the oval grain shapes for the less ordered material are unlikely to correspond to an underlying morphology. Step-bunching is inevitable via the motion of step edges, and can be used to increase the size of the plateaux, but has the drawback that it involves larger step heights. If the trade-off between these two features is not desirable, then sample (1300,60,1400,60) indicates a possible alternative template for a two-stage growth procedure, with (i) being production of excess carbon, and (ii) being coalescence, leading to fewer step bunches.

4.5 Scanning tunnelling microscopy

Preliminary STM measurements have been made on a selection of samples, as the initial stages of collaboration with the University of York. The resolution achieved was limited by the STM tip used, hence the detailed images of the surface, showing the real-space interference between the two lattices [79] were not obtainable. The initial attempts do, however, add important detail to the evidence from the more comprehensive measurements using other techniques. Specifically, STM combines the ability to probe small areas with a local sensitivity to species (or at least conductivity).

Some samples are far harder to contact and these are samples where the LEED charges at low energy. The assumption is that they are not continuous films, which makes the technique of limited additional use to AFM in terms of identifying nucleation details. For samples which do allow contact, all areas scanned can be fully imaged (the lowest level in a given image conducts, and may well dominate the transport properties), although is it difficult to gauge how representative this is. Also, there is still the issue of the size of the area probed, and

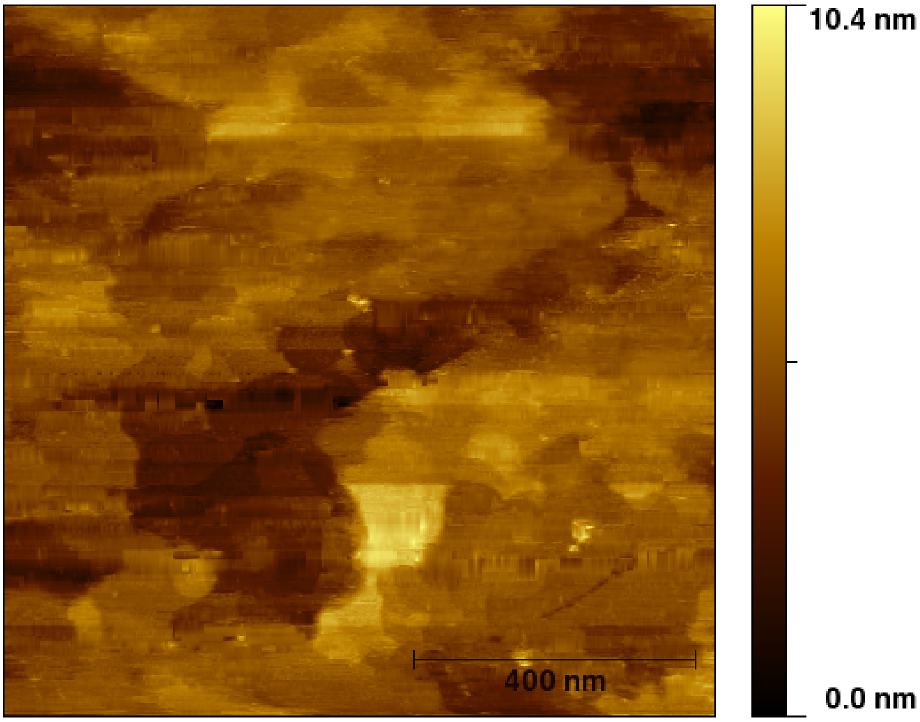

Figure 4.10: STM micrograph from (1400,20).

how representative this is of the sample as a whole, and the conducting properties.

As with AFM, there are many mesas raised up from the lowest level as seen in figure 4.10, and the temptation is to focus on these and their step heights. However, unlike AFM, the STM can address the question of whether the lowest visible layer (in many images this seems to provide a single height beneath many distinct mesas of differing heights) corresponds to substrate or surface graphene. For a sample which had shown LEED to low energy (and which was contactable on every attempt) one of these flat areas was successfully imaged within the capabilities of the tip at that time. The surface was conducting, and had an rms roughness of only 0.13 nm over a 40 nm square scanned area. With a better tip, it should be possible to achieve atomic resolution, hence linking the quality of the samples to published data and to the transport studies discussed here. Conducing SiC substrates would enable ungraphitised areas to be investigated by taking $I(V)$ spectra.

Finally, domains can be seen which are the same height but have a different appearance - it is possible that these are rotationally shifted with respect to each other (atomic resolution would be needed to see this, as in [80]).

4.6 Discussion and conclusions

The data from the various techniques presented here can be combined to gain a comprehensive idea of the characteristics of the graphitic films produced, to deduce some aspects of the growth mechanism and to anticipate the transport properties which can be expected.

The first conclusion is that the material produced is epitaxial. This conclusion (order with respect to the substrate) is compatible with the disorder deduced from the Raman data once the SPM is considered, and these techniques combine to indicate a polycrystalline material with grain sizes (from SPM) of 20 nm for anneals at 1300 °C, increasing to 300 nm for anneals at higher temperatures.

The Raman grain size from the samples annealed at higher temperatures is smaller than that seen in AFM data. This could be due to the penetration depth of the laser, and buried layers being disordered, or from lattice defects which do not constitute edges as identified by AFM, but the most likely cause is the very irregular shapes formed by the graphitic layer.

LEED data and Raman spectra show an apparent sensitivity to anneal duration, although there is no obvious relationship. This is interpreted as being due to samples being just on the verge of forming a complete layer, where conditions for individual anneals vary sufficiently that for these durations the critical point in the growth process fluctuates. Future annealing procedures at any given temperature should be continued for longer following the onset of graphitisation in order to remove this uncertainty. For the samples presented here, the conclusion is that it is likely, given the fact that most samples are annealed close to the onset of surface coverage, that the surface is not fully continuous.

Larger-area graphene domains resulting from higher temperature anneals should not be unexpected, if the system is considered in the context of carbon deposition and coalescence in a wider sense. While the temperatures used in early epitaxial graphene work were influenced by [36], and while there can be consequences for the thickness of the layer based on anneal temperature, if the issues of carbon supply, SiC substrate and bond formation are considered independently, the literature [70] would lead to a choice of temperature (based on sp^2 bond formation alone) higher than 1600 °C. Within the constraints set by a decomposition process, a combination of low temperature for carbon provision, and then high temperature for coalescence is identified as a potential improvement which could avoid the issues of step bunching and domain size being intrinsically linked.

Despite the general characteristics provided by these techniques, in general, surface techniques do not provide enough insight into the film's properties over a scale required for devices. Even when the area interrogated by the technique is similar to the size of a device, the techniques can still be incapable of ascertaining the properties with respect to the primary motivation for studying graphene - the electronic transport properties. In order to achieve this, transport measurements are needed.

Chapter 5

Transport properties: the effect of anneal duration on film continuity and disorder

5.1 Introduction

Samples annealed in UHV conditions as described in section 3.2.2 show LEED characteristics indicating the presence of an ordered graphitic surface system for annealing procedures with temperatures above 1275 °C and involving continuous durations longer than 15 minutes. Once contacts (voltage probe separation 5 μm) have been patterned using standard optical lithography (as described in section 3.4.1), these samples are measured in a constant-flow helium cryostat as described in section 3.5.1 in order to characterise their sheet resistance properties in magnetic fields H of up to μ_0H = 8 T and temperatures down to 1.4 K. Although it is possible to identify conditions required for the onset of graphitic growth (activation temperature) the data using Raman microscopy and LEED techniques show very little difference between samples. The AFM micrographs mentioned in section 4.4 were taken following a period of time spent attempting to draw conclusions from the transport data alone; in terms of chronology it is the micrographs which support the conclusions drawn from the transport data, and not *vice-versa*. In any case, it is not possible to positively identify areas of graphitised surface as distinct from un-graphitised substrate using AFM. The measurements and interpretations which follow are predominantly for samples annealed at 1300 °C for varying durations, and enable samples to be distinguished via their transport properties so that the characteristics corresponding to the onset of continuous films can be identified.

Table 5.1: Samples annealed in UHV conditions. Annealing conditions summary. Duration of single or multiple anneals (indicated by *e.g.* 10 + 5 for a 10 minute anneal, followed by LEED and a subsequent 5 minute anneal, all without breaking vacuum).

Sample	Temperature	Duration	Label
2316	1535 °C	60 min	1535,60
2331	1300 °C	20 + 15 min	1300,20+15
2366	1300 °C	15 + 10 min (etched mesa)	1300,15+10
2374	1275 °C	5 + 10 + 20 + 30 min	1275
2412	1300 °C	60 min	1300,60
2414	1300 °C	90 min	1300,90
2421	1300 °C	45 min	1300,45

5.2 Temperature-dependence of film resistance

As samples are cooled, there is significant change in the resistance of all samples, and a variation between samples which can be linked to annealing conditions. Samples annealed for 15 or 20 minutes at temperatures of 1300 °C or lower become effectively insulating at temperatures below ∼50 K; a longer anneal produces samples which conduct down to the lowest temperatures attainable in the system (∼1.3 K). There is an indication that successive short anneals graphitise the surface less effectively than a single longer anneal for the same total duration; as samples were treated identically prior to graphitisation this suggests that there is a propagation process from nucleation to the formation of a continuous layer which takes an appreciable length of time at these temperatures.

Figure 5.1 presents data for the samples listed in table 5.1. In all cases the resistance vs temperature (RvT) graphs are strongly non-metallic, with an increase in resistance of several orders of magnitude between RT and 5K. Data from LEED, Raman and XPS all support the conclusion that the surface is graphitic; the fact that the resistance varies in this way with temperature is an indication of the morphology of the surface material as in HOPG [81] and crystalline graphite [82]. The variations between samples' RvT should therefore provide insight into these properties, and from them conclusions can be drawn as to the growth mechanism for the graphite layer.

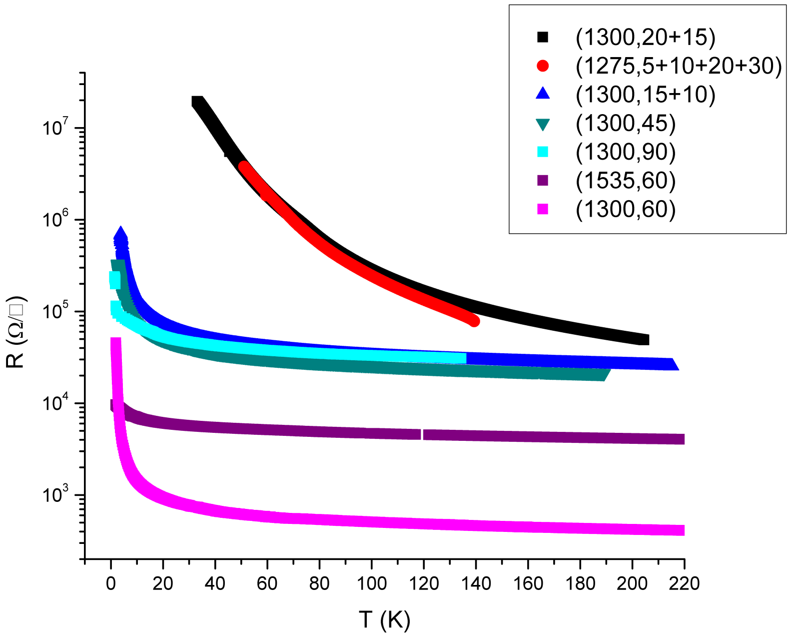

Figure 5.1: Resistance measured using a four-point technique, with a 300 nA DC bias. Cooling curves are for the various samples listed in table 5.1.

5.2.1 Localisation

The appearance of AFM micrographs (section 4.4) show that despite crystallinity, and epitaxial order with respect to the substrate (as shown by LEED), the graphitic layer produced by annealing in UHV consists of grains of order 20 nm in lateral size (a value corroborated by Raman spectroscopy). Such a disordered material could not be expected to exhibit ideal electronic properties, and there is an extensive literature on conduction through disordered materials, including various forms of carbon [83, 84, 85].

The cooling curves are the first indication that changes to the annealing procedure result in measurably different material. This can be assessed in a more systematic way by plotting graphs based on some candidate regimes. As the change in conduction properties with temperature is different in each case this should allow identification of the regime(s) which describe the conduction in these samples.

Conduction electrons in disordered material systems can be localised by scattering from impurities, leading to weak localisation (section 2.3.2). The conductivity (G) is corrected in a temperature dependent way [86] as a result of the ratio of elastic (τ_0) and inelastic (τ_i) scattering times, expressed as

$$G = \left(\frac{ne^2\tau_0}{m}\right)\left[1 - \frac{1}{\pi k_\mathrm{F} l}\ln\left(\frac{\tau_\mathrm{i}}{\tau_0}\right)\right], \tag{5.1}$$

where the first term is the Drude conductivity with n the electron density, e the electron charge and m the effective mass of an electron. In the correction term k_F is the Fermi wavevector and l the localisation length. As the inelastic scattering time is temperature dependent, while elastic scattering times are independent of temperature, the correction to the conductivity becomes larger at lower temperatures, as elastic scattering begins to dominate.

Figure 5.2 shows data for R vs T plotted on axes suitable for this WL expression (*i.e.* a straight line would indicate agreement). For data from RT to 5 K there is clearly poor agreement (the log scale on the second graph is included simply to enable the data to be represented on a single plot, and is not a suitable choice of axis for identifying a WL temperature dependence).

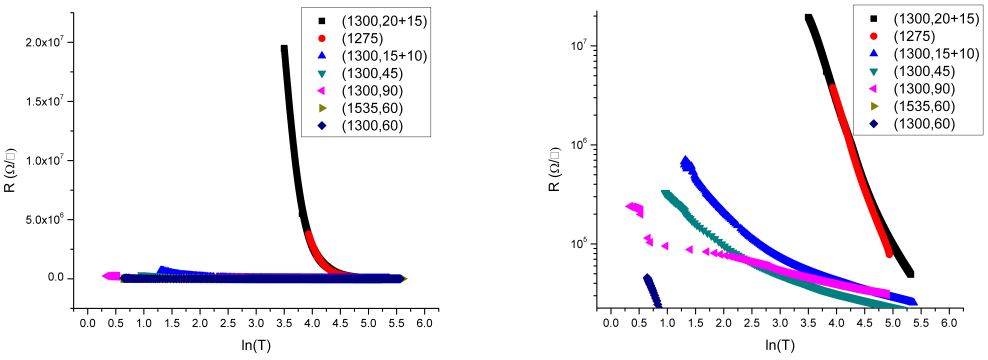

(a) (b)

Figure 5.2: WL plots for UHV grown samples (a) and using a log-scale for the resistance (b).

5.2.2 Variable range hopping

Another candidate regime is variable range hopping (VRH) (section 2.3.1). For Mott VRH [29] the expression for the variation of resistivity ρ with temperature T is

$$\rho = \rho_0 \exp\left(\frac{T_n}{T}\right)^{\frac{1}{n+1}}, \tag{5.2a}$$

where

$$T_{\mathrm{n}} = \frac{24}{\pi k_{\mathrm{B}} \xi^3 N(E_{\mathrm{F}})}, \tag{5.2b}$$

n is the dimensionality of the sample and ξ is the localisation length [60].

Resistance data above 5K for all UHV grown samples measured can be described using the assumption of a variable range hopping regime, figure 5.3. The good fit to the Mott 2D plot is readily understood in terms of the system being studied (any few atomic layers of conductive material on an insulating surface should exhibit 2D behaviour). The resistivity of films in this regime is described by equation 5.2a, which informs the choice of axes for figure 5.3. Plotting using axes for a 3D system, (*i.e.* a $T^{-1/4}$ exponent) results in lines which are still approximately straight, but with lower R^2 values for linear fits.

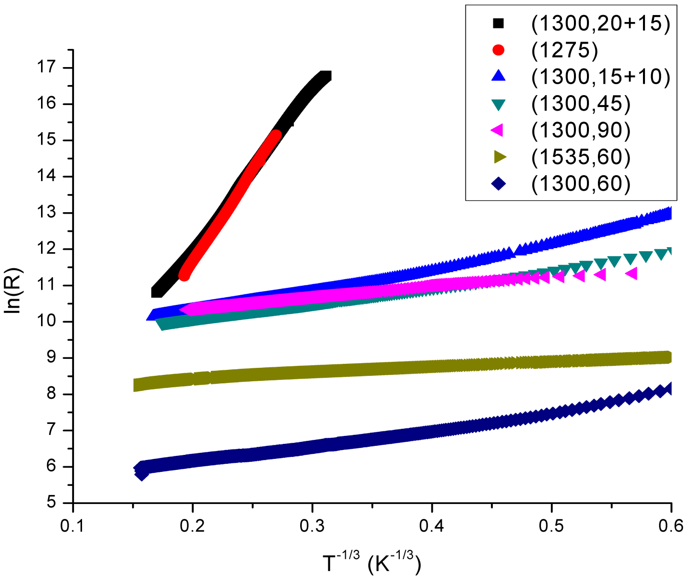

Figure 5.3: VRH Plot for Mott regime in two dimensions (leading to a $T^{-1/3}$ exponent), plotted for data above 5 K.

The range of characteristic temperatures extracted from these plots provides a way to distinguish between sample preparation conditions. The Raman and AFM data (sections 4.3 and 4.4) indicate a disordered, granular surface, and this is supported by the hopping regime seen in the transport data. The data are consistent with grains whose size appears independent of anneal duration. The transport data, however, for samples (1300,20+15) and (1275) which were annealed for shorter periods of time or lower temperatures show far higher values of T_n, and although unquantifiable due to unknown $N(E_F)$, lower values for ξ. The relationship between anneal duration and gradient (hence ξ) does not seem to be a proportional one. Rather, there seem to be two distinct values, with samples falling into two categories, A and B, where those in category A had continuous anneals of more than 45 minutes and B did not. The exception to this rule is sample (1300,15+10), which was etched to remove graphene from the surface, leaving a mesa around the contact electrodes, as described in section 3.4.2.

5.2.3 Electron-electron interaction

In disordered systems where electron-electron interactions are significant, equation 5.2 is no longer applicable. The expression describing $\rho(T)$ for this Efros-Shklovskii (ES) VRH regime [87] is

$$\rho = \rho_0 \exp\left(\frac{T_n}{T}\right)^{\frac{1}{2}}, \tag{5.3a}$$

where

$$T_n = \frac{e^2}{\pi\epsilon_0\epsilon_\mathrm{r}k_\mathrm{B}\xi}. \tag{5.3b}$$

here relative permittivity of the of the material is included as ϵ_r, and the permittivity of free space as ϵ_0.

Figure 5.4 shows the RvT data plotted on axes suitable for the Efros-Shklovskii electron-electron interaction. It can be seen that the data also fits the Efros-Shklovskii formula, indicating that there could be a degree of electron-electron interaction in the samples being studied. It should be mentioned that this choice of axes would also be appropriate for a 1D Mott VRH system. Again, the data fall onto two distinct gradients, with the same division (45 minute continuous anneal), and exception (2366), and again the implication is a far longer localisation length ξ_A for samples in category A.

5.2.4 Low temperature behaviour

One way to quantify the degree of disorder in a system is the product $k_\mathrm{F}l$ where k_F is the Fermi wavevector and l is the mean free path [60, 88]. In systems where the product $k_\mathrm{F}l \gg 1$, disorder and localisation are said to be weak; when $k_\mathrm{F}l \lesssim 1$ disorder and localisation are strong.

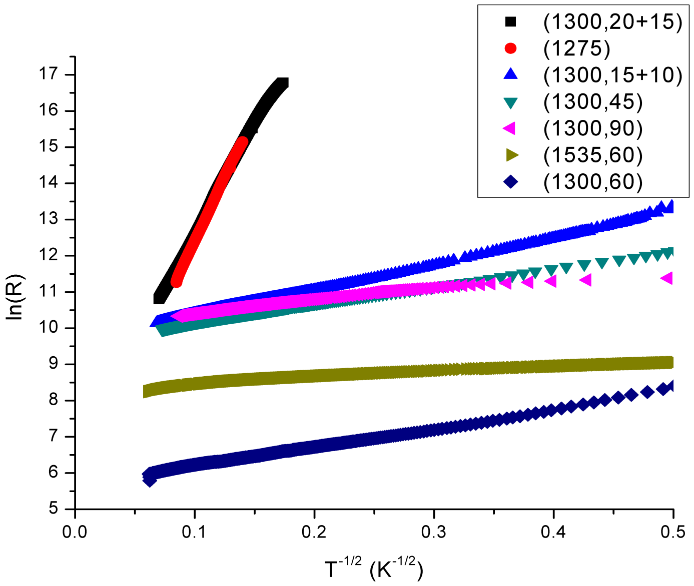

Figure 5.4: VRH Plot for Efros-Shklovskii hopping regime, for data above 5 K.

The plots for weak localisation over the full range of temperatures (figure 5.2 show that for most samples and most temperatures the agreement with this regime is poor. However, if the data below 5 K are plotted (for samples which are measurable to this temperature) the situation is not as clear cut. As the Fermi energy (hence Fermi wave vector) and also the Fermi velocity barely change with temperature, the lengthening mean free path (associated with the longer scattering lifetime) means that the product $k_F l$ changes with temperature. As the product increases away from unity, the system becomes less strongly localised, which should be visible as a closer approximation to a straight line using the axes for a WL plot; this transition to a WL regime can be identified for three samples, annealed at 1300 °C for 45, 60 and 90 minutes respectively (see figure 5.5).

5.2.5 R v T discussion and conclusions

While the epitaxial nature of the graphene is indicated by the LEED data, this technique cannot supply two important pieces of information: whether the films

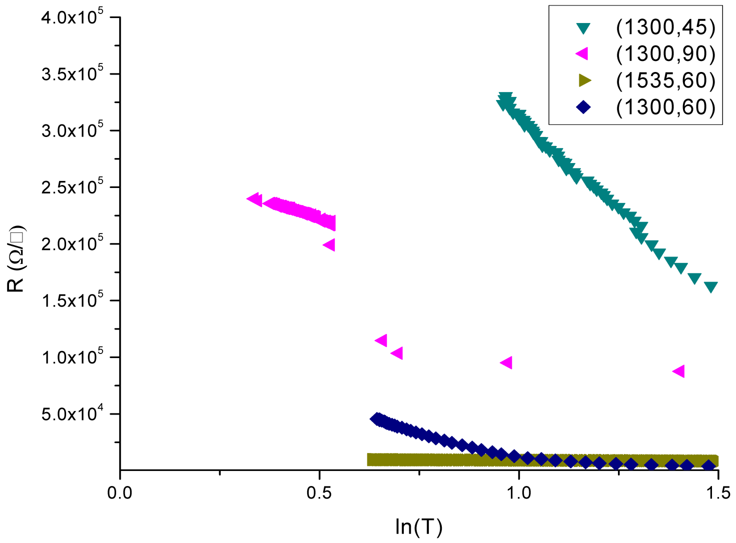

Figure 5.5: WL plot for low temperatures (below 5 K). Subset of data plotted for sample (1300,90), where thermal lag caused data artefacts, which have been removed. All samples here are in category A, as only these samples conduct down to these temperatures. The linear relationship suggests that at these temperatures, samples are approaching the WL regime.

are continuous, and for continuous films whether the long range order is sufficient for graphene-like properties to be measured. Using transport measurements, the system is probed over a larger area while giving a less forgiving view of the quality of the film, as any discontinuities have a significant effect on the behaviour of the sample, as opposed to being averaged as they are in LEED or Raman. This, combined with the motivation for studying graphene in the first place makes this a very pertinent measurement for the system studied.

The data for sheet resistivity change as a function of temperature show clear agreement to a variable range hopping regime, as opposed to weak localisation, for temperatures above 5 K. It is not possible using these data to distinguish between a Mott-VRH and an Efros-Shklovskii VRH regime (both sets give an average R-squared value of over 0.99 for the linear fits), but in either case, the data divide unambiguously into two sets of samples, distinguished by anneal duration.

Consideration of the ratio of characteristic temperatures T_{n}, and extracting ratios for localisation length ξ for the two categories of film suggests a reason for this, based on a possible growth mechanism. There are two possible ratios to consider, depending on which hopping regime is used to extract the characteristic temperature. From the Mott VRH fits, films annealed continuously for longer than 45 minutes (category A) have gradients of $\sim$5 $\mathrm{K}^{-\frac{1}{3}}$, films annealed for durations less than 45 minutes (category B) show a gradient of $\sim$50 $\mathrm{K}^{-\frac{1}{3}}$,leading to a ratio of $\xi_{\mathrm{A}}/\xi_{\mathrm{B}}$ of 10. The same data plotted for ES VRH yield values for the characteristic temperatures of $\sim$65 $\mathrm{K}^{-\frac{1}{2}}$ and $\sim$4.5 $\mathrm{K}^{-\frac{1}{2}}$ for shorter and longer than 45 minute anneals respectively, and a ratio of 180 for $\xi_{\mathrm{A}}/\xi_{\mathrm{B}}$. The single exception to this categorisation is sample (1300,15+10), which has been etched. If the impurities involved in hopping are found at true discontinuities as opposed to grain boundaries, then the ratio of length scales extracted from the plots would reflect this.

If the graphitisation process involves nucleation sites (where Si can leave the SiC structure due to defects) followed by lateral propagation of the graphitic region, then the final surface will depend on the nucleation-site density (both areal and energetic) and the propagation rate. Given that for temperatures below 1275 °C no graphitisation signature is seen for anneals of 60 minute duration, the activation energy for the nucleation appears to be just accessible at the temperatures used for these samples, and the propagation rate can be expected to be slow. The nucleation density must have a lower limit (based on the grain size of $\sim$20 nm) of 2.5×10^{15} m^{-2}. For a continuous surface to form, the temperature and duration of anneal have to be such that the nucleation density and the propagation speed allow all graphitised grains to coalesce. If the anneal is terminated prior to this, then while for measurements at high temperatures a conduction path may exist, this may no longer be the case at lower temperatures. The two distinct sets of curves A and B could therefore represent continuous and discontinuous surfaces respectively.

In this case, the length scales for coherent electron transport in the discontinuous films could be expected to be of the order of the lateral grain size (20 nm). The very similar gradient values across samples with complete films then indicates that the localisation length saturates. This is understandable, as substrates are from a single wafer, and so (prior to annealing) have equivalent inherent defect density. Finally the dimensions of the grains (∼20 nm) and the inelastic mean free path arrived at via multiplying scattering times from reference [62] ($\sim 1 \times 10^{-12}$s) and the Fermi velocity in graphene ($\mathrm{v_F} = 10^6$ ms^{-1}) mean that ratios for $\xi_\mathrm{A}/\xi_\mathrm{B}$ of 10 and 180 respectively are the correct order of magnitude. This also indicates that although film discontinuities influence the coherent transport (introducing elastic scattering centres which cause the electrons to lose their phase-coherence), electrons can traverse boundaries between grains coherently (evidence for this in high-quality graphene films is seen in [28, 89]) and that some coherent behaviour can be expected in the material being measured.

The response of the samples' resistance to an applied magnetic field will allow determination of the scattering rates for these samples, hence providing a check for the assumed scattering rate used in the above paragraph. If these scattering rates are sufficiently low, coherent electron transport (if present) will also be identifiable via MR measurements, as the electrons can be affected by a magnetic flux in ways which result in a change to the measured resistance. Finally, the two VRH regimes will give rise to identifiable and distinct contributions to any measured change in resistance with applied field. Such measurements are the obvious next step in determining the properties of the graphitised samples, and form the basis for the rest of this chapter, with the electron-electron contributions discussed in chapter 7.

5.3 Magnetotransport measurements

The behaviour of samples' sheet resistivity with temperature in a way consistent with a VRH regime indicates that the samples under discussion are not high-quality graphene. Magnetoresistance (MR) measurements were carried out as described in section 3.5.3 in order to compare samples' electronic properties in a quantifiable way. The effect of a magnetic field on electrons in high-quality graphene has been studied extensively both theoretically and experimentally. For flake graphene [7] a unique quantum Hall effect signature provides a standard for identifying single layers (see section 2.2.2). More recently high-quality epitaxial graphene has been shown to exhibit the same properties [28]. The electron transport properties of the surface layer at stages during the growth of such a layer, or for less ideal surfaces of graphene on SiC are less well-documented. An initial measurement of resistance with B-field, using a small DC bias and magnetic fields H to μ_0H = ±8T is shown in figure 5.6, and serves to introduce the dominant mechanism present for samples of this type.

The first point to note is that the resistance decreases with increasing magnetic field. Negative MR is usually associated with disorder: electrons are scattered from defects, and the effects of a magnetic field on backscattered electrons results in MR similar to that seen in figure 5.6 (see section 2.3.2).

The dependence on both temperature and bias of both zero and non-zero field resistance means that a relative change in resistance is required in order to compare measurements across samples and conditions. The definition of magnetoresistance used is

$$MR = \frac{R(B) - R(0)}{R(0)}. \tag{5.4}$$

In some literature this is quoted as a percentage. Because some theory fits to quantities other than MR, graphs where data is fitted may use other measures of relative change, such as magnetoconductance, $MC = (G(B) - G(0))/G(0)$, or $\delta\rho/\rho^2$. All unfitted data is presented as magnetoresistance percentage unless otherwise specified.

Data can be fitted using the theory of conduction in disordered materials, such as weak localisation. These consider various scattering mechanisms, and the fitting parameters are scattering lifetimes (τ_n), rates (τ_n^{-1}), or characteristic magnetic fields (B_n) associated with these. The theoretical background is based

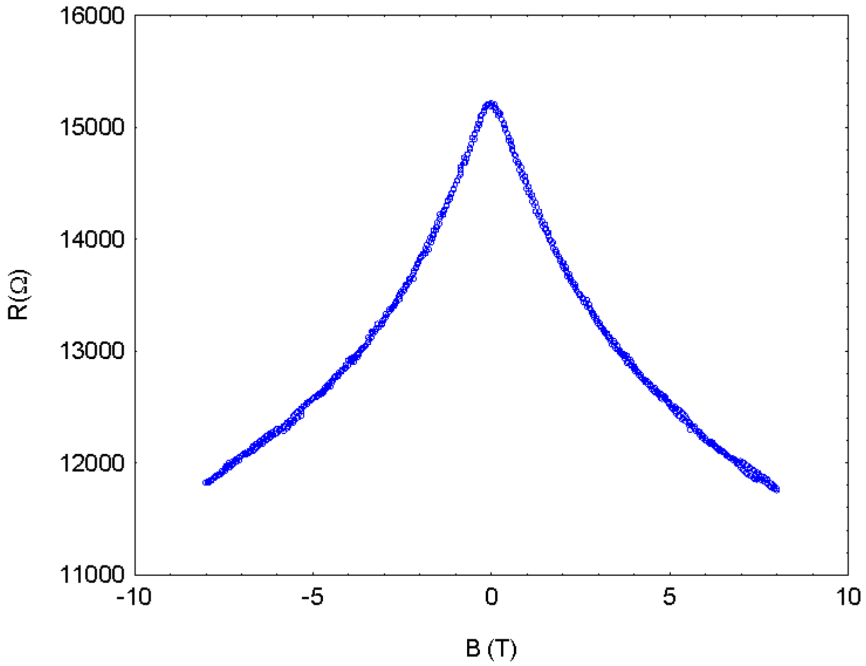

Figure 5.6: Measured resistance with an applied magnetic field. Sample (1300,90) at a temperature 1.5K, measurement bias 300 nA DC.

in WL regimes (*i.e.* $k_{\mathrm{F}}l \gg 1$) however various work [90, 91] shows that equation 3.1a is valid for negative MR even if $k_{\mathrm{F}}l \sim 1$, as is the case with the samples discussed in this chapter (based on the R(T) data above 5K). The equations described here are not specific to graphene, in contrast to some introduced in chapter 2, and which will be used in chapter 6.

Figure 5.7 shows fits to the same data using two expressions introduced in chapter 3. Both expressions fit the data closely, and with knowledge of the diffusion constant would yield the characteristic times for each scattering mechanism. Without a means to determine the diffusion constant D (such as by gating the sample and thus controlling / determining k_{F}), equation 3.2a is more appropriate. A single fit leaving D as a free parameter in a fit to equation 3.3a yields a value for the scattering time τ_ϕ of 1.29×10^{-12} s and for D of 2.4×10^{-4} m^{2}s^{-1}; the value found by converting the B_2 value is 1.89×10^{-12} s. This serves to justify the assumption for τ_ϕ used in section 5.2.5, and also to show the close equivalence of the two methods. The measurements made in this study do not yield D (the value from the fit is lower than for studies on less disordered material such as 0.3 m^2s^{-1}[92] or 8×10^{-3} m^2s^{-1}[93]), and for this reason fits for the remainder of the chapter will use the characteristic fields B_n, which will be sufficient for plotting trends with temperature, or comparisons between samples.

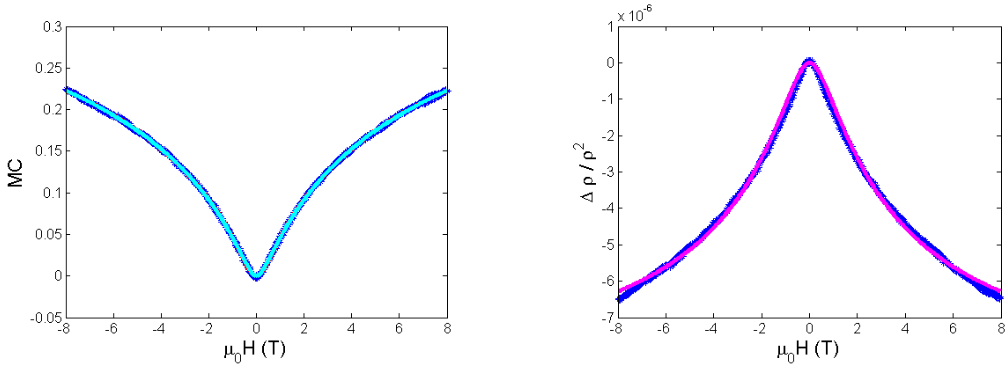

(a) (b)

Figure 5.7: Fits to equation 3.2 (a) and equation 3.3 (b) for data measured on sample (1300,90) at 1.5 K.

5.3.1 MR trends with temperature

The MR observed in all samples is temperature dependent. The cause of this temperature-dependence is that while scattering lifetimes for elastic, spin-orbit and magnetic scattering are independent of temperature, the phase coherence depends on temperature as coherence is broken via inelastic collisions, mediated by phonons which in turn have a temperature dependence.

Figure 5.8a shows MR data from a sample with a large number of layers of graphitic material on the surface. MR data taken at various temperatures shows two trends with decreasing temperature: the magnitude of the negative MR increases, and the shape of the curves becomes increasingly sub-linear. For a sample with only a few layers of graphitic material, there is a difference in the shape of the curves, but the same overall trend with temperature (figure 5.8b). This can

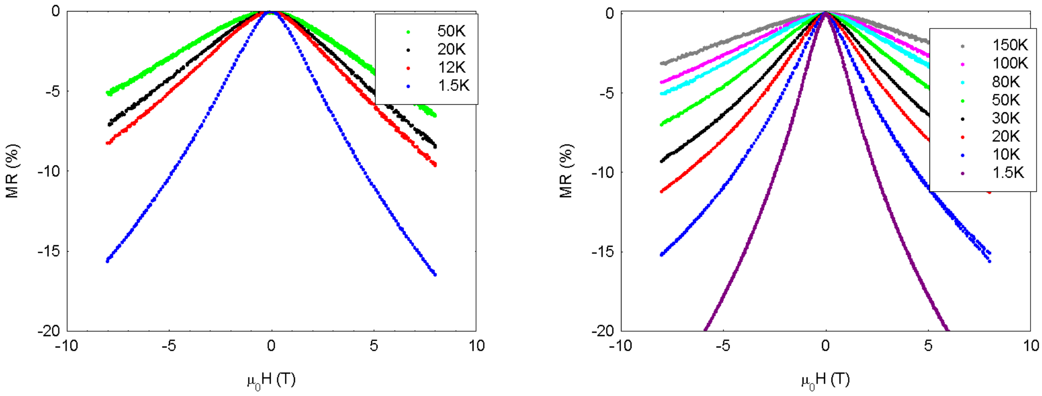

(a)

(b)

Figure 5.8: MR curves taken at various temperatures for sample (1535,60) (a) and sample (1300,60) (b). All measurements are taken at a DC bias of 300 nA.

be quantified in terms of the parameters used to fit the data; in equation 3.2 the characteristic field B_2 is proportional to the inelastic scattering rate (τ_{i}^{-1} or τ_{ϕ}^{-1}). The parameter B_2 is shown for both sets of curves plus a third sample in figure 5.9, and in each case is approximately linear when plotted against sample temperature, in agreement with other work [62, 94]. Without knowledge of the diffusion constant, the value of the scattering time is not known from this fit, however the values for B_2 are lower for the samples annealed at a lower temperature and for shorter durations, indicating a lower scattering rate. It is worth mentioning that in general graphitised samples are slightly 'smoky' in appearance, as expected from the attenuation seen in the Raman signal from the substrate (section 4.3.1), and that the (over-annealed) sample measured here was almost opaque, indicating many layers of graphitic material: it is included solely for comparison with the other samples which are more graphene-like.

5.3.2 MR behaviour with applied bias

Not only the temperature, but the bias used to measure the samples' sheet resistance can change the shape of the magnetoresistance curve (due to both $R(0)$ and ΔR changing), and hence the parameters used to fit the data. In figure 5.10,

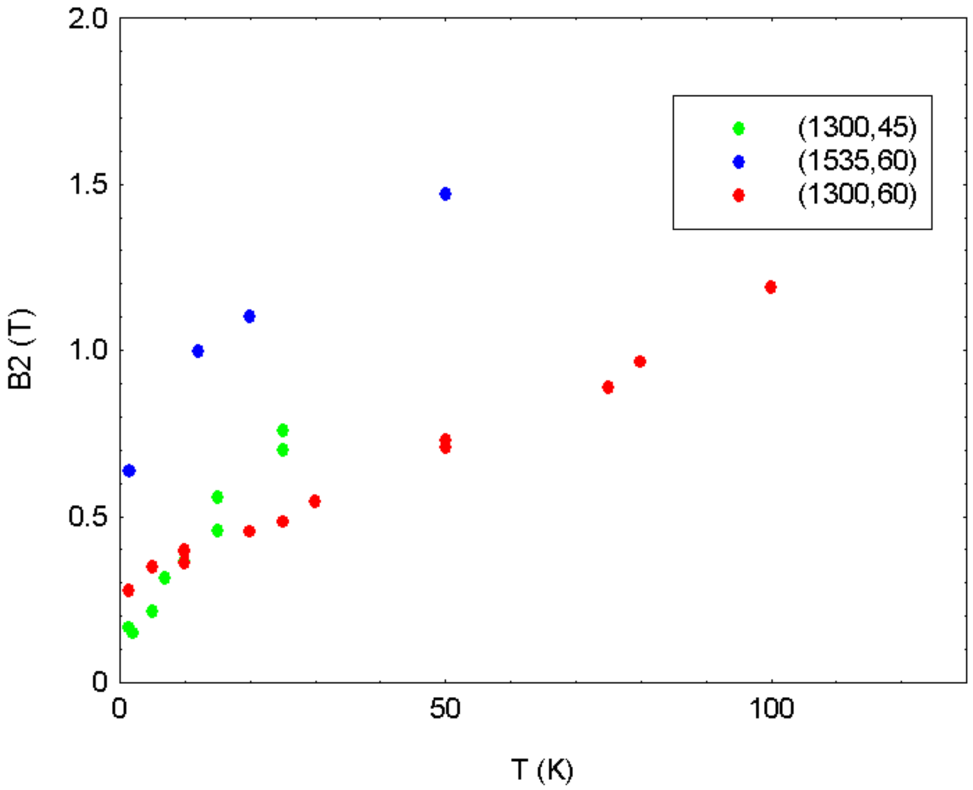

Figure 5.9: Fit parameter B_2 for fits to MR curves at various temperatures using equation 3.2a. The parameter B_2 is proportional to the inelastic scattering rate, and increases linearly with temperature.

the two plots both show a general trend towards larger measured MR with lower bias which can be quantified through fit the parameter $\eta(T)$ in equation 3.2. This trend with bias is shown in figure 5.11, and can be understood in terms of the coherent scattering diminishing at higher biases.

Careful consideration of bias is important in terms of the power dissipated, which was less than 5 nW in order to preclude heating effects. Also, in some samples, definite features can be seen at lower bias which are lost for a bias greater than $\sim$1 μA; the bias dependence of additional features is in agreement with the trend towards larger WL at lower bias due to greater coherence. These features can be seen more clearly if the data are fitted to a localisation expression 3.2,

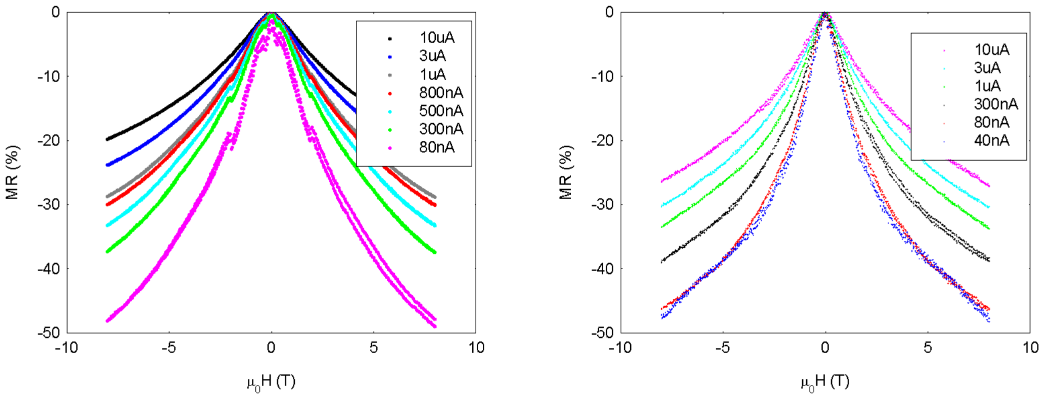

(a) (b)

Figure 5.10: MR curves for (a) (1300,60) and (b) (1300,45) measured at various bias. All measurements taken at 1.5K.

and the fit is then subtracted. Figure 5.12 shows the result of this procedure for three samples. The features in the data for sample (1300,60) at ∼2 T, which are just visible in the measured data in figure 5.10a, can be discerned more clearly following this process. The subtraction shows other features which appear to be one, oscillatory, component with similar features for samples (1300,60) and (1300,45). Sample (1535,60) is included as a control for artefects and shows a possible very low level of oscillation; this, and the fact that these subtle features are not seen in all samples or at higher temperatures supports the conclusion that they are real. The features are not fully understood, but it is worth noting that at a magnetic field of μ_0H=2 T the magnetic length, $\eta = \sqrt{\hbar/eB}$ is of the order of 20 nm, similar to the grain size.

The extraction of features via the subtraction procedure shows that this approach has value over and above being used to check goodness of fit, and motivates its further use in attempting to identify other influences on the conduction electrons. The coherence seen (the presence of which agrees with the mean free path estimated from the RvT data) can be explained by electrons scattering elastically over grain boundaries or by the greatest contribution to the conductivity coming from a buried layer(s) which are more ordered than the surfaces seen using surface

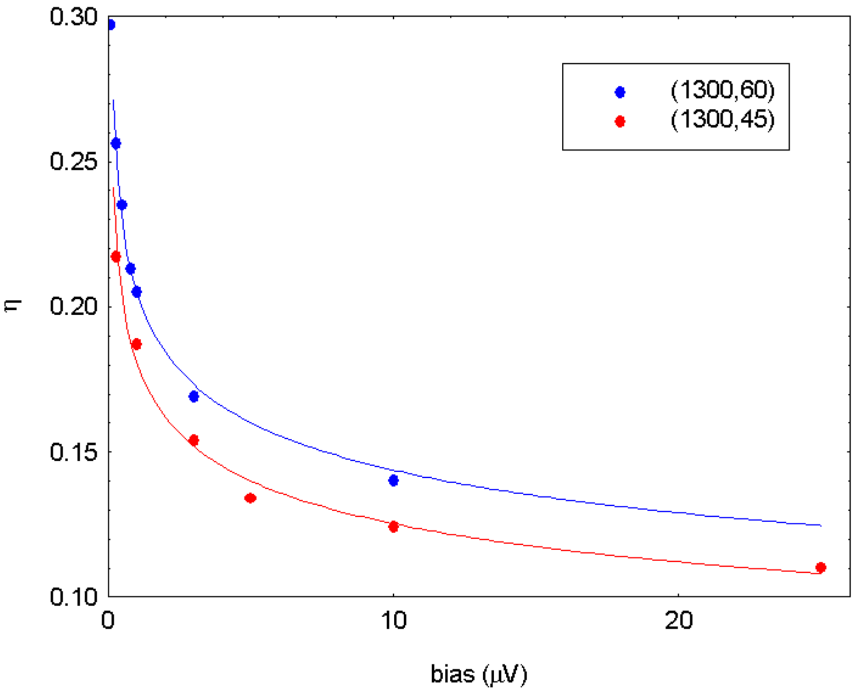

Figure 5.11: Trend with DC bias of η parameter from equation 3.2. Lines are guides for the eye.

science techniques in chapter 4.

Ascribing a definite mechanism for the oscillatory features seen in figure 5.12 is challenging. The features appear to be periodic in B, rather than the B^{-1} periodicity which would be expected if the mechanism was Shubnikov de Haas oscillations (subtraction of the WL signal could, however mask low-field features). This periodicity in B would possibly indicate Sondheimer oscillations (due to electrons being scattered from the surface interfaces) [95], but these should decrease in amplitude for higher values of B; this is not the case for sample (1300,45), and the similarity between the two traces indicates a common mechanism. Oscillations due to electrons trapped in classical orbits which are commensurate with material defects have been observed in artificial defect arrays in 2DEG materials [96] and also more recently in graphene [97]. These oscillations appear similar to those seen in the samples presented here, and the similarity between the two

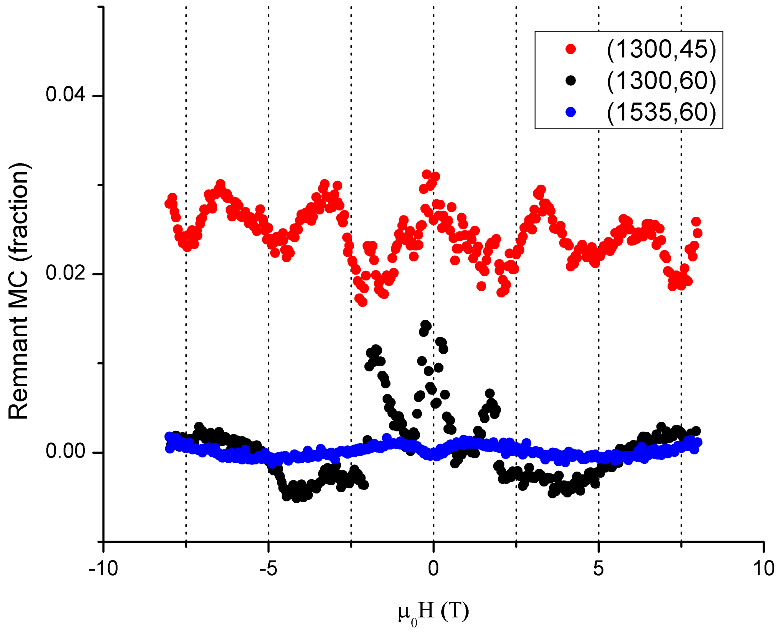

Figure 5.12: Sample (1300,60) (300 nA DC), (1300,45) (10 nA AC) and (1535,60) (300 nA DC) with WL fit subtracted from data. Data for (1300,45) is offset for clarity.

sets of data is then attributable to the similar size of the domains in the granular graphene; against this attribution is the fact that deviations from a single spatial periodicity would cause any oscillatory component in B to have many component frequencies, which would tend to destroy any single periodicity in the magnetoconductance. Finally universal conductance fluctuations (UCFs) are often invoked to explain mesoscopic magnetoconductance oscillations, in 2DEG materials in general [98] and graphene specifically [99]. While in high quality material and 2DEG materials the period in B is usually very small, the period depends on the phase coherence length l_ϕ as $l_\phi \sim \Phi_0/\Delta B$ where Φ_0 is the flux quantum [100, 101], which would make the observed period possible; in the case of the oscillations seen in graphene, there was an appreciable dependence on bias current, in agreement with the observations here. The argument against UCFs is that they are generally understood as being a fingerprint of a specific device (the universality being only in terms of magnitude), and the two traces are if anything too similar to conform to this. It is also possible that a combination of these candidate mechanisms is present, further complicating the process of positively identifying them. Measurements using equipment which can reach lower temperatures and higher magnetic fields would serve to identify the mechanisms more clearly.

5.3.3 MR comparison between samples

Figure 5.13 shows the MR behaviour of several samples at the same bias and temperature. The shape of the curves (unquantified) shows a trend with annealing time. The one exception is the data for 2366, which has a shaped mesa, defined via etching with oxygen plasma, and which was an exception to the categories in section 5.2.5. The trend with this exception removed is that the curves show larger negative magnetoresistance and are narrower for shorter anneals (while all having an anneal long enough to produce an apparently continuous film). This indication of greater coherence is in agreement with the appearance of oscillatory features for the samples annealed for shorter durations.

5.4 Bias and field dependence combined

5.4.1 Dynamic conductance

Knowing that the MR of the samples depends on the bias used, the characteristics of zero-field conductance could be expected to yield further information. To this end, the conductance was measured as a function of bias voltage. The results for a measurement with no applied field can be interpreted for samples with localised states as described in reference [102]. The conductance change with bias is given by

$$\sigma = \sigma_0 \exp\left[-\left(\frac{\mathcal{E}_0}{\mathcal{E}}\right)^{1/2}\right],$$

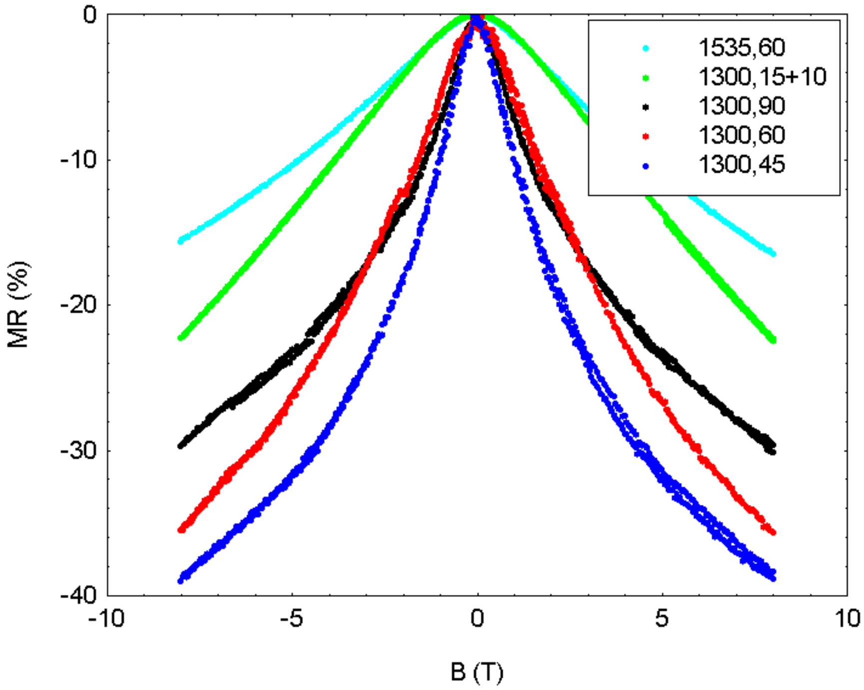

Figure 5.13: MR measurements at 1.5 K for samples annealed at 1300 °Cfor various durations. Sample (1535,60) is included for comparison. Measurements were made with a DC bias of 300 nA.

where

$$\mathcal{E}_0 = 4e/(\kappa\xi^2). \tag{5.5}$$

Here $\mathcal{E}$ is the electric field, $\mathcal{E}_0$ is a characteristic electric field, κ is the dielectric constant and ξ is the localisation length.

This can be used as the basis for a plot as in figure 5.14 in order to extract a value for $\mathcal{E}_0$ and localisation length ξ. When considering the figure, the fit to this regime appears close (at high fields). The value for the dielectric constant κ may vary slightly from the sample in reference [102] (as the level of disorder in the samples in that paper influenced this value). Comparing the published values for $\mathcal{E}_0$ with those obtained for the disordered graphene layers yields localisation lengths of approximately 60 nm, (assuming the same value for κ). This value, along with the coherence time from WL fits to MR data provide important additional support for the conclusion reached for the ratio of localisation lengths arrived at using RvT data.

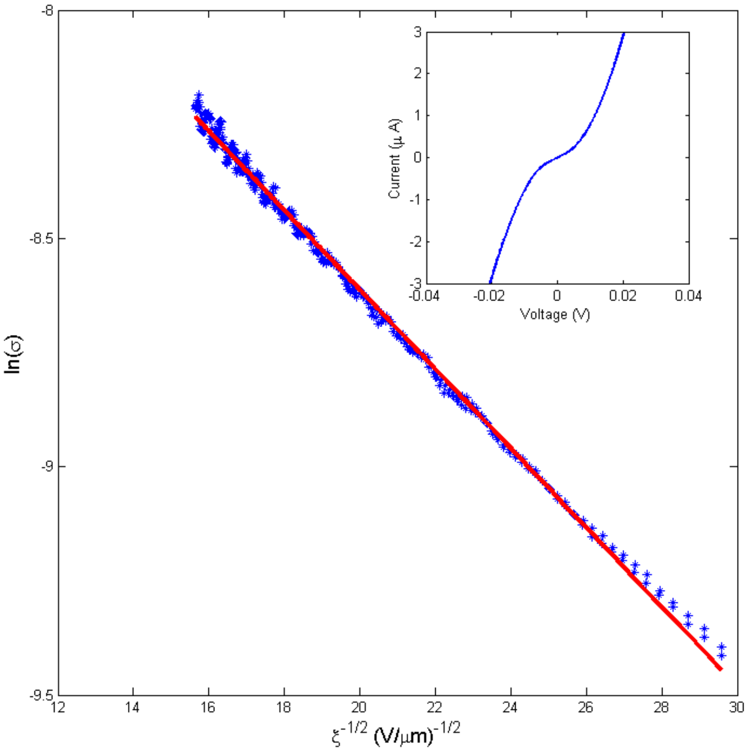

Figure 5.14: Sample (1300,60). Dynamic conductance measurement made at 1.4 K. Plotted to extract a value for the characteristic electric field, ξ_0.

5.4.2 Dynamic conductance and magnetic field

The bias- and magnetic field- dependence of the samples' resistance are summarised conveniently by plotting a surface with the x and y axes being bias and field, respectively. These surfaces are the results of measurements made by taking a dynamic conductance curve at each magnetic field. In all cases presented here the resistance behaviour is monotonic in both magnetic field and bias voltage, with no sign on these surface plots of oscillatory behaviour as seen when the fitting and subtraction processes are used for MR sweeps at a single bias.

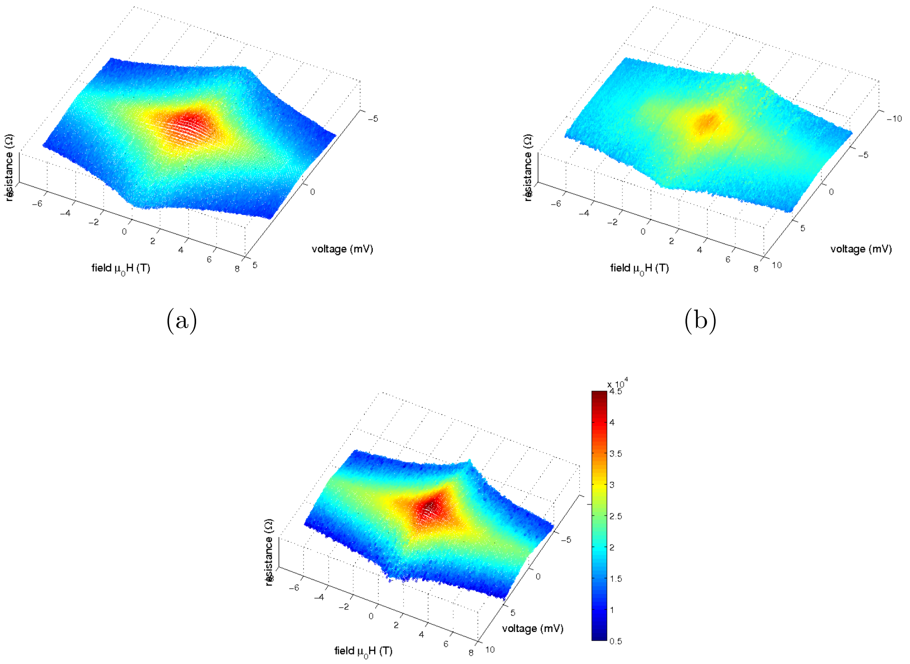

(a)

(b)

(c)

Figure 5.15: Dynamic conductance with Field. Samples (1300,60) (a), (1300,90) (b) and (1300,45) (c). The colour scale is common for all plots, and runs from 5 kΩ to 45 kΩ.

The surfaces plotted here show the relatively strong dependence of resistance on source-drain bias compared to magnetic field. The fact that, from a zero B-field low bias maximum resistance, a magnetic flux of 8 T is required to decrease the resistance to the same level as is achieved by only a 5 mV bias is an indication of the non-linear nature of the $I(V)$ seen in figure 5.14.

5.5 Conclusions

Transport measurements provide a means of distinguishing samples which appear similar when surface techniques are used. They also enable additional effects to be observed.

The transport characteristics of samples can be identified by the change in resistance with decreasing temperature. Samples fall into two categories based on anneal duration which are identified as being incomplete (or below percolation transition) and complete films (or above percolation transition) respectively.

All samples show disorder-related localisation behaviour. When measured in applied magnetic fields H of $\mu_0 = 8$ T this is the dominant feature. These MR curves can be fitted and parameters extracted which are indicative of the scattering rates.

The temperature dependence of scattering rates follows expected behaviour for a weak localisation model, and extracted scattering times agree with literature. The scattering rates also agree with the explanation of the ratio of localisation lengths for the continuous and discontinuous films.

Lower bias measurements for some samples (annealed for shorter durations) yield features which are small relative to the WL signal, but which can be seen clearly if the dominant WL is fitted and subtracted. It is not possible for these samples to distinguish between several possible causes of these features without further measurements using equipment which can reach higher fields and lower temperatures.

Chapter 6

Transport properties of samples from accelerated growth

6.1 Introduction

Samples discussed in this chapter were prepared as in section 3.2.3. Based on the conclusions reached in chapters 4 and 5 about the likely process of graphitic area propagation (namely that the speed of propagation at 1300 °C is very slow), the annealing conditions were reconsidered. Instead of using a single temperature close to the activation temperature and investigating the effects of anneal duration on the onset and propagation of graphitisation, the rate of propagation was increased by raising the annealing temperature. For this procedure, a sapphire cap was used to protect samples from any debris from the sample plate or the heating assembly. An initial anneal for sample (1300,60,1400,30) (1300 °C for 60 minutes) did not result in graphitisation (see section 4.2) and the choice of an anneal temperature of 1400 °C was informed by this. As described in section 4.4, comparison of AFM micrographs shows that this was successful in producing a surface consisting of larger individual domains of graphene, indicating that the propagation rate increases faster with temperature than does the density of possible nucleation sites. Lithographic patterning was used to form contacts as with the samples discussed in chapter 5, and equivalent measurements were made. Samples discussed in this chapter are therefore a small subset of those characterised in chapter 4.

Table 6.1: Summary of conditions for higher temperature annealing.

Sample number	Temperature	Duration	Label
2438	1300 °C	60 min	
followed by	1400 °C	60 min	1300,60,1400,60
2440	1400 °C	30 min	1400,30

6.2 Temperature-dependence of film resistance

Resistance was measured with a DC 4-point technique while cooling the samples in a constant-flow He cryostat. The data show that the resistance change is far less pronounced than with the samples discussed in chapter 5. As with those samples, plots of variable range hopping and weak localisation serve to identify which transport regime the samples are in. Figure 6.1 shows plots as introduced previously in section 5.2; the fit to a 2D VRH plot is poorer than for the non-optimised samples, whereas the weak localisation plot (figure 6.1b) shows a good agreement up to high temperatures (∼100 K). This is immediately in contrast to the previous chapter where a good fit to a WL regime was only possible below 5 K, and is indicative of far larger coherent contribution to transport in the samples, which should be quantifiable as longer coherence lengths and times. Samples measured in reference [6] also exhibited R(T) behaviour in agreement with weak localisation, up to temperatures of 40 K.

This gives an indication also that the product $k_\mathrm{F} l$ is greater than 1, and also greater than for the samples discussed in chapter 5. Given that any doping by the substrate or residues from the lithographic processing is likely to be the same or similar for all samples and that in any case the doping of the lowest layer is a consequence of the substrate interaction [62], k_F should also be similar, meaning that an initial tentative conclusion is that these samples have a longer l (elastic mean free path) compared to the previous samples. Quantifying the various scattering lengths and times is not possible without knowledge of k_F from a gated device, defined Hall effect device, or from Shubnikov de Haas oscillations, but

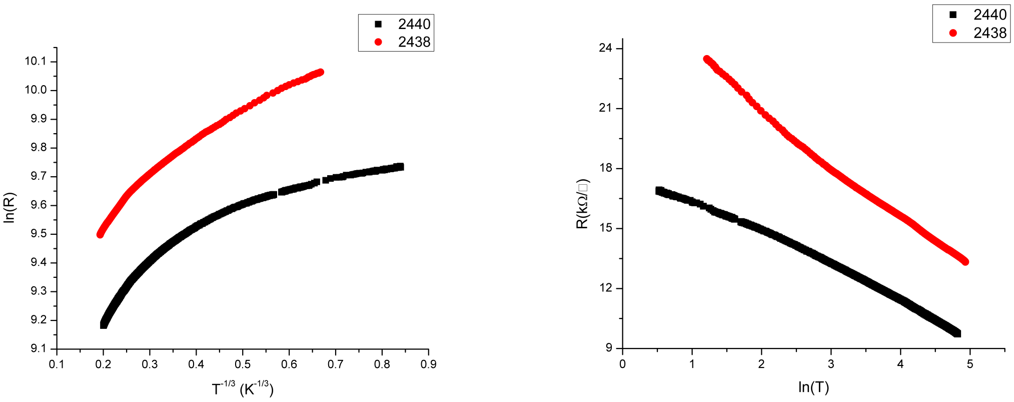

(a) (b)

Figure 6.1: RvT plots for VRH and WL. The WL plot yields a more linear relationship to high temperatures, indicating that samples in this chapter have significantly larger coherence lengths than those in chapter 5.

a value of k_F of 10^{-8} m^{-1} is commonly found in the literature [92]; samples in the previous chapter would then have l of order 10nm, similar size to the grains, and this value would be higher for samples discussed in this chapter, in agreement with the AFM data. This should be reflected in values for characteristic scattering field B_ϕ, which is proportional to scattering rate and which is obtained from magnetoresistance measurements equivalent to those described in chapter 5 .

6.3 Magnetotransport measurements

Magnetotransport measurements enable the degree of localisation to be quantified, with scattering rates calculated via fits to data. To this end samples were measured in an applied magnetic field H of μ_0 H $= \pm 8$ T, at temperatures between RT and 1.3 K. Magnetic fields were swept from positive to negative and back to positive. All measurements are 4-point, current-flipped and use a DC bias of 300 nA (as described in section 3.5) unless specified.

6.3.1 Overview of MR features

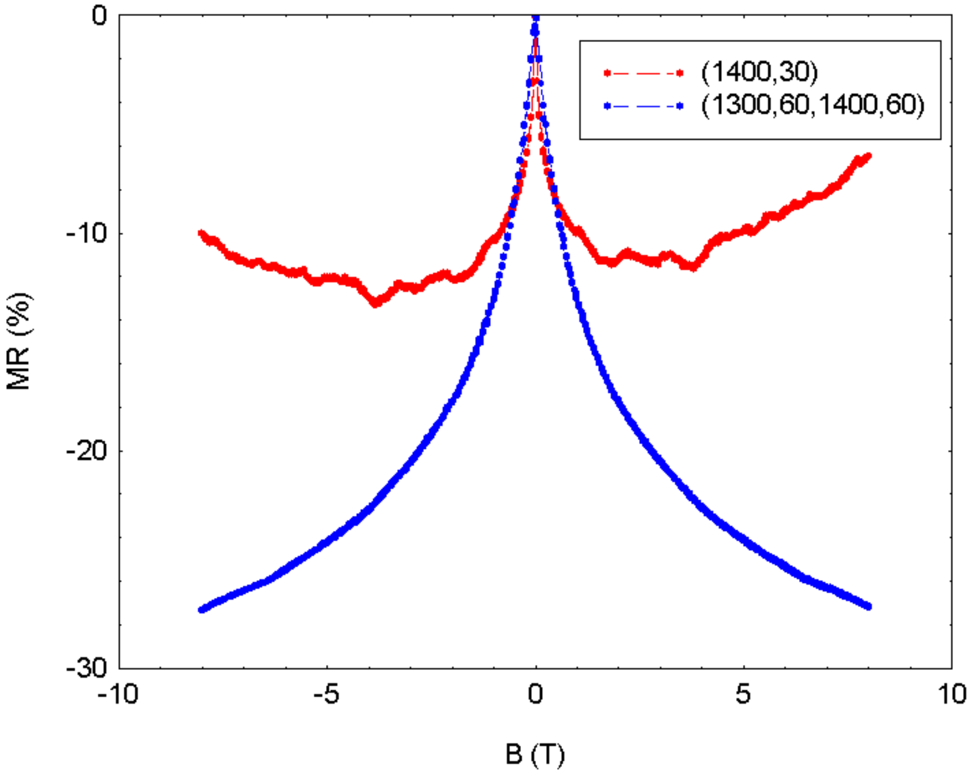

Figure 6.2: MR plots for (1300,60,1400,30) and (1400,30), measured at 1.5 K.

Figure 6.2 shows 8 T measurements as described, with MR again being defined as $(R(B)-R(0))/R(0)$, plotted as a percentage value. For both samples the MR peak is sharper than for samples in chapter 5, indicating greater coherence. However, the most significant difference is that the MR does not remain negative for sample 2440. Inelastic (dephasing) scattering rates are now lower than the rate of intervalley scattering [62]. This sample appears similar to 2438 in terms of lateral grain size (from AFM), so the greater extent to which transport is coherent is attributed either to fewer layers or diminished substrate interaction. A shorter-duration anneal is likely to have resulted in fewer layers, which suggests that additional layers(s) are the cause of the decreased coherence, but the difference in attenuation is beyond the resolution of the Raman technique used (see section 4.3). This departure from the graph shapes seen in chapter 5 introduces the need for alternative methods to explain and extract parameters from these curves, as localisation fits to ±8 T are clearly not going to be sufficient.

Another significant departure from any MR data presented so far is that (for sample 2440) whereas previously subtractions were required to show additional (oscillatory) features, some are visible here in the measured data. While providing some support for the remnant shapes seen in chapter 5, this aspect of the MR curves also serves as motivation for further, similar subtractions in order to characterise samples more fully, especially for sample (1300,60,1400,30), which could be expected to show some coherent contribution, based on the results in section 5.3.2 and the sharpness of the WL peak in figure 6.2.

Finally, the improved quality of the material means that the fitting procedures should be revisited, as the decreased disorder may mean that scattering times are long enough to make intra- and intervalley scattering relevant, as mentioned in section 2.3.2.

6.3.2 Fitting equations

As before, the WL features can be fit using expressions from [60] (equation 3.2a), or from [62] (equation 3.3a is a standard WL expression from this paper). In the same paper, the appropriate equation, containing terms specifically for graphene, is given below as 6.1a.

$$\begin{aligned}\Delta\rho(B) = -\frac{e^2\rho^2}{\pi h}\Bigg[& F\left(\frac{2\tau_\phi}{\tau_\mathrm{B}}\right) - F\left(\frac{2}{\tau_\mathrm{B}(\tau_\phi^{-1} + 2\tau_\mathrm{iv}^{-1})}\right) \\ & -2F\left(\frac{2}{\tau_\mathrm{B}(\tau_\phi^{-1} + \tau_\mathrm{iv}^{-1} + \tau_\mathrm{w}^{-1})}\right)\Bigg]\end{aligned} \tag{6.1a}$$

where

$$F(z) = \ln(z) + \Psi\left(\frac{1}{2} + \frac{1}{z}\right) \tag{6.1b}$$

and the various scattering times and rates are the inelastic or phase-coherent time τ_ϕ, the intervalley scattering time τ_{iv}, and the warping induced relaxation time τ_w. The τ_B is related to the applied field via the diffusion constant D by $\tau_B = \hbar/2eDB$.

The lack of knowledge of the diffusion constant D means that a more direct way to fit the data is via an expression from [32], which is the original paper on the theory of the response of conductance in graphene to a magnetic field.

$$\frac{\Delta\rho(B)}{\rho^2} = -\frac{e^2}{\pi h}\left[F\left(\frac{B}{B_\phi}\right) - F\left(\frac{B}{B_\phi + 2B_\mathrm{i}}\right) - 2F\left(\frac{B}{B_\phi + B_*}\right)\right], \tag{6.2a}$$

where

$$F(z) = \ln(z) + \Psi\left(\frac{1}{2} + \frac{1}{z}\right), B_{\phi,i,*} = \frac{\hbar c}{4De}\tau_{\phi,\mathrm{i},*}. \tag{6.2b}$$

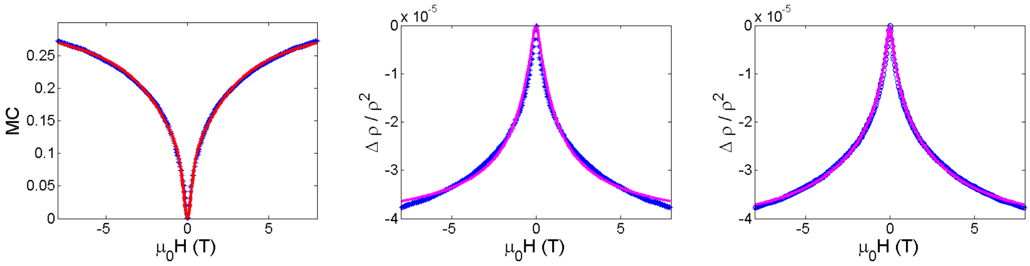

(a) (b) (c)

Figure 6.3: MR plots for (1300,60,1400,30) measured at 1.5 K, fitted using equation 3.2a (a), equation 3.3a (b) and equation 6.2a (c).

Figure 6.3 shows data for sample (1300,60,1400,30), fitted using equation 3.2a as for data in chapter 5 and also using equations 3.3a (a fit to standard WL) and 6.2a (including terms for WAL). For this sample, which retains the negative MR characteristics of the more disordered samples while exhibiting a far sharper MR peak, it is unclear whether the graphene-like fit would be expected to describe the data better. From the fits, it can be seen that the least good is the fit to standard WL fit 6.3b, which is an indication that the full expression may be required for this sample. The discrepancy between how closely this expression and equation 3.2a fit the data is due to the fact that equation 3.2a effectively has an additional fitting term contained within the $\eta(T)$ term (as introduced in section 3.6); support for this comes from the fact that if expression 3.3a is amended to include a scaling factor, the fit is much closer (and a scaling factor of 0.2 is found, in good agreement with [62]). Finally, the full expression, including the terms for weak antilocalisation, fits closely without the need for a scaling factor; this is in contrast to the situation for the samples for discussed in chapter 5. This informs the choice of fitting equation for the remainder of this chapter, as even with no visible (*i.e.* positive MR) contribution from WAL terms, the full expression is required in order to avoid the need for a scaling factor.

6.3.3 Weak localisation: trends with temperature

MR curves for sample (1300,60,1400,30) were taken at various temperatures. The behaviour is similar to that seen in chapter 5, with sharper peaks and more sub-linear curves at lower temperatures. These curves can be fitted using equation 6.2a; figure 6.4 shows the trend of B_ϕ with temperature for fits to this data, and for comparison also the data presented in chapter 5 are also plotted. The trend for B_ϕ is linear for sample (1300,60,1400,30), whereas two samples in chapter 5 show a trend, but not one which would be expected, indicating that the equation is not relevant for their magnetoconductance characteristics (this can be explained as the dominant scattering mechanism being inelastic scattering, in which all phase coherence is lost). Interestingly, the over-annealed sample shows a linear trend with temperature (although for all three samples the other scattering terms hit the limits imposed by the fitting procedure for the linear sections of their traces). The magnitude of the parameter B_ϕ (which is proportional to the scattering rate) is smaller than for the fits in chapter 5 (both as fitted here, and as presented in chapter 5); based on the values from chapter 5 they are smaller by a factor of 10.

Values for the parameter B_ϕ are also plotted for sample (1400,30), based on fits to the measured MR data. While this serves for an initial comparison, it appears that the scattering rates are similar to sample (1300,60,1400,30), which

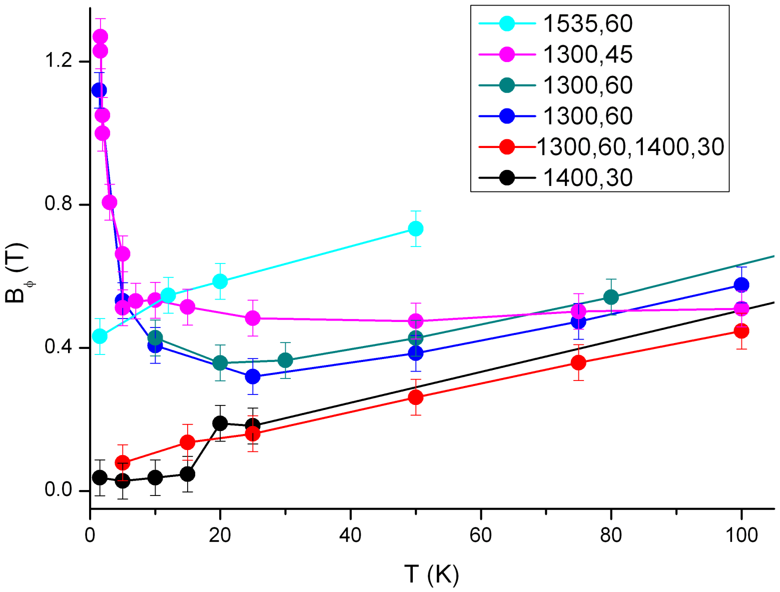

Figure 6.4: Values for B_ϕ obtained by fitting MR data to equation 6.2a. Error bars are assigned based on two sets of data for sample (1300,60) which were taken 3 months apart. Sample (1400,30) has a point at 150 K, not shown.

is not expected based on the shape of the MR data in figure 6.2. The data requires additional steps in order to be analysed properly; this procedure is detailed in the following section.

6.3.4 Data analysis for more complex MR

In the case of sample (1400,30), there are several contributing features contained in the magnetoresistance. These are depicted in figure 6.5, and can be summarised as

- With increasing temperature, zero-field resistance decreases, and magnitude of WL peak decreases, almost vanishing at 150 K
- All curves have a positive component at high fields which appears to become more pronounced at low temperature, but which persists to high temperatures.

- Additional features appear at temperatures below ∼10 K

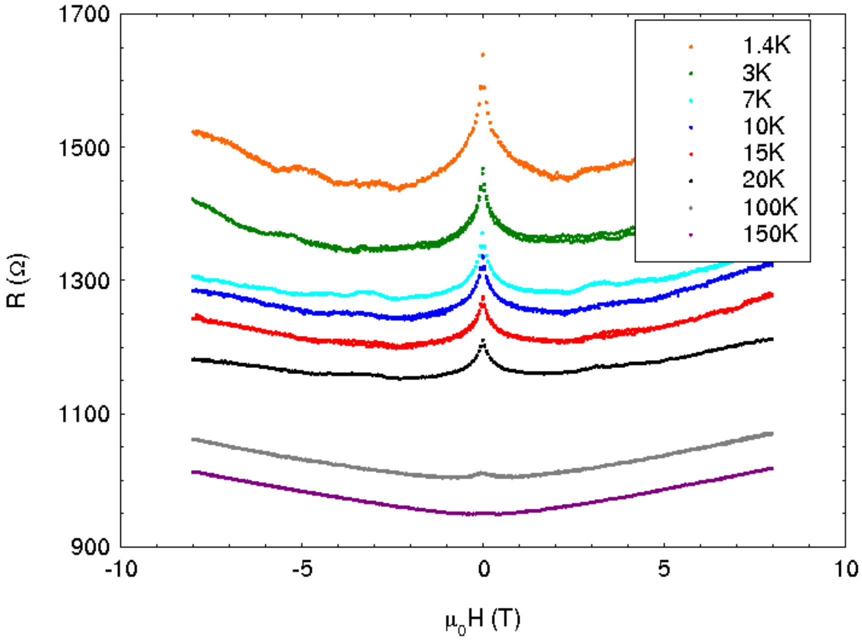

Figure 6.5: MR Data, 300 nA bias, various temperatures. Sample (1400,30). At higher temperatures the WL peak becomes smaller and the oscillatory features are no longer present. A positive component remains at temperatures of 150 K.

This brief summary is consistent with observations in the literature for epitaxial graphene [62] and also for graphene produced via the exfoliation method [103]. For measurements made on graphene where the lateral size of single domains exceeds that of the device area, the low-temperature features have been shown to be due to Landau-level quantisation (Shubnikov- de Haas oscillations). The oscillations in the raw data seen in figure 6.2 require further investigation, as the similarity between this data and that published in [97] is particularly striking. As the oscillations were interpreted as originating from introduced disorder, analysis of data presented here could add to an understanding of conduction in these samples with smaller grains.

Clearly in the case of this sample the physics required to explain at least some of these features is specific to graphene, as opposed to the more general low-dimensional physics utilised in chapter 5 (this was indicated in the details for the fit to negative MR in the previous sections, but is more explicit for this sample). The positive gradient at high applied fields is attributed to two individual components: a classical Lorentz force on the electrons (which persists to high temperatures) and a positive component from weak antilocalisation, which is present only at lower temperatures [62] (the temperature at which this component is no longer relevant is governed by the same relationship which makes the WAL equation irrelevant for the disordered samples: the inelastic scattering rate increases with temperature until it is the dominant mechanism). This introduces an additional step when fitting MR data, as the classical contribution must be subtracted, achieved by subtracting a data set taken at high temperature. The fit to equation 6.2a is then based on the corrected resistance, defined as $R^*(B,T) = R(B,T) - R(B, 150\text{ K})$ where the data at 150 K is chosen due to the fact that at this temperature the WL peak is not present. The full description of the fitting procedure can be summarised as follows

- Initially, data from a high-temperature MR sweep (150 K in the following discussion) is subtracted from the low-temperature MR curves being analysed. This removes the positive background due to classical effects.
- A small Hall-effect contribution can sometimes be seen due to the alignment of the electrodes. This is removed by subtracting a linear fit from the data.
- The next correction to the data is to convert from resistance to resistivity. As the measurements are of sheet films 5 mm × 10 mm, and the contacts are separated by ∼20 μm the correction factor used is 4.5325 [104].
- The details of the contacts used for measurements can also differ from sample to sample, even if the lithographic pattern used is the same, due to the success with which the sample is mounted onto the chip carrier. To enable full comparison between samples, the resistance is quoted in units of $\Omega/\square$.
- The remnant resistivity is then fitted using equation 6.2a.

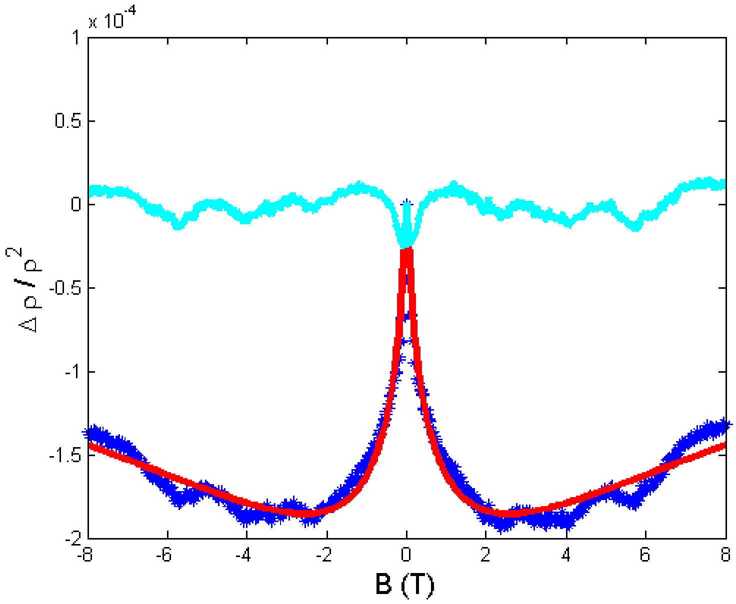

Figure 6.6: WAL fit to low-temperature data (1.5 K) with high-temperature background subtracted. Data is dark blue, fit red and remnant (data minus fit) is pale blue.

The resulting fit (for 1.5 K data) is shown in fig 6.6. The modification to the fit procedure modifies the characteristic field B_ϕ to lower values than in figure 6.4, as expected based on the initial shape of the MR curve. The difference between the fit and the data is also plotted - this shows features which are symmetric in field, and which do not appear for high temperatures. The oscillatory features obtained by fitting and subtracting (using both fitting methods) are passingly similar to those seen in chapter 5, and are considered in more detail in section 6.3.6.

6.3.5 Weak localisation: subtraction of fits

Despite the increased coherence in the samples presented in this chapter, and the associated alteration to the physical models used to describe some aspects of their behaviour, the remnant magnetoresistance bears a striking resemblance to that seen for previous samples. As sample (1400,30) has visible oscillations in MR prior to any data manipulation, and as the coherence times for sample

(1300,60,1400,30) are longer than for samples for which oscillations have been seen in chapter 5, similar analysis for this sample is expected to yield an oscillatory component despite the amplitude being too small to discern in the measured trace. In order for the fitting to be consistent, the method for this sample should be a single-stage subtraction, as in chapter 5, but with the fitting to data carried out using equation 6.2a; on performing this operation on the data, the largest contribution to the remnant trace is due to poor agreement with the fit, which is found to be large relative to the amplitude of the (now visible) oscillatory features. The cause is taken to be the fact that whereas the magnitude of the classical Lorentz force can be subtracted for the data for sample (1400,30), this procedure may be necessary but is not possible for sample (1300,60,1400,30); the exact magnitudes of the values plotted in figure 6.4 should not be considered accurate.

One alternative would be to fit a smaller range of fields. The background from the classical Lorentz force is known to be quadratic, and hence although the WL will be suppressed at low fields by the WAL and the Lorentz force, these will be smaller contributions; this would potentially yield more accurate values for B_ϕ, but would not enable the oscillatory features to be seen.

For the purposes of extracting the oscillatory signal, the procedure from chapter 5 is followed using equation 3.2a, as the $\eta(T)$ parameter should allow scaling which will incorporate both the WAL and the Lorentz contributions. Remnant data from this procedure is presented in figure 6.7.

6.3.6 Discussion of oscillatory magnetoresistance

Magnetoconductance data for sample (1400,30) measured at various bias are presented in figure 6.8 following processing as in section 6.3.4 for comparison with figure 6.7.

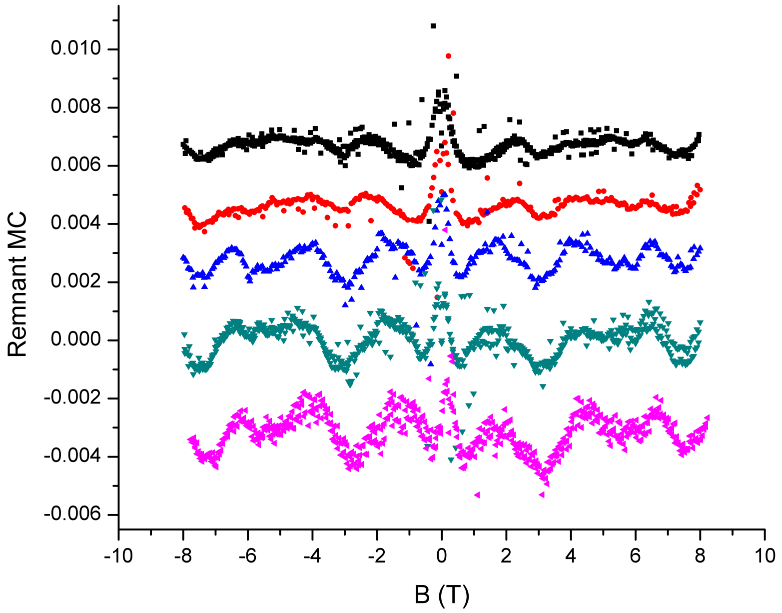

Figure 6.7: Sample (1300,60,1400,30) measured at biases of (from top) 10 μA, 5 μA, 3 μA, 1 μA, 300 nA, with high temperature data subtracted and WL fitted (using equation 3.2a) and subtracted. Traces are offset for clarity with the exception of the 1 μA trace.

The measured data for these samples, and the fitting discussion above indicate that these samples have lower levels of disorder such that their transport properties are described by graphene-specific physical models. Despite this, and despite the separate methodology required (for sample (1400,30)) the remnant traces appear similar to the remnant data discussed in chapter 5. As MR traces for sample (1400,30) show these features clearly superimposed on the general shape of the curve, the first conclusion drawn is that the fitting and conclusions from the samples in chapter 5 were valid, and definitely not based on a measurement or fitting artefact.

Both sets of data seem to show the bias dependence seen in the more disordered samples, with the features becoming less well-defined as the source-drain bias becomes higher. This is in agreement with [100], however as with the previ-

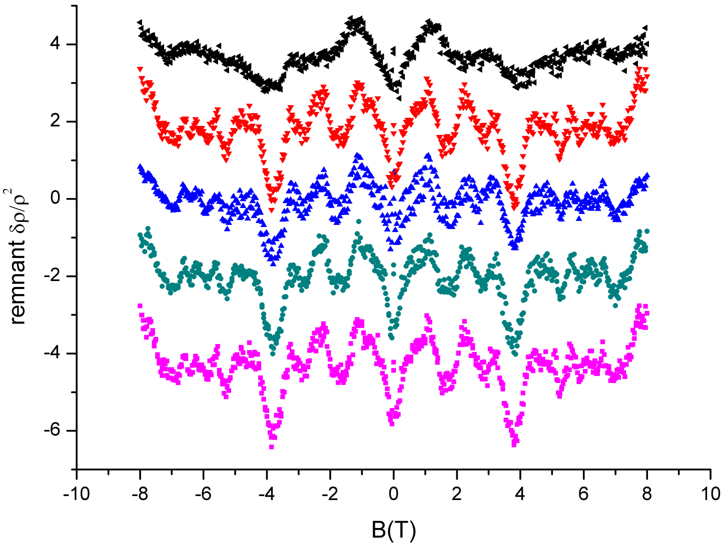

Figure 6.8: Sample (1400,30) measured at biases of (from top) 10 μA, 5 μA, 3 μA, 1 μA, 500 nA, with WAL fitted (using equation 6.2a) and subtracted. Traces are offset for clarity with the exception of the 3 μA trace, and remnant values are scaled by 10^6.

ous data, it is not possible to definitely identify the source of these oscillations.

6.4 Bias and field dependence combined

6.4.1 Dynamic conductance

The $I(V)$ characteristics of the samples in this chapter is much closer to linear than that for the more disordered samples. This can be seen in the inset to figure 6.9, the main axes of which are plotted to extract a value for the localisation length. The data at high fields is again a good approximation to a linear relationship, and the localisation length yielded is 400 nm for sample (1300,60,1400,30) and 1.5 μm for sample (1400,30), which is in agreement with the transition into the WL regime.

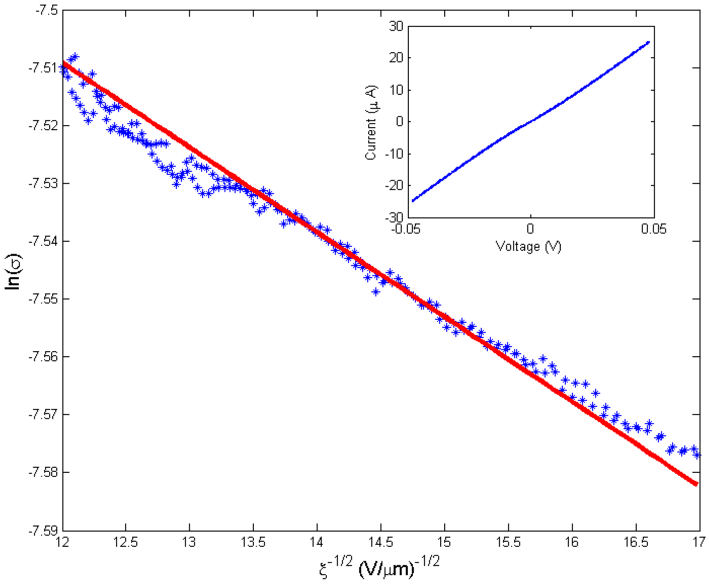

Figure 6.9: Plot to extract localisation length from I(V) measurements. Data shown is for sample (1300,60,1400,300).

6.4.2 Dynamic conductance and magnetic field

The near-linear $I(V)$ means that measuring MR at different bias gives very similar curves, unlike for samples in chapter 5. A consequence of this is that additional processing is possible on the plots of resistance and bias dependence introduced previously. Subtracting a linear term from the measured dynamic conductance trace results in visible oscillations not only in individual MR curves, but in the surfaces; figure 6.10 shows the result of this operation for sample (1400,30). The measured change in R with B and bias is shown in figure 6.10a and the results of a linear subtraction from the measured $I(V)$ are shown in figure 6.10b.

The surface subtraction plot presented in figure 6.11 is for a narrower bias range. The oscillatory component in magnetic field seen in individual MR traces can be seen to be present across all bias shown here. This is to be expected given

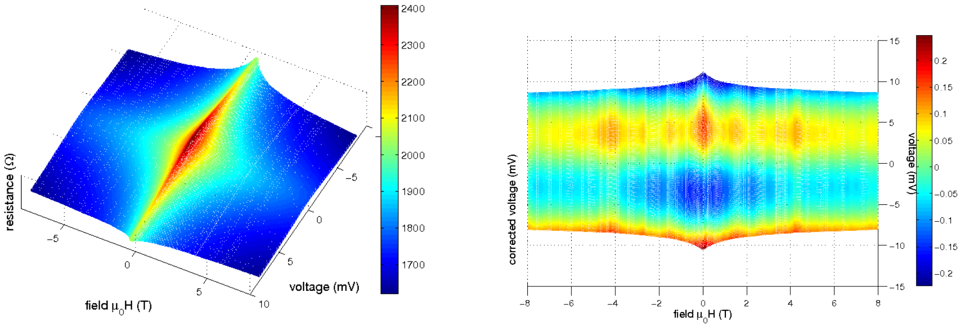

(a)

(b)

Figure 6.10: Data for sample (1300,60,1400,30) plotted to show dependence of resistance on source-drain bias and magnetic field (a), and the same data processed to remove a linear $I(V)$ (b).

the equivalence between this data and that presented in figure 6.7, but is should be stressed that the method used here included no fitting to WL parameters, but simply the subtraction of a linear fit from the $I(V)$ taken at each field position.

6.5 Conclusions / discussion

The first conclusion from the data presented in this chapter is a simple comparison between these samples and those for which transport properties were presented in chapter 5. The surface techniques used and presented in chapter 4 (with the exception of AFM) do not enable the two sets of samples to be distinguished. Transport properties, the aspect of the samples which exhibits the most potential for applications, also enable this distinction to be made. The conclusions drawn in terms of length scales are in agreement with AFM, and point to an increase in lateral size of at least an order of magnitude.

The remaining conclusions drawn from the various measurements and analyses are all a consequence of the longer physical (and hence electronic) coherence lengths of the samples. The first effect is that the $I(V)$ of the samples remains almost linear at low temperatures. The value of dR/dT is still negative, but

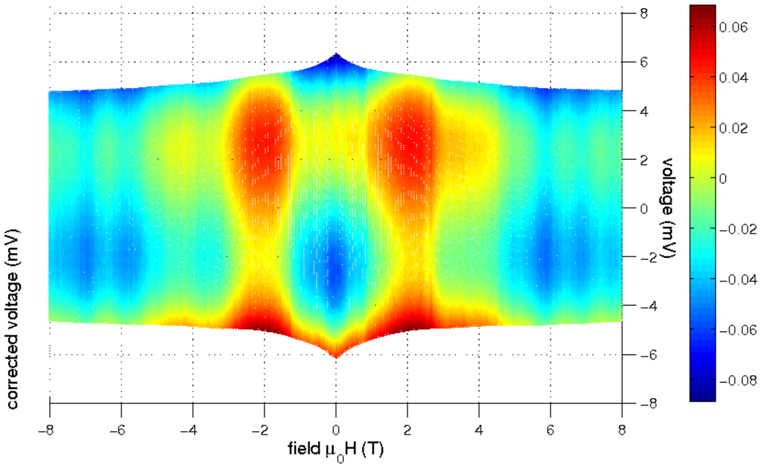

Figure 6.11: Sample (1300,60,1400,30) with a linear fit to the $I(V)$ data subtracted.

plots show that $k_{\mathrm{F}}l \gg 1$, as the change with temperature is described by the WL regime. The evidence for greater coherence continues with data from more specific measurements. The peak in WL magnetoresistance is sharper; this is partially quantified via lower characteristic fields, B_{ϕ}, required to fit the MR data, indicating lower scattering rates. The WL can also be seen to saturate at high fields.

The evolution of the WAL features, which cause a suppressed WL for sample (1300,60,1400,30) and a positive WAL component for sample (1400,30), coincide with the evidence for longer coherence lengths as samples are measured which are of higher quality. This provides a clear demonstration of the competing scattering processes present in these samples.

In terms of growth conditions and dynamics, the data support the considerations which lead to annealing at higher temperatures. Shorter durations are needed for continuous coverage of the substrate; the implication being that this far above the activation temperature the rate of propagation increases dramatically. This leaves scope for further improvements in film quality to be achieved by anneals at still higher temperatures. That the duration of these anneals should be short is indicated by the sample introduced in chapter 5 which had an anneal at 1535 °C for 60 minutes: the many layers of carbon formed in this case means that the system does not exhibit graphene-like properties.

The two-stage process experienced by sample (1300,60,1400,30) has resulted in a measurably higher quality sample than might be expected. While the longest coherence times found were for the sample without the initial anneal at a lower temperature, the transport properties from the two-stage process support the initial conclusion drawn from the AFM data.

Chapter 7

Electron-electron interactions

7.1 Introduction

The resistance change with temperature for samples shown in chapter 5 shows a possible contribution from interaction between electrons. The magnetoresistance measurements in chapter 5 appear to be explained comprehensively by a weak localisation regime, albeit possibly with a scaling factor, as discussed. In this chapter a subset of the MR data will be considered in greater detail, in order to investigate contributions to the electrical characteristics of the material from electron-electron interactions; contributions from interaction effects have been seen in graphene in cleaved graphite system (reference [105]) and such effects are not uncommon in two-dimensional materials.

7.2 Characteristic MR shapes

As discussed in chapter 5, in general, AC and DC measurements show the same features. The exception is a set of data from AC measurements on sample 2421 (annealed for 45 mins at 1300 °C). Subsequent measurements (both AC and DC) have not reproduced the initial features fully, due probably to sample degradation. The result set discussed here is seen in figure 7.1, and shows a clear trend with bias which argues strongly against the features being measurement artefacts.

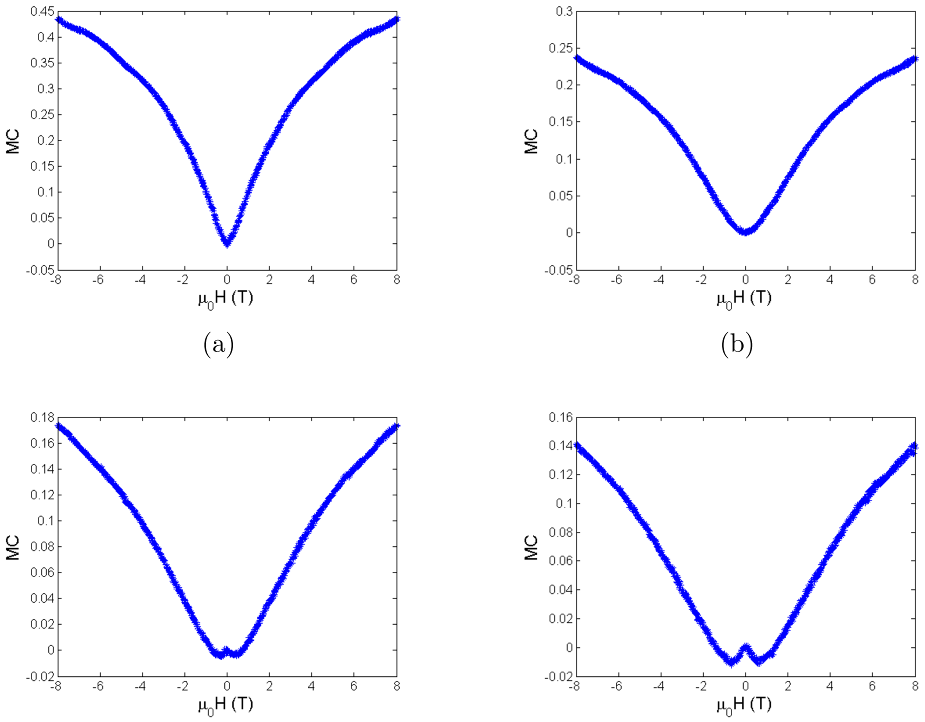

(a) (b)

(c) (d)

Figure 7.1: Sample (1300,45). Magnetoconductance curves at different AC bias. 50 nA (a), 1 μA (b), 3 μA (c) and 10 μA (d).

At low fields, a small negative magnetoconductance feature can be seen, which at higher fields is lost as the familiar weak localisation positive MC is established. The negative MC also disappears for lower bias measurements.

This set of data provides an additional suggestion that closer consideration of electron-electron interactions may be warranted across all samples. As described in subsequent sections, similar (although far less prominent) features are seen through a selection of samples measured, when the data and fitting are treated in a detailed fashion. The procedure is first developed for the data shown in figure 7.1, and then applied to other samples' data.

7.3 Fitting and subtractions

Measured MR curves at a temperature of 1.5 K and AC bias of over 1 μA show a clear difference in MR response when compared with the DC measurements presented so far. Whereas equations for WL fitted the data presented in chapters 5 and 6 well, even before these are attempted for this data it is expected that they will not achieve a good fit at low applied fields. Figure 7.2 shows an example of attempted fits to both equations for the 10 μA data shown in figure 7.1, and also the remnant from the fit, *i.e.* the experimental data with the fitting function subtracted.

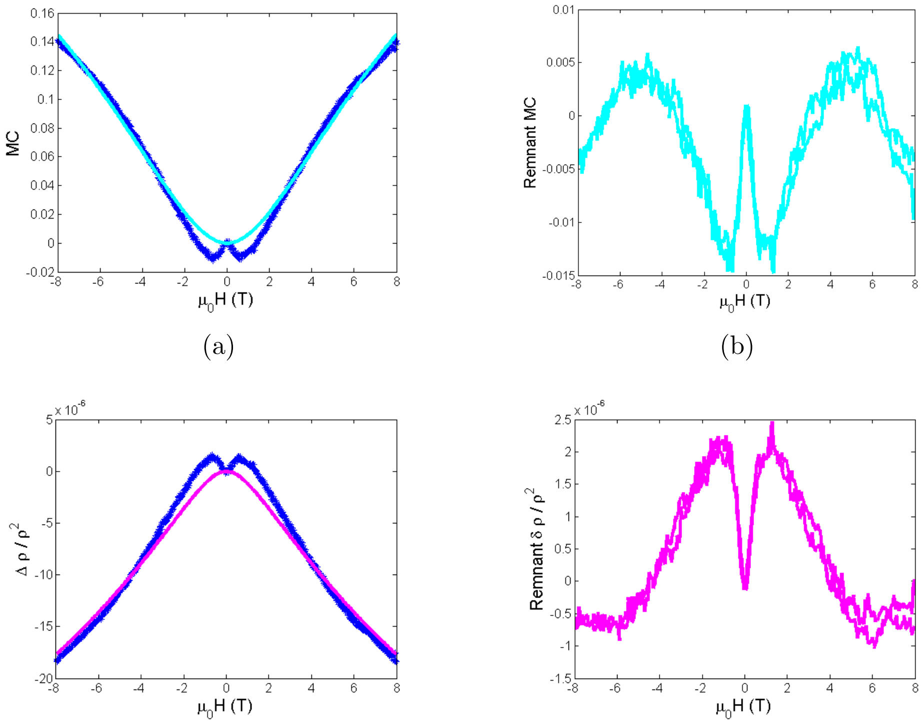

(a) (b) (c) (d)

Figure 7.2: Sample (1300,45). Fits to data (a) and remnant from the fit, (b) for the expression for WL in [60], and then fit and remnant from the WL expression in [62]: (c) and (d). Measured data are dark blue.

The fits, as expected, are poor. They fail to follow the experimental data at low fields, and also at higher fields; the parameters which give the closest overall fit over the entire range of data are incorrect, as the fit expression does not have terms which address the low-field feature.

This feature is not seen in the published graphene literature, but similar features are found in the literature for disordered carbon [60], and are attributed to electron-electron interaction. As the data from R(T) measurements could not rule out a contribution from this mechanism, this does not seem unlikely. Closer investigation and further fitting reveals that even in samples where there is no electron-electron contribution visible to the naked eye, there is a definite trend once the dominant (WL) features are subtracted. The effect is not confined to a single sample, or to AC measurements, and is fully described in the following section.

7.3.1 Fitting with an additional term

There are indications from the RvT data that simply fitting to localisation theory may not be sufficient to accurately describe the electron transport properties of these samples. For several measurements of sample annealed at 1300 °C for 45 mins, there is a visible discrepancy between the MR data and the expected shape due only to localisation effects. In reference [60] an additional term is added to include electron-electron interaction, following reference [106] and the full expression for expected MR becomes

$$MC = \eta(T)\left[\Psi\left(\frac{1}{2}+\frac{B_2}{B}\right)-\Psi\left(\frac{1}{2}+\frac{B_1}{B}\right)-\ln\frac{B_2}{B_1}\right]-A_{\mathrm{e}}\frac{B^2}{B^2+B_{\mathrm{e}}^2}. \tag{7.1}$$

Here B_{e} is a characteristic field for spin alignment, and A_{e} is a constant which scales the contribution from the electron-electron effect.

It is instructive to plot the fit and the remnant data from the fit with and without the additional term. Figures 7.3a and 7.3b show examples of such plots. The fit to the full expression (equation 7.1) shows far closer agreement. A final useful graph, shown in figure 7.3c plots the difference between the two fit expressions. For the data in figure 7.3 this seems superfluous, as figures 7.3b and 7.3c are so similar, but in cases where the deviation is less clear, the shape of this final plot can be taken as an indicator of the presence of electron-electron interactions.

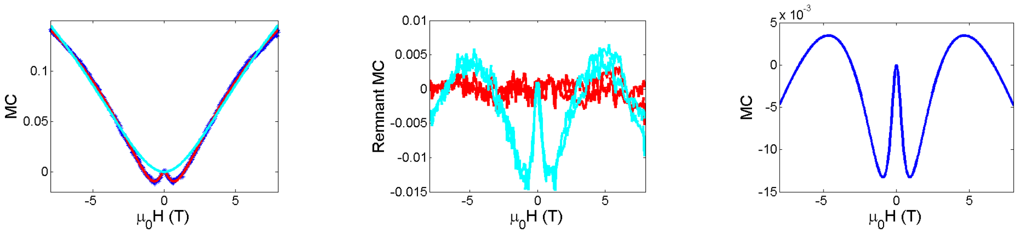

(a) (b) (c)

Figure 7.3: Sample (1300,45). Fits to the expression in [60] (equation 7.1) both with (red) and without (cyan) the term for e-e interaction. Data is in blue(a). In (b) the remnant data is shown for each, and in (c) the two fit expressions are subtracted from each other.

The shape of the remnant data in figure 7.3c is now used as a template to interpret graphs plotted as a result of performing the same fit and subtraction for sample (1300,45) at various bias 7.4. Using this set of data, it appears that the shape of the remnant is a good indicator of the presence of electron-electron interactions.

One possible explanation of the bias-dependence is space-charge limited current as described by the Mott-Gurney law.

$$j = \frac{9\epsilon\mu V^2}{8L^3} \tag{7.2}$$

where j is the current density, ϵ is the dielectric constant of the material, μ the mobility, V the applied voltage and L the distance between the electrodes.

Following this initial data set, the same procedure was attempted across all samples mentioned in chapter 5. This was done irrespective of whether there was any visible sign of e-e contributions in the measured data. The idea is that the

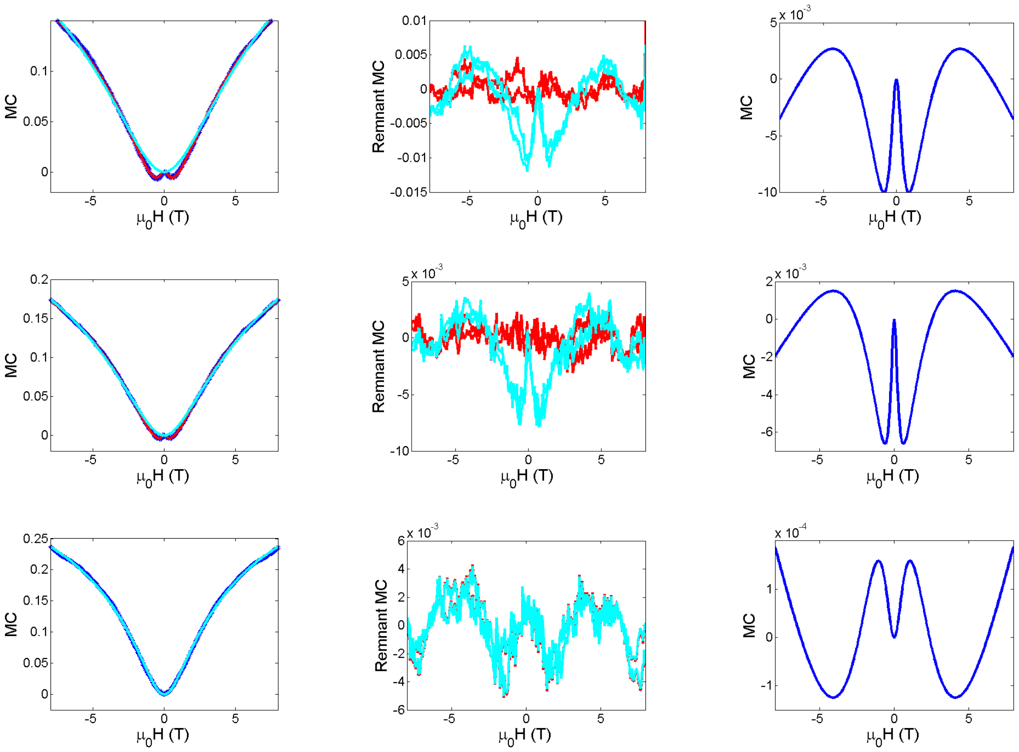

Figure 7.4: Sample (1300,45) at different biases. 5 μA top row, 3 μA second row, and 1 μA bottom row. For each measurement, the fit to WL is shown in cyan, and with an electron-electron (ee) term in red. The remnants (data-fit) are shown in the centre figure, and the fit differences (WL-WL with ee) are shown on the right.

remnant (difference between the two fits) can make visible a very small contribution from e-e. The low-field section of the graph is most pertinent, with the peak towards zero field indicating the poor fit to the data unless the e-e term is included. While there was an indication that some samples could only be fitted poorly (assessed by one or more parameters being returned at the boundary value, even when this was non-physical), a definite conclusion could not be drawn. This (certainly for sample (1300,60)) was partially due to the remnant features discussed in chapter 5.

7.4 Temperature dependence

In order to avoid the issue of the oscillatory features from (1300,60), and attempt to quantify the contribution rather than identify an MR feature, equation 7.1 was used to fit MR data for (1300,60) and for (1300,45) measured at various temperatures. The parameter A_e was then plotted for each fit to create figure 7.5. The plots shows that the magnitude of the electron-electron interaction increases as the sample temperature decreases.

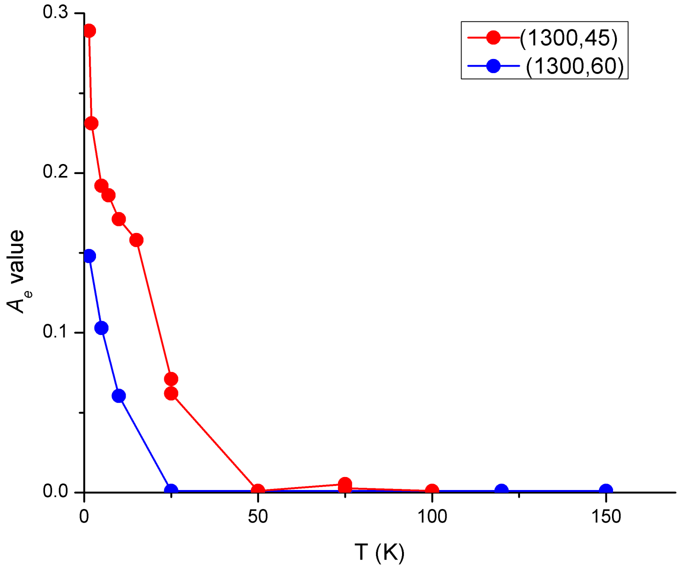

Figure 7.5: A_e values from fits to equation 7.1 for MR data measured on samples (1300,60) and (1300,45). A_e indicates the strength of the contribution to the MR from electron-electron interaction, and can be seen to increase above negligible values below a temperature of approximately 25 K.

7.5 Discussion

The MR data for sample (1300,45) show a definite contribution for higher bias measurements. At low fields this contribution causes a positive MR, which at higher fields reverts to the familiar negative weak localisation shape. Fitting this data to an equation used to model electron-electron interactions in disordered carbon is possible, with parameters which are physical for the system studied.

When plotting and fitting MR data at various temperatures, the parameter A_e, which indicates the strength of the electron-electron contribution shows a definite trend with temperature for both samples' MR data. The data used for this plot was the same set as was included in chapter 6 to show the attempted fit using WAL theory. Comparing the shape of the curve to that in figure 6.4, the point at which these samples deviate from a linear dependence on temperature for coherent transport corresponds remarkably closely to the shape of the graph seen here, indicating a possible cause for the poor trend in B_ϕ when a fit to WAL was used.

Chapter 8

Summary /Outlook

8.1 Introduction

Research into epitaxial graphene on silicon carbide is a fast-moving new research field, shown most clearly by the paper count; in the period from 2000 to 2008 a total of 31 papers on the topic can be found, with the count for subsequent years being 107, 210 and 235 (year to date). The field is maturing rapidly, with early papers devoted to the potential promise of the material, and more recent developments in the materials science aspects reaching the point where more ambitious devices can be realised. If the scope for research into mechanically cleaved graphene is considered, the increased paper count for epitaxial graphene shows a delayed start (by a year) and a yearly total 10% that of graphene as a whole.

The rapid development of the technology means that while a process is being perfected few papers are published, which in turn leads to several research groups developing similar solutions independently. An example is the range of temperatures used, beginning with those known to cause (unwanted) graphitisation of SiC during studies in the 1970s, and evolving through to much higher temperatures associated with the coalescence of disordered carbon by the formation of sp^2 bonds. This, and the considerations of growth dynamics upon which the solutions are based can seem inevitable with hindsight, with the speed of development meaning that review papers summarising widely accepted growth recipes can be presented mere months after a new development has been made.

This can alter the context of the research, with the focus being drawn to whether developments in procedure and accompanying improvements in material result in material which is equivalent to cleaved graphene, or has lateral dimensions comparable to the largest reported. While this is the ultimate objective from the point of view of applications and some fundamental research, the rich physics accessible mean that the investigations remain a source of interest; more importantly, in finding solutions or new details pertinent to the growth process existing methods can be fine-tuned.

8.2 Summary

Samples of graphitised SiC have been thoroughly characterised using a range of surface science techniques, and a variety of electronic transport measurements. Initial growth conditions have been altered on the basis of interpretations of the data acquired, and the improvements to the procedure have resulted in increased physical size of individual graphene domains of an order of magnitude (measured using AFM). The consequence of this in terms of electronic properties is a phase coherence which also improves by an order of magnitude, resulting in markedly different behaviour seen most clearly in response to an applied magnetic field.

Detailed fitting of magnetoconductance data has been carried out, using models for weak localisation and weak anti-localisation. This fitting shows that for the samples with larger lateral domain size, graphene-specific scattering must be included in order to explain the data, supporting a view of graphene-like properties emerging from what can appear to be a disordered carbon system. It can be imagined that this may well mean that the reverse is true, and that some behaviours seen distinctly in the less ordered system may well exist in highly ordered graphene systems, albeit less markedly.

Accurate fitting of these dominant contributions to the magnetoconductance means that they can be subtracted from the measured data. The similarity of the remnant MR features in the more ordered material to those initially seen in the granular samples, presented following equivalent processing to that for disordered samples, then following more complex WL / WAL subtractions and finally via an entirely separate process completes the picture of continuity between the samples measured, which is in agreement with the similar properties from the surface science techniques (especially LEED).

This in-depth analysis of non-ideal graphene not only informs changes to growth conditions which improved the quality of sample (and hold the promise of further improvement), the data also suggest an alternative growth paradigm which could resolve known limitations even in the state-of-the art as it exists today.

8.3 Outlook

The results for growth of epitaxial graphene are encouraging. Initialising a new avenue of enquiry takes time while equipment is acquired, mended or modified for a new purpose, and expertise takes time to build. Despite these initial overheads, the graphene produced so far is approaching the quality achieved by the leaders in the field when UHV conditions are used. It should be noted that the largest lateral size for graphitised SiC domains is now at the wafer scale, and is achieved by additional control over growth dynamics via confined geometry [28] or an Argon atmosphere [43].

Now that measurement systems, techniques and data interpretations are established, further progress in material quality is the number one priority. To this end recent wafers have undergone an advanced polish performed by NovsSiC, in order to improve the starting conditions. A furnace capable of being used for hydrogen annealing has been purchased and is being commissioned to further improve the surface of the substrate.

The new furnace will also enable graphitisation to be carried out in an argon atmosphere (as in [37]) which should enable the production of large areas of high quality graphene. Simultaneously to this, it should be possible to improve the quality of UHV-grown material; investigating the potential of the two-stage procedure outlined in this thesis has the potential to achieve this.

In parallel with material quality improvements, the existing quality is high enough to warrant further characterisation. The priorities here are to measure gate dependence, in order to identify and control the carrier concentration, and Hall measurements in order to fully characterise the material. This development has begun, with some e-beam patterning completed and etching conditions investigated. More complex devices, incorporating ferromagnetic and superconducting materials are envisaged as following on from these initial devices. While this development is in progress, continuing the existing measurements, but in equipment with higher magnetic field capability, and also at lower temperatures will enable more definite identification of features presented here.

Finally the growth dynamics is the subject of a scheduled experiment at Brookhaven National Laboratory, where low-energy electron microscopy (LEEM) will be used to probe the growth of samples as in [107] but with annealing conditions relevant for the investigation of the mobility of carbon as distinct from step edges, in a two-stage annealing procedure.

References

[1] P.R. Wallace. The Band Theory of Graphite. *Physical Review*, 71:622–634, 1947. x, 1, 8, 9

[2] N. D. Mermin. Crystalline order in two dimensions. *Phys. Rev.*, 176(1):250–254, 1968. 1, 7

[3] Gordon W. Semenoff. Condensed-matter simulation of a three-dimensional anomaly. *Phys. Rev. Lett.*, 53(26):2449–2452, 1984. 1

[4] K. S. Novoselov, A. K. Geim, S. V. Morozov, D. Jiang, Y. Zhang, S. V. Dubonos, I. V. Grigorieva, and A. A. Firsov. Electric Field Effect in Atomically Thin Carbon Films. *Science*, 306(5696):666–669, 2004. 1, 3

[5] A.J. Van Bommel, J.E. Crombeen, and A Van Tooren. Leed and Auger electron observations of the SiC (0001) surface. *Surface Science*, 48:463–472, 1974. 1, 27

[6] C. Berger, Z. Song, T. Li, X. Li, A.Y. Ogbazghi, R. Feng, Z. Dai, A.N. Marchenkov, E.H. Conrad, P.N. First, and W.A. deHeer. Ultrathin epitaxial graphite: 2D electron gas properties and a route toward graphene-based nanoelectronics. *Journal of Physical Chemistry B*, 108(52):19912–19916, 2004. 1, 3, 83

[7] K. S. Novoselov, A. K. Geim, S. V. Morozov, D. Jiang, M. I. Katsnelson, I. V. Grigorieva, S. V. Dubonos, and A. A. Firsov. Two-dimensional gas of massless dirac fermions in graphene. *Nature*, 438(7065):197–200, November 2005. x, 1, 9, 11, 12, 69

[8] S. V. Morozov, K. S. Novoselov, M. I. Katsnelson, F. Schedin, L. A. Ponomarenko, D. Jiang, and A. K. Geim. Strong suppression of weak localization in graphene. *Physical Review Letters*, 97(1):016801, 2006. 1

[9] K. S. Novoselov, E. McCann, S. V. Morozov, V. I. Fal'ko, M. I. Katsnelson, U. Zeitler, D. Jiang, F. Schedin, and A. K. Geim. Unconventional Quantum Hall Effect and Berry's phase of 2 π in bilayer graphene. *Nature Physics*, 2(3):177–180, 2006. 1

[10] C. L. Kane. Materials Science - Erasing electron mass. *Nature*, 438(7065):168–170, 2005. 1

[11] M. I. Katsnelson, K. S. Novoselov, and A. K. Geim. Chiral tunnelling and the Klein paradox in graphene. *Nat Phys*, 2(9):620–625, 2006. 2

[12] A. K. Geim and K. S. Novoselov. The rise of graphene. *Nature Materials*, 6(3):183–191, 2007. x, 2, 10

[13] A Cortijo and M.A.H. Vozmediano. Effects of topological defects and local curvature on the electronic properties of planar graphene. *Nuclear Physics B*, 763(3):293–308, February 2007. 2

[14] A Castro Neto, F Guinea, and N.M. Peres. Drawing conclusions from graphene. *Physics World*, (November):33–37, 2006. 2

[15] N. M. R. Peres. Colloquium: The transport properties of graphene: An introduction. *Rev. Mod. Phys.*, 82(3):2673–2700, 2010. 2

[16] D R Hang, C F Huang, W K Hung, Y H Chang, J C Chen, H C Yang, Y F Chen, D K Shih, T Y Chu, and H H Lin. Shubnikov-de Haas oscillations of two-dimensional electron gas in an InAsN/InGaAs single quantum well. *Semiconductor Science and Technology*, 17(9):999–1003, 2002. 2

[17] S. Y. Zhou, G.-H. Gweon, J. Graf, A. V. Fedorov, C. D. Spataru, R. D. Diehl, Y. Kopelevich, D.-H. Lee, Steven G. Louie, and A. Lanzara. First direct observation of Dirac fermions in graphites. *Nat Phys*, 2(9):595–599, 2006. 2

[18] Editorial. Graphene Calling. *Nat Mater*, 03:169, 2007. 3

[19] E.W. Hill, A.K. Geim, K. Novoselov, F. Schedin, and P. Blake. Graphene spin valve devices. *Magnetics, IEEE Transactions on*, 42(10):2694–2696, 2006. 3

[20] N. Staley, H. Wang, C. Puls, J. Forster, T. N. Jackson, K. McCarthy, B. Clouser, and Y. Liu. Lithography-free fabrication of graphene devices. *Applied Physics Letters*, 90(14):143518, 2007. 3

[21] Sukang Bae, Hyeongkeun Kim, Youngbin Lee, Xiangfan Xu, Jae-Sung Park, Yi Zheng, Jayakumar Balakrishnan, Tian Lei, Hye Ri Kim, Young Il Song, Young-Jin Kim, Kwang S. Kim, Barbaros Ozyilmaz, Jong-Hyun Ahn, Byung Hee Hong, and Sumio Iijima. Roll-to-roll production of 30-inch graphene films for transparent electrodes. *Nat Nano*, 5(8):574–578, 2010. 3, 15

[22] B.J. Baliga. Trends in power semiconductor devices. *Electron Devices, IEEE Transactions on*, 43(10):1717 –1731, 1996. 3

[23] Jr. Eddy, C. R. and D. K. Gaskill. Silicon Carbide as a Platform for Power Electronics. *Science*, 324(5933):1398–1400, 2009. 3

[24] R. E. Peierls. Bemerkungen ber umwandlungstemperaturen. *Helv. Phys. Acta*, 7:81–83, 1934. 7

[25] CWJ Beenakker and H Van Houten. Quantum Transport in Semiconductor Nanostructures. *Solid State Physics-Advances in Research and Applications*, 44:1–228, 1991. 8

[26] G Dresselhaus & M S Dresselhaus R Saito. *Physical properties of carbon nanotubes*. Imperial College Press, 1998. 8

[27] Y. B. Zhang, Y. W. Tan, H. L. Stormer, and P. Kim. Experimental observation of the Quantum Hall Effect and Berry's phase in graphene. *Nature*, 438(7065):201–204, November 2005. 10

[28] Xiaosong Wu, Yike Hu, Ming Ruan, Nerasoa K Madiomanana, John Hankinson, Mike Sprinkle, Claire Berger, and Walt A. de Heer. Half integer quantum Hall effect in high mobility single layer epitaxial graphene. *Applied Physics Letters*, 95(22):223108, 2009. x, 11, 17, 18, 68, 69, 110

[29] N. F. Mott and E. A. Davis. *Electronic processes in non-crystalline materials*. Clarendon Press, 1971. 12, 62

[30] A.A. Maradudin V.M Agranovich, editor. *Mesoscopic Phenomena in Solids*. North-Holland, 1987. 13

[31] Patrick A. Lee and T. V. Ramakrishnan. Disordered electronic systems. *Rev. Mod. Phys.*, 57(2):287–337, 1985. 14

[32] E. McCann, K. Kechedzhi, Vladimir I. Fal'ko, H. Suzuura, T. Ando, and B. L. Altshuler. Weak-localization magnetoresistance and valley symmetry in graphene. *Phys. Rev. Lett.*, 97(14):146805, 2006. 14, 36, 87

[33] Alan B. Kaiser, Cristina Gmez-Navarro, Ravi S. Sundaram, Marko Burghard, and Klaus Kern. Electrical conduction mechanism in chemically derived graphene monolayers. *Nano Letters*, 9(5):1787–1792, 2009. 15

[34] Peter W. Sutter, Jan-Ingo Flege, and Eli A. Sutter. Epitaxial graphene on ruthenium. *Nat Mater*, 7(5):406–411, 2008. 15

[35] Dmitry V. Kosynkin, Amanda L. Higginbotham, Alexander Sinitskii, Jay R. Lomeda, Ayrat Dimiev, B. Katherine Price, and James M. Tour. Longitudinal unzipping of carbon nanotubes to form graphene nanoribbons. *Nature*, 458(7240):872–876, 2009. 15

[36] A.J. Van Bommel, J.E. Crombeen, and A Van Tooren. Leed and Auger electron observations of the SiC (0001) surface. *Surface Science*, 48:463–472, 1974. 16, 57

[37] J. L. Tedesco, G. G. Jernigan, J. C. Culbertson, J. K. Hite, Y. Yang, K. M. Daniels, R. L. Myers-Ward, Jr. C. R. Eddy, J. A. Robinson, K. A. Trumbull, M. T. Wetherington, P. M. Campbell, and D. K. Gaskill. Morphology characterization of argon-mediated epitaxial graphene on C-face SiC. *Applied Physics Letters*, 96(22):222103, 2010. 16, 110

[38] Taisuke Ohta, N. C. Bartelt, Shu Nie, Konrad Thürmer, and G. L. Kellogg. Role of carbon surface diffusion on the growth of epitaxial graphene on SiC. *Phys. Rev. B*, 81(12):121411, 2010. 16

[39] E. Rollings, G.-H. Gweon, S.Y. Zhou, B.S. Mun, J.L. McChesney, B.S. Hussain, A.V. Fedorov, P.N. First, W.A. de Heer, and A. Lanzara. Synthesis and characterization of atomically thin graphite films on a silicon carbide substrate. *Journal of Physics and Chemistry of Solids*, 67(9-10):2172 – 2177, 2006. SMEC 2005, Study of matter under extreme conditions. 17

[40] A. Al-Temimy, C. Riedl, and U. Starke. Low temperature growth of epitaxial graphene on SiC induced by carbon evaporation. *Applied Physics Letters*, 95(23):231907, 2009. 17

[41] A. Charrier, A. Coati, T. Argunova, F. Thibaudau, Y. Garreau, R. Pinchaux, I. Forbeaux, J.-M. Debever, M. Sauvage-Simkin, and J.-M. Themlin. Solid-state decomposition of Silicon Carbide for growing ultra-thin heteroepitaxial graphite films. *Journal of Applied Physics*, 92(5):2479–2484, 2002. 17

[42] Walt A. de Heer, Claire Berger, Xiaosong Wu, Phillip N. First, Edward H. Conrad, Xuebin Li, Tianbo Li, Michael Sprinkle, Joanna Hass, Marcin L. Sadowski, Marek Potemski, and Grard Martinez. Epitaxial graphene. *Solid State Communications*, 143(1-2):92 – 100, 2007. Exploring graphene - Recent research advances. 17, 19, 43

[43] Konstantin V. Emtsev, Aaron Bostwick, Karsten Horn, Johannes Jobst, Gary L. Kellogg, Lothar Ley, Jessica L. McChesney, Taisuke Ohta, Sergey A. Reshanov, Jonas Rohrl, Eli Rotenberg, Andreas K. Schmid,

Daniel Waldmann, Heiko B. Weber, and Thomas Seyller. Towards wafer-size graphene layers by atmospheric pressure graphitization of silicon carbide. *Nat Mater*, 8(3):203–207, 2009. 17, 54, 110

[44] J. Hass, F. Varchon, J. E. Millan-Otoya, M. Sprinkle, N. Sharma, W. A. de Heer, C. Berger, P. N. First, L. Magaud, and E. H. Conrad. Why multilayer graphene on 4H-SiC($000\bar{1}$) behaves like a single sheet of graphene. *Phys. Rev. Lett.*, 100(12):125504–4, 2008. 19, 21, 40, 41

[45] C. Riedl, C. Coletti, T. Iwasaki, A. A. Zakharov, and U. Starke. Quasi-free-standing epitaxial graphene on SiC obtained by hydrogen intercalation. *Phys. Rev. Lett.*, 103(24):246804, 2009. 19

[46] Inc. CREE. 4600 Silicon Drive Durham, NC 27703. 21

[47] M.A. Van Hove. Analysis of dynamical low-energy electron diffraction mechanisms. *Surface Science*, 49(1):181 – 188, 1975. 26

[48] Th. Seyller, A. Bostwick, K. V. Emtsev, K. Horn, L. Ley, J. L. McChesney, T. Ohta, J. D. Riley, E. Rotenberg, and F. Speck. Epitaxial graphene: a new material. *Physica Status Solidi (b)*, 245(7):1436–1446, 2008. 27

[49] P. J. Fisher, Luxmi, N. Srivastava, S. Nie, and R. M. Feenstra. Thickness monitoring of graphene on SiC using low-energy electron diffraction. In *Journal of Vacuum Science & Technology A*, volume 28, pages 958–962. AVS, 2010. 27, 43

[50] M.S. Dresselhaus, A. Jorio, and R. Saito. Characterizing graphene, graphite, and carbon nanotubes by Raman spectroscopy. *Annual Review of Condensed Matter Physics*, 1(1):89–108, 2010. 28

[51] P. Blake, E. W. Hill, A. H. Castro Neto, K. S. Novoselov, D. Jiang, R. Yang, T. J. Booth, and A. K. Geim. Making graphene visible. *Applied Physics Letters*, 91(6):063124, 2007. 28

[52] A. C. Ferrari, J. C. Meyer, V. Scardaci, C. Casiraghi, M. Lazzeri, F. Mauri, S. Piscanec, D. Jiang, K. S. Novoselov, S. Roth, and A. K. Geim. Raman spectrum of graphene and graphene layers. *Phys. Rev. Lett.*, 97(18):187401, 2006. 28

[53] L. G. Cançado, M. A. Pimenta, R. Saito, A. Jorio, L. O. Ladeira, A. Grueneis, A. G. Souza-Filho, G. Dresselhaus, and M. S. Dresselhaus. Stokes and anti-stokes double resonance raman scattering in two-dimensional graphite. *Phys. Rev. B*, 66(3):035415, 2002. 29

[54] F. J. Himpsel, F. R. McFeely, A. Taleb-Ibrahimi, J. A. Yarmoff, and G. Hollinger. Microscopic structure of the SiO_2/Si interface. *Phys. Rev. B*, 38(9):6084–6096, 1988. 30

[55] F. Bozso, Jr. J. T. Yates, W. J. Choyke, and L. Muehlhoff. Studies of SiC formation on Si (100) by chemical vapor deposition. *Journal of Applied Physics*, 57(8):2771–2778, 1985. 30

[56] Bin Wang, Yanfeng Ma, Yingpeng Wu, Na Li, Yi Huang, and Yongsheng Chen. Direct and large scale electric arc discharge synthesis of boron and nitrogen doped single-walled carbon nanotubes and their electronic properties. *Carbon*, 47(8):2112 – 2115, 2009. 30

[57] Courtesy of Nicholas Porter. x, 33

[58] Joseph G. Checkelsky, Lu Li, and N. P. Ong. Zero-energy state in graphene in a high magnetic field. *Phys. Rev. Lett.*, 100(20):206801, 2008. 33

[59] G Heine and W Lang. Magnetoresistance of the new ceramic thermometer from 4.2K to 300K in magnetic fields up to 13T. *Cryogenics*, 38(4):377 – 379, 1998. 34

[60] Yu Wang and Jorge J. Santiago-Aviles. Large negative magnetoresistance and strong localization in highly disordered electrospun pregraphitic carbon nanofiber. *Applied Physics Letters*, 89(12):123119, 2006. 35, 62, 64, 86, 102, 103, 104

[61] Ralph Rosenbaum. Superconducting fluctuations and magnetoconductance measurements of thin films in parallel magnetic fields. *Phys. Rev. B*, 32(4):2190–2199, 1985. 36

[62] Xiaosong Wu, Xuebin Li, Zhimin Song, Claire Berger, and Walt A. de Heer. Weak antilocalization in epitaxial graphene: Evidence for chiral electrons. *Phys. Rev. Lett.*, 98(13):136801, 2007. 36, 68, 72, 83, 85, 86, 88, 90, 91, 102

[63] I. Forbeaux, J. M. Themlin, A. Charrier, F. Thibaudau, and J. M. Debever. Solid-state graphitization mechanisms of silicon carbide 6H-SiC polar faces. *Applied Surface Science*, 162-163:406 – 412, 2000. 40

[64] I. Forbeaux, J.-M. Themlin, and J.-M. Debever. High-temperature graphitization of the 6H-SiC (0001) face. *Surface Science*, 442:9–18, 1999. 40

[65] F. Amy, P. Soukiassian, and C. Brylinski. Atomic cracks and $(2\sqrt{3}\times2\sqrt{3})$-R30° reconstruction at 6H-SiC(0001) surfaces. *Applied Physics Letters*, 85(6):926–928, 2004. 42

[66] K. V. Emtsev, F. Speck, Th. Seyller, L. Ley, and J. D. Riley. Interaction, growth, and ordering of epitaxial graphene on SiC{0001} surfaces: A comparative photoelectron spectroscopy study. *Phys. Rev. B*, 77(15):155303, Apr 2008. 43

[67] Michael K. Yakes, Daniel Gunlycke, Joseph L. Tedesco, Paul M. Campbell, Rachael L. Myers-Ward, Charles R. Eddy, D. Kurt Gaskill, Paul E. Sheehan, and Arnaldo R. Laracuente. Conductance anisotropy in epitaxial graphene sheets generated by substrate interactions. *Nano Letters*, 10(5):1559–1562, 2010. 43

[68] C. Riedl, A. A. Zakharov, and U. Starke. Precise in situ thickness analysis of epitaxial graphene layers on SiC(0001) using low-energy electron diffraction and angle resolved ultraviolet photoelectron spectroscopy. *Appl. Phys. Lett.*, 93(3):033106–3, 2008. 43

[69] F. Tuinstra and J. L. Koenig. Raman spectrum of graphite. *The Journal of Chemical Physics*, 53(3):1126–1130, 1970. 44

[70] L. G. Cançado, K. Takai, T. Enoki, M. Endo, Y. A. Kim, H. Mizusaki, A. Jorio, L. N. Coelho, R. Magalh aes Paniago, and M. A. Pimenta. General equation for the determination of the crystallite size L_a of nanographite by Raman spectroscopy. *Applied Physics Letters*, 88(16):163106, 2006. 44, 47, 57

[71] A. C. Ferrari, J. C. Meyer, V. Scardaci, C. Casiraghi, M. Lazzeri, F. Mauri, S. Piscanec, D. Jiang, K. S. Novoselov, S. Roth, and A. K. Geim. Raman spectrum of graphene and graphene layers. *Phys. Rev. Lett.*, 97(18):187401, 2006. 44, 48

[72] J. Röhrl, M. Hundhausen, K. V. Emtsev, Th. Seyller, R. Graupner, and L. Ley. Raman spectra of epitaxial graphene on SiC(0001). *Applied Physics Letters*, 92(20):201918, 2008. 44, 49

[73] Dong Su Lee, Christian Riedl, Benjamin Krauss, Klaus von Klitzing, Ulrich Starke, and Jurgen H. Smet. Raman spectra of epitaxial graphene on SiC and of epitaxial graphene transferred to SiO_2. *Nano Letters*, 8(12):4320–4325, 2008. 44, 49

[74] J. C. Burton, L. Sun, F. H. Long, Z. C. Feng, and I. T. Ferguson. First- and second-order Raman scattering from semi-insulating 4H-SiC. *Phys. Rev. B*, 59(11):7282–7284, 1999. 46

[75] Christopher Barsby. Mphys report. Master's thesis, Leeds University, 2010. 46

[76] Shriram Shivaraman, M. Chandrashekhar, John Boeckl, and Michael Spencer. Thickness estimation of epitaxial graphene on SiC using attenuation of substrate Raman intensity. *Journal of Electronic Materials*, 38:725–730, 2009. 10.1007/s11664-009-0803-6. 46, 50

[77] D. Graf, F. Molitor, K. Ensslin, C. Stampfer, A. Jungen, C. Hierold, and L. Wirtz. Spatially resolved Raman spectroscopy of single- and few-layer graphene. *Nano Letters*, 7(2):238–242, 2007. 48

[78] C. Faugeras, A. Nerrière, M. Potemski, A. Mahmood, E. Dujardin, C. Berger, and W. A. de Heer. Few-layer graphene on SiC, pyrolitic graphite, and graphene: A Raman scattering study. *Applied Physics Letters*, 92(1):011914, 2008. 49

[79] F. Hiebel, P. Mallet, F. Varchon, L. Magaud, and J-Y. Veuillen. Graphene-substrate interaction on 6H-SiC($000\overline{1}$) : A scanning tunneling microscopy study. *Phys. Rev. B*, 78(15):153412, 2008. 54

[80] J-Y Veuillen, F Hiebel, L Magaud, P Mallet, and F Varchon. Interface structure of graphene on SiC: an *ab initio* and STM approach. *Journal of Physics D: Applied Physics*, 43(37):374008, 2010. 56

[81] C. Uher and L. M. Sander. Unusual temperature dependence of the resistivity of exfoliated graphites. *Phys. Rev. B*, 27(2):1326–1332, 1983. 60

[82] X. Zhang, Q. Z. Xue, and D. D. Zhu. Positive and negative linear magnetoresistance of graphite. *Physics Letters A*, 320(5-6):471 – 477, 2004. 60

[83] M.Z. Tahar, M.S. Dresselhaus, and M. Endo. Size effects in electrical properties of benzene-derived graphite fibers. *Carbon*, 24(1):67 – 72, 1986. 61

[84] L. A. Pendrys, C. Zeller, and F. L. Vogel. Electrical transport properties of natural and synthetic graphite. *Journal of Materials Science*, 15(8):2103–2112, 1980. 61

[85] Yu Wang and Jorge J. Santiago-Aviles. Large negative magnetoresistance and two-dimensional weak localization in carbon nanofiber fabricated using electrospinning. *Journal of Applied Physics*, 94(3):1721–1727, 2003. 61

[86] Gerd Bergmann. Physical interpretation of weak localization: A time-of-flight experiment with conduction electrons. *Phys. Rev. B*, 28(6):2914–2920, 1983. 61

[87] A L Efros and B I Shklovskii. Coulomb gap and low temperature conductivity of disordered systems. *Journal of Physics C: Solid State Physics*, 8(4):L49, 1975. 64

[88] A. Faißt and H. v. Löhneysen. Electrical resistance and magnetoresistance of pyrocarbon at low temperatures in fields up to 14 Tesla. *Carbon*, 40(3):321 – 327, 2002. 64

[89] Johannes Jobst, Daniel Waldmann, Florian Speck, Roland Hirner, Duncan K. Maude, Thomas Seyller, and Heiko B. Weber. Quantum oscillations and quantum Hall effect in epitaxial graphene. *Phys. Rev. B*, 81(19):195434, 2010. 68

[90] G. M. Minkov, O. E. Rut, A. V. Germanenko, A. A. Sherstobitov, B. N. Zvonkov, E. A. Uskova, and A. A. Birukov. Quantum corrections to conductivity: From weak to strong localization. *Phys. Rev. B*, 65(23):235322, 2002. 70

[91] Yong-Jun Liu and Chang-De Gong. The study of spin-spin correlations in quasi-one-dimensional Heisenberg antiferromagnetic clusters. *Journal of Physics: Condensed Matter*, 14(3):493, 2002. 70

[92] Claire Berger, Zhimin Song, Xuebin Li, Xiaosong Wu, Nate Brown, Cecile Naud, Didier Mayou, Tianbo Li, Joanna Hass, Alexei N. Marchenkov, Edward H. Conrad, Phillip N. First, and Walt A. de Heer. Electronic confinement and coherence in patterned epitaxial graphene. *Science*, 312(5777):1191–1196, 2006. 71, 84

[93] Jai Seung Yoo, Yung Woo Park, Viera Skákalová, and Siegmar Roth. Shubnikov–de Haas and Aharonov Bohm effects in a graphene nanoring structure. *Applied Physics Letters*, 96(14):143112, 2010. 71

[94] R.V. Gorbachev, F.V. Tikhonenko, A.S. Mayorov, D.W. Horsell, and A.K. Savchenko. Weak localisation in bilayer graphene. *Physica E: Low-dimensional Systems and Nanostructures*, 40(5):1360 – 1363, 2008. 17th International Conference on Electronic Properties of Two-Dimensional Systems. 72

[95] A.B. Pippard. *Magnetoresistance in Metals*. Cambridge University Press, 1989. 75

[96] D. Weiss, M. L. Roukes, A. Menschig, P. Grambow, K. von Klitzing, and G. Weimann. Electron pinball and commensurate orbits in a periodic array of scatterers. *Phys. Rev. Lett.*, 66(21):2790–2793, 1991. 75

[97] T. Shen, Y. Q. Wu, M. A. Capano, L. P. Rokhinson, L. W. Engel, and P. D. Ye. Magnetoconductance oscillations in graphene antidot arrays. *Applied Physics Letters*, 93(12):122102, 2008. 75, 90

[98] R. Giraud, L. Vila, A. Lematre, and G. Faini. Large phase coherence effects in GaMnAs-based nanostructures: Towards a quantum spintronics. *Applied Surface Science*, 254(1):343 – 346, 2007. Proceedings of the 13th International Conference on Solid Films and Surfaces - ICSFS 13. 76

[99] D.W. Horsell, A.K. Savchenko, F.V. Tikhonenko, K. Kechedzhi, I.V. Lerner, and V.I. Fal'ko. Mesoscopic conductance fluctuations in graphene. *Solid State Communications*, 149(27-28):1041 – 1045, 2009. Recent Progress in Graphene Studies. 76

[100] Zhi-Min Liao, Bing-Hong Han, Hong-Zhou Zhang, Yang-Bo Zhou, Qing Zhao, and Da-Peng Yu. Current regulation of universal conductance fluctuations in bilayer graphene. *New Journal of Physics*, 12(8):083016, 2010. 76, 94

[101] Neal E. Staley, Conor P. Puls, and Ying Liu. Suppression of conductance fluctuation in weakly disordered mesoscopic graphene samples near the charge neutral point. *Phys. Rev. B*, 77(15):155429, 2008. 76

[102] D.P. Wang, D.E. Feldman, B.R. Perkins, A.J. Yin, G.H. Wang, J.M. Xu, and A. Zaslavsky. Hopping conduction in disordered carbon nanotubes. *Solid State Communications*, 142(5):287 – 291, 2007. 77, 78

[103] F. V. Tikhonenko, A. A. Kozikov, A. K. Savchenko, and R. V. Gorbachev. Transition between electron localization and antilocalization in graphene. *Phys. Rev. Lett.*, 103(22):226801, 2009. 90

[104] S. M. Sze. *VLSI technology.* McGraw-Hill, 1988. 91

[105] ChangLing Tan, ZhenBing Tan, Li Ma, FanMing Qu, Fan Yang, Jun Chen, GuangTong Liu, HaiFang Yang, ChangLi Yang, and Li Lu. Observation of electron weak localization and correlation effects in disordered graphene. *Science in China Series G: Physics Mechanics and Astronomy*, 52:1293–1298, 2009. 100

[106] A. Frydman and Zvi Ovadyahu. Spin and quantum interference effects in hopping conductivity. *Solid State Communications*, 94(9):745 – 749, 1995. 103

[107] H. Hibino, H. Kageshima, F. Maeda, M. Nagase, Y. Kobayashi, and H. Yamaguchi. Microscopic thickness determination of thin graphite films formed on SiC from quantized oscillation in reflectivity of low-energy electrons. *Phys. Rev. B*, 77(7):075413, 2008. 111